University of Southern Queensland
Faculty of Health, Engineering and Sciences

Development of a low-cost IoT Thermal Work Limit sensor used in construction tunnels

A dissertation submitted by

Chism Long

In the fulfilment of

ENG4111 & ENG4112 Research Project

Towards the degree of

Bachelor of Electrical Engineering (Honours)

Submitted September 2023

Abstract

The significance of Thermal Work Limit (TWL) monitoring in tunnel environments stems from potential health hazards, particularly heat stress. Despite the enhancements in IoT devices that monitor environmental parameters, there exists a notable deficiency in cost-effective, real-time TWL monitoring systems suitable for tunnel environments. The Project uses the calculation methodology formulated by Derrick Brake and Graham bates and applies the TWL Index with IoT technology in a real-world application, providing a low-cost solution to real-time health and safety monitoring.

Addressing the unique challenges of sensor placement in a construction tunnel was an essential part of this research. The airflow patterns, influenced by the tunnel's shape and the presence of Mechanical and Electrical (M&E) equipment, demanded research into sensor positioning. A systematic, grid-based analysis was adopted, with the aim of identifying locations that offered a consistent representation of wind speeds. From the data gathered, an ideal position for the anemometer was determined at a location 5.0m above the paving surface around the centre of the tunnel.

Hardware choices played a critical role in the development of the prototype. The Arduino Nano 33 IoT emerged as the chosen microcontroller after an evaluation of ten potential candidates. The integration of the Adafruit BME280 sensor and FS7 constant temperature anemometer were critical for acquiring accurate atmospheric and environmental data. The software was a significant part of the foundation of the prototype. The coding ensured seamless operation and interfacing of the sensors and components. The primary emphasis during this process was acquisition and validation of data from the BME280 sensor, and AF7 CTA ensuring accurate measurement data for TWL calculations. The integration with the Arduino IoT Cloud was also important as it handled, processed, and presented data, for the real-time visualisations. This integration aided in immediate data assessment but also highlighted the potential for future enhancements, including remote monitoring, scalability, and inter-device communication.

The implementation of the prototype underwent a 32-hour deployment. The deployment was interrupted by site commissioning activities and had to be removed. Within those 32 hours, the system captured valuable and usable data, however it was 5 ½ days short of the projected test time which would have offered a more comprehensive dataset. Results from calibration, workshop and onsite testing can substantiate the information obtained during the prototype’s short deployment.

University of Southern Queensland

Faculty of Health, Engineering and Sciences

ENG4111 & ENG4112 Research Project

Limitations of Use

The Council of the University of Southern Queensland, its Faculty of Health, Engineering and Sciences, and the staff of the University of Southern Queensland, do not accept any responsibility for the truth, accuracy or completeness of material contained within or associated with this dissertation.

Persons using all or any part of this material do so at their own risk, and not at the risk of the Council of the University of Southern Queensland, its Faculty of Health, Engineering and Sciences or the staff of the University of Southern Queensland.

This dissertation reports an educational exercise and has no purpose or validity beyond this exercise. The sole purpose of the course pair entitles “Research Project” is to contribute to the overall education within the student’s chosen degree program. This document, the associated hardware, software, drawings, and any other material set out in the associated appendices should not be used for any other purpose: if they are so used, it is entirely at the risk of the user.

Certification

I certify that the ideas, designs and experimental work, results, analyses and conclusions set out in this dissertation are entirely my own effort, except where otherwise indicated and acknowledged.

I further certify that the work is original and has not been previously submitted for assessment in any other course or institution, except where specifically stated.

Chism Long

Student Number: [redacted]

Acknowledgements

I would like to express my gratitude to my supervisors Habib Alehossein and Tobias Low for their support throughout the Project.

Mostly, I would like to that my wife for her support throughout my studies and keeping me on track, making it all possible.

List of Figures

List of Tables

List of Appendices

Table of Contents

1 Introduction

1.1 Introduction

Thermal work limit (TWL) is widely researched and documented with Australia's Rick Brake and Graham Bates paving the way through vast studies carried out in construction and mining work environments through 1990 to early 2000 period. The aim of these studies was to identify applicable methods to safely assess work conditions to limit heat stress related incidents. In mining and construction tunnels, TWL readings are traditionally taken using hand-held meters in various locations at finite times. Temperatures in underground mining and construction are subject to rapid changes due to geo-thermal pockets and exothermic reactions from construction activities such as concrete paving pours.

The integration of Internet of Things (IoT) sensors into external environments presents an opportunity for further development into weather and environment monitoring. Within the specific field of construction tunnels, the development of a low-cost IoT Thermal Work Limit (TWL) sensor is therefore the focal point of this research. IoT sensors can provide real-time data on temperature, humidity, and air velocity, factors which are essential for calculating TWL. By collating this information, construction managers and safety teams can make informed decisions to optimise worker safety and productivity.

The development of an IoT TWL sensor for construction tunnels addresses the critical need for timely monitoring of thermal conditions and heat stress in the construction industry. This dissertation examines the design complexities, development methodologies, and practical applications of this sensor. This dissertation delves into the intricate design, development, and potential benefits of such an IoT TWL sensor, aiming to provide a cost-effective solution for the tunnelling industry. The ensuing chapters provide detailed insights into the sensor's design, capabilities, and impact on tunnel construction practices.

1.2 Project Brief

This project focuses on the development of an affordable IoT Thermal Work Limit (TWL) sensor tailored for construction tunnel environments. Tunnel construction presents many challenges related to thermal conditions, impacting worker safety and efficiency. The TWL sensor aims to provide real-time environmental data and TWL levels to continually monitor and assess heat stress in construction tunnels. By offering a low-cost solution, that is both accurate and reliable, the aim is to provide projects the ability to purchase a network of devices which can be deployed across work sites.

1.3 Research Objectives

The following research objectives detail the processes and milestones which were required for the successful completion of the project in accordance with project plan and objectives in Appendix A.

1. Conduct literature review of Thermal Work Limit (TWL) methodologies, TWL and IoT devices and sensors.
2. Identify relevant parameters required for TWL calculations.
3. Carry out analysis on air flow requirements for optimising sensor position in tunnel.
4. Carry out analysis on IoT equipment, sensors, and cloud interfaces.
5. Develop conceptual design for prototype and associated circuitry.
6. Develop coding for prototype and IoT cloud connectivity.
7. Purchase and construct prototype as per design documentation.
8. Carry out calibration and operational testing on prototype.
9. Carry out redundancy, failure, and safety testing on prototype.
10. Deploy prototype and collect environment data.
11. Analyse sensor data and ascertain operational effectiveness.
12. Present Research Project in final dissertation report.

1.4 Project Overview

The project was carried out in the following structure to achieve project objectives as set out in Section 1.3 in line with the Project timeline.

1.4.1 Research Stage

A literature review will be detailed in Chapter 2. The review will provide an insight into current heat indexes, TWL calculation and methodology as well as an overview of current TWL technologies and IoT advancements in environmental data collection.

Chapter 3 explores the parameters required for TWL calculations providing the necessary research used to support hardware selection.

Chapter 4 focuses on resource analysis, evaluating potential hardware options for the project. A selection criterion for finding for appropriate sensors, equipment and IoT platform for effective TWL monitoring is also provided.

1.4.2 Design and Development Stage

Chapter 6 focuses on the sensor's circuit design, detailing the individual components utilised. It then transitions to the housing specifications for the sensor and finally the development of the programming and coding integral to the sensor's functionality.

Chapter 7 starts with the calibration procedures for temperature, humidity, pressure, and wind speed sensors. An overview of bench testing methods is provided to confirm operation of the device. The final section discusses redundancy, failure scenarios, and essential safety testing measures.

1.4.3 Implementation and Analysis Stage

The completion stage involves evaluating data to ensure its accuracy and alignment with project outcomes.

1.4.4 Completion Stage

This stage includes the submission of the dissertation, marking the completion of the Research Project. The document adheres to established referencing and citation as per project referencing specification. The dissertation will be written in a clear and logical manner, completed within the specified timeframe.

1.5 Project Risk Assessment

The Project risk assessment strictly adhered to the safe work method practices of the Rozelle Interchange Project. This encompasses specific practices related to working at height and requirements for the use of an elevated work platform, which were essential for the success of the Project. The development and evaluation of risks were methodically carried out using a generic risk assessment matrix, ensuring alignment with the project's risk assessment specifications. The risk assessment matrix is shown in Table 1.

Table 1 Risk assessment matrix (JHCPB JV RIC, 2023)

PROBABILITY OR CHANCE	QUALITATIVE ASSESSMENT	RECURRENCE TIMEFRAME		Management Impact	* Impact of event absorbed through normal activity	* Will require some local management attention over several days	* Significant event that can be managed with careful attention, will take some project managers much time for several weeks * Local operation of contingency plan	* Major event that requires the implementation of crisis and contingency plans at a project level, regional area or support function (DRP) * Will require the involvement of senior managers and will take up the time of project managers for several weeks	* Critical event or disaster with significant impact on the Rozelle Interchange Project that requires considerable senior management time to handle over several months * Full implementation of Rozelle Interchange Project's crisis management plan for days to weeks
				CONSEQUENCE					
				RATING	1	2	3	4	5
≥ 90%	Almost certain to occur during the project / contract life	Less than "Monthly"	LIKELIHOOD	ALMOST CERTAIN	D	C	B	A	A
51% to 89%	Considered likely to occur during the project / contract life	"Monthly" to "Yearly"		LIKELY	D	D	C	B	A
30% to 50%	Considered a possible occurrence during the project / contract life	Between 2 and 5 years		POSSIBLE	E	D	C	C	B
5% to 29%	Considered unlikely to occur during the project / contract life	Between 5 and 20 years		UNLIKELY	E	E	D	C	B
< 5%	Considered a rare occurrence to happen during the project / contract life	Greater than every 20 years		RARE / REMOTE	E	E	D	D	C

The full Project risk assessment can be found in Appendix C. It is vital to note that all potential hazards were rigorously evaluated based on both their likelihood of occurrence and the severity of their possible outcomes, whether these outcomes pertain to monetary loss, personal injury, or equipment damage.

1.6 Project Ethical Considerations

When developing a sensor that monitors heat stress, upholding ethical standards becomes crucial. Inaccurate data from such a device can potentially jeopardise the safety and well-being of personnel working within construction tunnels. The sensor's precision could directly influence decision-making processes related to worker safety, and any discrepancies can lead to harmful or potentially fatal outcomes. As a result, ensuring the reliability and accuracy of the sensor not only serves a technical requirement but also a profound ethical obligation to protect human lives in potentially hazardous environments. It is noted that this is a prototype and should not be directly used as a sole source for information. Throughout the project, diligence was maintained to ensure that the collection, analysis, and dissemination of information remained factual and unbiased. Although no additional ethical

issues were anticipated during the theory and design stages, caution was exercised during construction and testing phases.

1.7 Dissertation Overview

Chapter 1 introduces the context, significance, and objectives of the research related to the IoT Thermal Work Limit sensor Project.

Chapter 2 provides a detailed analysis of existing literature on Thermal Work Limit, focusing on current applications, and technological advancements. It also includes a review of IoT advancements and accurate anemometer sensors.

Chapter 3 details the specific parameters affecting TWL and outlines the methods and formulation vital for its accurate calculation.

Chapter 4 assesses available resources, focusing on hardware options best suited for the sensor's design and functionality.

Chapter 5 examines optimal positioning strategies to maximise the accuracy and efficacy of the IoT TWL sensor.

Chapter 6 details the sensor's design aspects, from circuitry layout and housing specifications to the integral programming and coding of the device and IoT cloud connectivity.

Chapter 7 discusses the rigorous calibration procedures for the sensor and its subsequent testing phases to ensure reliability and safety.

Chapter 8 discusses the implementation of the sensor, detailing data collection and subsequent analysis of this data.

Chapter 9 concludes the dissertation summarising key findings of the research, potential applications, and future directions in the potential advancements in IoT TWL sensors.

This is followed by the References section, which lists all applicable research sources, and the Appendices, which includes supplementary material relevant to the Research Project.

2 Literature Review

2.1 Chapter Overview

This literature review examines the importance of Thermal Work Limit (TWL) monitoring in construction tunnels, analysing current methodologies, technologies, and research gaps. Tunnels play pivotal roles in transportation and essential service pathways (Karen & Myer 2020). However, tunnel construction introduces significant health and safety risks to workers due to environmental factors (Chan et al, 2013). The TWL index, introduced by Brake and Bates in 1997 (Brake, D and Bates, G 2002), assesses the environmental heat stress considering various factors. This review aims to highlight the potential of an IoT TWL sensor that provides real-time data to enhance worker safety in tunnel environments.

2.1.1 Monitoring Thermal Work Limit (TWL)

2.1.1.1 Significance of TWL in Tunnel Construction

Numerous, but limited studies have been written demonstrating the significance of TWL monitoring for construction workers. Minimal research has been done specifically on TWL monitoring in tunnel environments. Heat stress can be brought on by the temperatures and humidity in tunnels, which can result in exhaustion, dehydration, heatstroke, and even death (Ahmed 2020; Brake 2002). 13 workplace heat stress-related fatalities occurred in Australia between 2000 and 2015, while 13 occurred in the United States between 2012 and 2013 (Gun, 2019). Monitoring TWL can assist for maintaining worker safety, especially during higher temperatures and humidity days (Roghanchi, P and Kocsis, K, 2018). According to Brake and Bates (2000), TWL monitoring helps in estimating the frequency of work-rest cycles, advised water intake, ventilation needs for tunnel or enclosed workplaces, and necessary personal protective equipment (PPE). Poor TWL monitoring can have serious consequences, including higher accident rates, decreased productivity, more worker compensation claims, and fatalities (Gariazzo et al., 2023). Heat stress can also worsen pre-existing medical disorders and increase the chance of developing chronic illnesses such cardiovascular and respiratory conditions (Montazar et al., 2013). As a result, efficient TWL monitoring, and worker awareness are crucial for both short-term and long-term worker safety.

2.1.1.2 Methodologies for TWL and other Heat Stress Indices

Evaluating heat stress involves considering many different factors like metabolic rate, environmental conditions, clothing, and the individual's acclimatisation to current work environment. Methods such as TWL, and predicted heat strain (PHS) are relatively comprehensive compared to the more commonly applied wet bulb globe temperature (WBGT) index, (Brake and Bates, 2001). Zarea et al. (2019) explores the correlation between WBGT, Tropical Summer Index (TSI), and Universal Thermal Climate Index (UTCI) and worker's physiological characteristics, raising the possibility that there are limitations to the use of these indices for precisely determining worker heat stress. Other studies such as one from Golbabaei and others (2019) developed an outdoor environmental heat index outdoor workers in hot and dry climates, considering both environmental factors and the tympanic temperature as a physiological response to heat.

TWL is used for managing and accessing heat stress and specifies a restricted metabolic rate, indicating the maximum level of heat stress that can be compensated (Bernard et al., 2022). Metabolic rate calculations are different for each individual and there are many factors which can vary metabolic rate between individuals. Miller and Bates (2007) highlight the critical role of hydration and acclimatisation in preventing heat illness in workers, critiquing the limitations of the Wet Bulb Globe Temperature (WBGT). Brake and Bates providing long term advocation for the use of the TWL in the Australian and overseas mining industry. In an earlier study by Bates and Miller (2002), they argue that awareness would show that workers could adequately manage their own exposure and minimise risk of heat stress. In addition, a study conducted at construction sites in Abu Dhabi and Dubai by Ahmed et al (2020) indicated that trained workers were more likely to adjust their own work pace to keep their heart rate within a safe range. Other research has confirmed the efficacy of TWL as a metric for heat stress exposure in Iran and the Middle East (Farshad et al., 2014).

A combined study between Leighton Contractors and Thorzt in 2012 - 2013 on a water treatment facilities project in remote Queensland, Australia, examined the safe implementation of a heat stress program which used TWL to monitor hydration of workers each day. In the program, 10% of personnel in roles requiring manual labour are tested daily using random and voluntary selection, with hydration tests conducted at the start and end of shifts. If a worker failed a hydration test, they were required to hydrate and be retested after an hour and the process continued until the worker was adequately hydrated. Temperatures exceeded 45°C and workers were able to safely continue work at a reduced rate (Ng, 2014). This is a good example of an implementation of TWL for outdoor scenarios. Temperature rises are relatively gradually and are least susceptible to swings in temperature. Zhou et al (2023) methods of evaluating worker's comfort levels when working in road tunnels near

geothermal rock heating. The studies in this section use various forms of heat indices as a tool for assessing worker safety. However, a conspicuous gap in these studies is the absence of continuous monitoring of both the workplace environment and the workers themselves. The Research Project aims to employ a TWL approach to continually assess the working environment for worker safety. The TWL device will provide site safety teams with real-time data, enabling them to make prompt and informed decisions providing necessary notifications to workers as dictated by the evolving conditions and site processes. This approach ensures a proactive stance towards maintaining optimal working conditions and prioritising worker safety.

2.1.1.3 TWL Technologies

Numerous IoT sensor devices have emerged which focus mainly on-air monitoring. To monitor environ-mental conditions, these systems combine measures of temperature, humidity, and air quality. However, there are additional approaches that use readings from wearable sensors. Saidi, A. and Gauvin, C. (2023) conducted a study on the development of real-time monitoring system for early detection of heat stress in workers. They explored historical and current indices like this Research Project and proposed incorporating sensors into fabrics and wearable smart systems to monitor an individual's heat stress. Another study by Shakerian et al. (2021) demonstrated the potential of wearable biosensors in assessing heat strain among construction workers, achieving up to 95% prediction accuracy, although it noted the need for larger sample sizes and subjects with more industry experience for more accurate results. The focus of these studies is on the adoption of wearable sensors, which can provide substantial feedback for users through associated applications. The consequence of escalating this technology to accommodate expansive workforces could be-come quite significant. This research aims to extend its coverage to a broader workforce whilst maintaining precision in TWL measurements. There is now software on the market now which are used to determine heat stress like that from Fame Labsat the University of Thessaly in Greece or PHS from University of Queensland. A detailed analysis into the accuracy of the Fame Lab calculator which PHS methodology for assessing sustainable heat stress exposures from variable such as skin temperature and environmental data to predict heat strain (Ioannou et al., 2019; ISO 7933:2018). Existing software solutions necessitate manual data input, a process that aligns with the current practices observed across numerous construction sites. The Research Project seeks to enhance this process by utilising an algorithm capable of processing both raw data directly from the TWL sensor. Traditional techniques use handheld or fixed stations to collect data and then apply an algorithm to get the TWL reading. Manual measurements could be labour-intensive and prone to mistakes made by humans. Additionally, manual measurements might not account for changes in the environment throughout

the course of the work shift, leading to unreliable estimations of TWL. Examples of contemporary technologies used to determine TWL include handheld devices like the Kestrel 5400 or the Scarlet TWL-1S (Environdata, 2020; Kestrel Meters, 2023; Scarlet-Tech, 2023) shown in Figure 1.

(a) $EnvirondataWeatherStation$ (b) $Kestrel5400$ (c) $ScarletTWL-1S$

Figure 1: Retail and commercial TWL Sensors available from various suppliers (Environdata, 2020; Kestrelmeters, 2023; Scarlet-tech, 2023)

TWL levels are calculated by these devices using algorithms after reading multiple variables (Kestrel, 2023). Fixed weather stations like shown above, provide real time data however they are bulky and restricted to fixed locations. These systems are expensive and not suitable for installation around construction machinery in tunnels. The cost of handheld devices is relatively high, and they don't explicitly provide real-time data to a network, database, or other system. Furthermore, factors like sensor drift, calibration mistakes, and wear and tear from continuous handling can impair the accuracy of these systems (CO2METER.COM, 2023). Another drawback of handheld sensors, although not specifically weather reading sensors, is that the user must enter the potentially dangerous area to take the readings. The design and construction (D&C) device in this research project will be vulnerable to the same risks, but without human interference.

2.1.2 Anemometers

In fluid dynamics research, hot-wire anemometry has been recognised as a reliable method for measuring velocity and turbulence for decades. The hot-wire anemometer (HWA) utilises the principle of convective heat loss to measure air velocity (Brunn, H.H, 1995). The underlying theory is based on heat transfer. The sensor, comprised of a fine resistive wire electrically heated to a stable temperature above the fluid's ambient temperature, registers temperature changes as variations in electrical resistance, which are then correlated to fluid velocity.

There are many studies around the high-resolution capabilities of HWAs. They are capable of resolving extremely small turbulence timescales, making them ideal for atmospheric research and industrial applications (Merzkirch, W., Vitkin, D., Xiong, W., 1998). Their sensitivity to changes in ambient conditions, particularly temperature and pressure, presents a significant obstacle.

Recent advancements in the material sciences have aimed to reduce this sensitivity. Microfabrication techniques employing materials such as platinum and tungsten have resulted in the development of sensors that can withstand harsh environments while retaining a high spatial resolution (Baker, 2002). In addition, new manufacturing techniques have enabled the production of micro-scale hot-wire sensors, thereby expanding their applications to microfluidics, where conventional anemometers would be impractical due to size constraints (Ligrani, P.M, Mahmood, G.I, Harrison, J.L, Clayton, C.M, Nelson, D.L, 2001).

Incorporating signal conditioning circuits and digital signal processing techniques into HWAs has also significantly improved their functionality. These enhancements have made it easier to compensate for the nonlinear characteristics of the HWA, thereby improving measurement precision (Vollmers, 2002). Con-currently, developments in calibration techniques have enabled a more precise and reliable conversion of resistance changes to velocity measurements (Bruun, 1995).

The integration of HWA's with advanced data acquisition systems and computational fluid dynamics (CFD)simulations has resulted in a comprehensive tool for fluid dynamic analysis (Tavoularis, 2005). In conjunction with CFD, real-time, high-frequency data collection enables more detailed flow field analyses, bringing us one step closer to precise flow control applications. Hot-wire anemometer sensors have undergone significant material and technological advancements over the past few decades. With ongoing research focusing on enhancing sensor performance and integrating them with other systems, their role in fluid dynamics is expected to grow in the coming years. As air velocity is one of the key variables for the TWL calculations.

2.1.3 Research Gaps and Future Directions

2.1.3.1 Real-time Monitoring

Existing TWL monitoring techniques, include both manual and automated methods. To measure and determine TWL in real-time, there are currently no portable IoT sensors available. This new sensor will close this gap by giving onsite safety teams quick access to environmental data and TWL levels for risk assessment and decision-making purposes. Real-time monitoring will make it possible to spot patterns and trends in environmental conditions. These patterns and trends can then be used to guide proactive interventions like modifying work schedules, work processes, or engineering controls. While fixed stations may offer real-time data, tunnel environments do not apply to them, and they lack the flexibility for quick and simple relocation for tunnel construction activities like rock-bolting.

2.1.3.2 Integration with IoT Networks

Most current TWL monitoring systems, whether fixed or portable, function as standalone devices. Typically, fixed stations are standalone units that are installed outside and can connect to the LoRaWAN network. Based on the location's remoteness, this restricts their ability to integrate with larger IoT networks. IoT devices are increasingly being used on mine sites because of their dependability, ruggedness, and low maintenance requirements (Ali et al., 2022). Because current handheld devices lack IoT connectivity, there isa chance to investigate the creation of a new device. This gap can be filled by creating an IoT sensor that easily integrates with current IoT networks and construction management systems, enabling real-time data sharing, remote monitoring, and analytics. The creation of advanced decision support systems that use artificial intelligence and machine learning to optimise work schedules, resource allocation, and safety interventions can also be facilitated by integration with IoT networks (Saini et al., 2022).

2.1.3.3 Scalability

Due to their extensive installation and maintenance requirements, many of the TWL monitoring systems currently in use are not easily scalable. By enabling a low, medium, or large-scale implementation across various tunnel sections and/or across various construction sites, an IoT sensor that is small, affordable, and simple to deploy can close this research gap. Given that these projects require careful staging and planning and call for flexible and adaptable TWL monitoring solutions, scalability may be especially crucial for tunnel construction applications.

2.1.3.4 Personalised Monitoring

There are few studies on individualised TWL monitoring. As was already mentioned, most heat indices place a strong emphasis on the calculation of metabolic rate; however, each person's metabolic rate differs significantly from another due to factors like age, weight, and physical fitness, all of which can affect how susceptible they are to heat stress. Furthermore, it does not consider the fact that different tasks are performed at various locations at various metabolic rates (Brake, D.J.; Bates, G.P., 2000). Personalised worker data can be incorporated into an IoT sensor to increase the accuracy of risk assessments and provide information for targeted interventions like individualised work-rest schedules and PPE recommendations. Personalised monitoring could make it easier to implement precision health interventions by using individual data to customise health promotion and disease prevention strategies, like other wearable technologies offered by Apple, Samsung, and Garmin.

2.2 Literature Review Summary

Thermal Work Limit (TWL) monitoring is critical for construction workers, especially in tunnel environments due to risks like heat stress, which can lead to serious health issues and fatalities. Various heat stress evaluation methods exist, with TWL and predicted heat strain (PHS) being more comprehensive than wet bulb globe temperature (WBGT). However, research points to limitations in commonly used indices, necessitating alternative, more precise metrics like TWL. Several studies showcase implementations of TWL monitoring, emphasising its efficacy and the importance of continuous monitoring for optimal working conditions and worker safety. Current IoT sensor devices primarily focus on environmental monitoring. Some studies explore wearable sensor solutions for individual heat stress monitoring, though issues like cost and lack of real-time data network integration persist. Traditional TWL monitoring technologies include handheld and fixed devices, which can be expensive, bulky, and sometimes lack precision due to factors like calibration errors and manual data entry. Hot-wire anemometry is an established method for accurately measuring air velocity, crucial for TWL calculations, with advancements in materials and technologies improving their applications in fluid dynamics. Notable research gaps include a lack of real-time TWL monitoring in portable IoT formats, integration challenges with larger IoT networks, scalability concerns for existing monitoring systems, and a need for more personalised TWL monitoring solutions.

3 Methodology and Parameters for TWL calculations

3.1 TWL Overview and Application

Thermal Work Limit (TWL) is a heat stress index that was developed to limit the physiological strain associated with work in hot environments. It factors in the environmental conditions (such as temperature, humidity, and wind speed), clothing, and the metabolic heat generated by the body due to physical activity. It was conceived to quantify heat stress, particularly tailored for employees performing self-paced tasks. According to Brake and Bates (2002), Thermal Work Limit (TWL) refers to the peak metabolic rate that can be constantly sustained by hydrated, acclimated individuals within a specified thermal environment, without surpassing safe thresholds of core body temperature (38.2°C) and perspiration rate (1.2 kg/hr). The TWL calculation, is a complex algorithm with several formulas and adjustable constants such as clothing insulation and maximum sweat rate. A higher TWL score signifies a greater sustainable work rate concerning thermal stress. Suggested TWL limits and interventions as set out by Brake and Bates are listed in Table 2.

Table 2 Recommended TWL Limits and Interventions (Brake and Bates, 2002)

Recommended TWL limits and interventions for self-paced work		
TWL limit (W/m^{-2})	Name of limit/zone	Interventions
<115 (or DB > 44°C or WB > 32°C)	Withdrawal	• No ordinary work allowed • Work only allowed in a safety emergency or to rectify environmental conditions • Permit to work in heat must be completed and authorized by manager beforehand • Dehydration test at end of shift • Personal water bottle (4-liter capacity) must be on the job at all times
115 to 140	Buffer	• Rectify ventilation or redeploy workers if possible • No person to work alone • No unacclimatized person to work • If work does continue, a corrective action request must be completed and signed by the manager within 48 hrs • Wind speed must be increased to at least 0.5 m/s^{-1} • Dehydration test at end of shift • Personal water bottle (4-liter capacity) must be on the job at all times
140 to 220	Acclimatization	• Acclimatized persons allowed to work, but not alone • Personal water bottle (4-liter capacity) must be on the job at all times
>220	Unrestricted	• No limits on work due to thermal stress

3.2 TWL Formulas and Calculation Methodology

This section provides a detailed look into the derivation of TWL and the calculations to be used for the device. The TWL index developed by Brake and Bates, is based on formulas for convection, radiation, and evaporation derived from the work of Stewart, J.M, Mitchell, D, and Whillier, A (Brake and Bates, 2002). The algorithm incorporates formulas from the American Society of Heating, Refrigeration and Air-Conditioning Engineers (ASHRAE) which is identified in Brake and Bates' work.

The heat balance equation is the foundation for worker in contact with hot areas and is given as:

$$M - W = C + R + E + B$$

Where:

- M is the metabolic rate,
- W is the rate of mechanical work accomplished,
- C is the rate of heat loss from skin due to convection,
- R is the rate of heat loss from skin due to radiation,
- E is the rate of total evaporative heat loss from the skin,
- B is the rate of convective and evaporative heat loss from respiration,

The TWL can be formulated from this balance equation by calculating each part separately and combining. Essentially, TWL is given by *M* in this equation. Noting in a steady-state scenario, both S terms are zero. The term W is typically assumed to be zero.

The TWL shall be calculated using the following steps.

1. Calculate the heat loss due to respiration using:

$$B = 0.0014\,M\,(34 - ta) + 0.0173\,M\,(5.87 - pa)$$

   Where:

   - ta is the dry bulb temperature of ambient air in °C.
   - pa is the partial water vapor pressure in ambient air in kPa.

2. Calculate radiation losses *R* (for a naked person):

$$R = h_r f_r (t_{skin} - t_{rad})$$

   Where:

$$hr = 4.61\left[1 + \frac{(t_{rad} + t_{skin})}{546}\right]^3$$

   and,

   - f_r is the posture factor (dimensionless), typ 0.73 for a standing person.
   - t_{rad} is the average radiant temperature in °C.

3. Calculate convection losses *C* (for a naked person):

$$C = h_c(t_{skin} - t_a)\frac{W}{m^{-2}}$$

Where:

$$hc = \frac{0.608P^{0.6}V^{0.6}\frac{W}{m^2}}{K^{-1}}$$

Where:

- *P* is the ambient barometric pressure in kPa
- *V* is the wind speed over the skin in m/s^{-1}

4. Calculate the heat transfer *H* from the deep body core to the skin:

$$H = K_{cs}(t_{core} - t_{skin})$$

Where:

$$K_{cs} = 84 + 72\tanh\left[1.3\ (t_{\Sigma} - 37.9)\right]$$

And,

$$t_{\Sigma} = 0.1\ t_{skin} + 0.9\ t_{core}$$

And,

- T_{core} is maximum core temperature under normal working conditions, typ 38.2°C.
- t_{skin} is the skin temperature in °C.

5. Calculate the sweat rate S_r and evaporation rate:

$$Sr = 0.42 + 0.44\ tanh[1.16\ (t_{\Sigma} - 37.4)]$$

Using the latent heat of evaporation of sweat the actual evaporation rate *E* can be calculate by making the following assessments.

For, $Sr = Emax < 0.46$ $\quad E = \lambda Sr$

For, $0.46 \leq \frac{\lambda S_r}{E_{max}} \leq 1.7$ $$E = \lambda S_r \, exp\left[0.4127 \times \left(\frac{1.8\lambda S_r}{E_{max}} - \, 0.46\right)^{1.168}\right]$$

For, $\frac{\lambda S_r}{E_{max}} > 1.7$ $$E = \, E_{max}$$

6. Calculate TWL, assuming *W* is zero:

$$M \, = C \, + \, R \, + \, E \, + \, B$$

And finally,

$$TWL \, = M$$

4 Sensor Positioning Optimisation

4.1 Tunnel Construction Overview

An appropriate location for the anemometer is required to both secure accurate airflow measurements and ensure it is free from influence from vehicle movement air disruptions and also prevent it from being struck by construction plant and equipment. The tunnel shape is a horseshoe profile with a circular arch roof, with dimensions ranging from 12 to 18 meters wide, and heights varying between 7.5 meter to as high as 12 meters at the centre of the crown in some locations. Generally, the sofit measures to around 6 meters. The true tunnel profile is shown in Figure 2.

Figure 2 Tunnel profile - horse shoe shape cut in sandstone substrate.

The rock substrate is cut using a road header machine and the walls and crown are then cover with fibre-reinforced sprayed concrete, creating a rough and bumpy surface. This creates a unique setting for air dynamics. When air moves through our horseshoe-shaped tunnel, Complex flow patterns are created close to the surface. This is unique structural design creates complex air flow patterns. In addition, Mechanical and Electrical (M&E) equipment including deluge systems, signs, cable ladders, and lighting fixtures, all attached to the crown, also complicate the measurement of airflow. In particular, the undulated wall surfaces disrupt the airflow and create turbulence.

4.2 Location Optimisation

Tunnel structure and M&E equipment causing variable air velocities can cause the anemometer sensor to produce skewed measurement and therefore TWL output as it would fail to capture the average airflow within the tunnel. Obstructions also lead to localised alterations in airflow, creating regions of accelerated or slowed air movement. Such changes can influence the anemometer readings, so a location with minimal impact of these obstructions is preferred. Ideally, the anemometer should be placed in a clear pathway of airflow, far from any immediate disruptions whilst not impeding access to any construction plant or equipment. Therefore, the mounting height for the anemometer is also a major consideration, especially given the daily movement of plant and machinery within the tunnel. To avoid physical damage to the anemometer, it should be installed at a height that safely clears these vehicles but still provides accurate readings that are not affect by vehicular air flow. Location optimisation considered the performance, functionality, and safety characteristics. Location selection therefore adhered to the following criteria:

- Mounting no closer than 1m from tunnel wall, soffit, or crown.
- Mounting height of no less than 5 meters.
- Clear of all M&E obstructions or installations.
- Closest to average airflow.
- Have the least variance airflow.

4.2.1 Location Mapping

A systematic analysis was carried out to identify the optimal position for the anemometer to acquire an consistent average wind speed with minimal variance. Wind speed readings were taken in a structured grid formation of 1m x 1m intervals starting at a set height of 5.0m above the paving level. This is considered as the safe area above the vehicle envelop, ensuring coverage of potential wind fluctuations. The grid allowed for a spatial understanding of the wind flow throughout the tunnel, pinpointing areas of steady laminar flow as opposed to more turbulent zones. It should be noted that there are many different variances of tunnel sizes and shapes depending on civil design, rock substrate, and M&E equipment. A baseline test was performed in a designated region of the tunnel measuring 5m in width and 2m in height, situated 1.5m above the paving height. The grid formation and reference test can be seen in a section of tunnel in Figure 3. Noting this was not the location of test but a representation of test area as it clearly shows the tunnel profile.

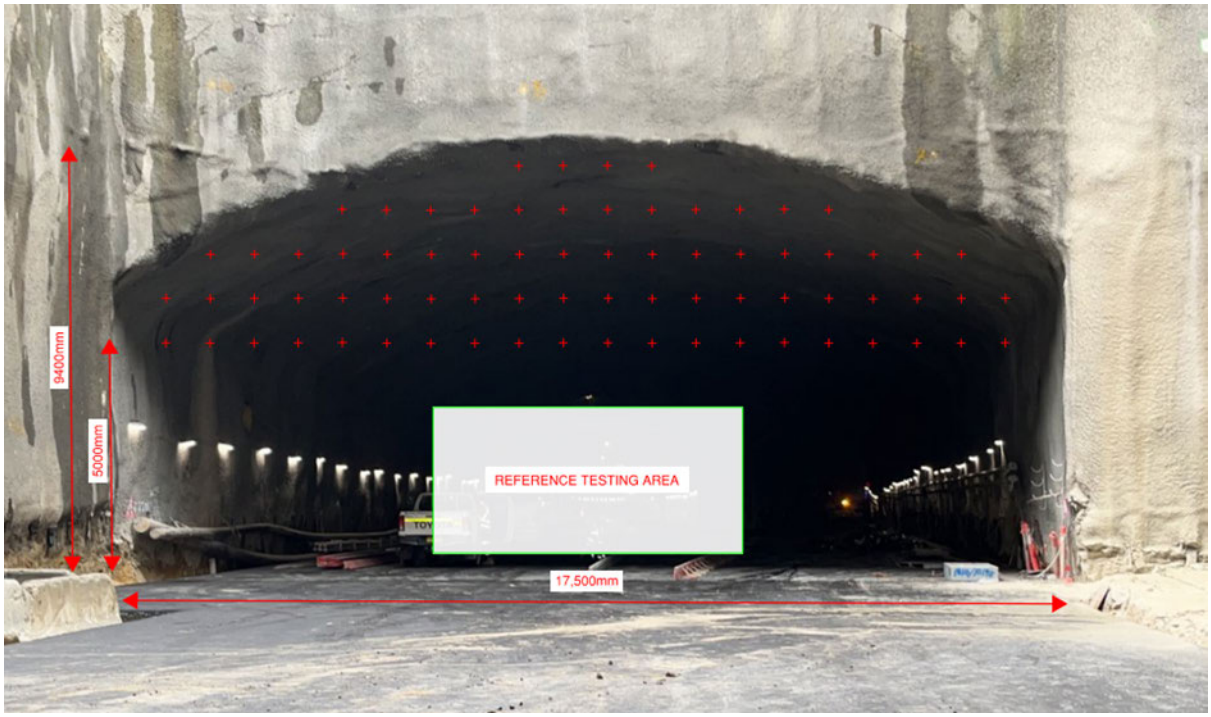

Figure 3 Wind speed typical testing pattern and reference test area.

The reference test area was used to evaluate the consistency and reliability of the wind speed readings across the testing section of the tunnel to identify desired location that meets design criteria. The research aimed at ensuring that the anemometer placement would yield reliable and consistent readings, thereby contributing to the accuracy and integrity to the measurement data of the TWL prototype.

4.2.2 Data Collection

All wind speed measurements taken in the section of the tunnel were conducted using a calibrated Kestrel 5400 meter. An elevated work platform was used to access and acquire measurements at various heights and locations. Table 3 lists the wind speed readings recorded as per the grid formation. Note NaN depicts rock substrate areas.

Table 3 Prototype positioning wind speed measurements.

Height above paving (m)	Lateral section position (m)											
	0.5	**1.5**	**2.5**	**3.5**	**4.5**	**6.5**	**7.5**	**8.5**	**9.5**	**10.5**	**11.5**	**12.5**
9.0	NaN	NaN	NaN	0.2	0.5	0.3	0.2	0.4	NaN	NaN	NaN	NaN
8.0	NaN	NaN	0.4	0.5	0.2	0.5	0.6	0.6	0.5	0.2	0.3	NaN
7.0	NaN	0.3	0.2	0.6	0.6	0.6	0.7	0.6	0.5	0.4	0.4	0.2
6.0	0.5	0.2	0.6	0.7	0.7	0.7	0.7	0.7	0.6	0.4	0.2	0.4
5.0	0.2	0.5	0.7	0.7	0.6	0.8	**0.7	0.7	0.6	0.5	0.2	0.5

** denotes optimal location from analysis.

Table 4 lists the wind speed readings recorded for the reference test are in line with the grid formation test pattern.

Table 4 Wind speed measurements for reference test zone.

Height above paving (m)	Lateral section position (m)				
	4.0	**5.0**	**6.0**	**7.0**	**8.0**
4.0	0.7	0.8	0.8	0.7	0.7
3.0	0.7	0.7	0.7	0.7	0.8
2.0	0.7	0.8	0.7	0.7	0.7
1.0	0.7	0.8	0.8	0.7	0.7

4.2.3 Data Analysis

The scope of this investigation encompasses two distinct areas:

1. Sensor Test Area: Positioned starting 5m above the paving surface to tunnel crown and sofit areas.
2. Reference Test Area: Located at the geometrical centre of the tunnel cross-section.

The indication of "NaN" within Table 3 is indicative of rock substrate regions, thus illustrating positions where measurements are not feasible due to solid obstructions.

Utilising the wind speed data collected from Table 3 and Table 4, the optimal placement for the anemometer sensor can be found. The positioning criterion included two parameters:

- Proximity to the average wind speed derived from the Reference Test Area.
- Minimal deviation from adjacent measurements within the Sensor Test Area.

A summary of the results from the statistical analysis are found in Table 5.

Table 5 Summary of results from statistical data analysis

Calculation	**Value**	**Unit**
Average Wind Speed – Test Zone	0.7267	m/s
Average Wind Speed – Reference Zone	0.4792	m/s
Variance	0.0371	Unitless
Standard Deviation to adjacent measurements	0.2333	Unitless
Average Standard Deviation	0.2267	Unitless
Combined deviation	0.0047	Unitless

Based on the analysis, the findings pointed to Row 5, Column 7 as the optimal location for the anemometer. This specific position produced a combined deviation of 0.047, showing consistency with both the average wind speed from the reference test area data and the wind speed values from surrounding cells. This location ensures a balanced representation of the tunnel's ventilation dynamics and promotes data accuracy for the technical analyses, and therefore the optimal location for the prototype to be install.

5 Design and Development

5.1 System Overview

5.2 Microcontroller Selection

Ten microcontrollers were assessed as part of the analysis. Criteria assessed were hardware and software capabilities, suitability for IoT application and Integrated Development Environment (IDE). A suitable microcontroller for controlling temperature, humidity, and wind sensors is found through this analysis. IoT cloud platform integration was favoured for the Project. The evaluation covers well-known microcontrollers like the Arduino, Raspberry Pi, and ESP32 in addition to a few lesser-known development boards like the Particle Photon and Asus Tinker Board 2. All data taken direct from their respective datasheets. A full comparison is summarised in **Error! Reference source not found.**.

Table 6 Microcontroller comparison summary

Name	Processor	Communication Protocol	Inputs	Outputs	Analogue I/O	Proprietary IoT Platform	Estimated Cost (AUD)
Arduino UNO WiFi Rev 2	ATmega4809 (8-bit AVR RISC)	WiFi (802.11 b/g/n)	15	15	6 (10-bit)	No	$45
Arduino UNO Rev3	ATmega328P (8-bit AVR RISC)	None (requires shield)	14	14	6 (10-bit)	No	$25
Arduino Nano 33 IoT	SAMD21 Cortex-M0+ (32-bit ARM)	WiFi, Bluetooth	14	14	8 (12-bit)	Yes	$35
Adafruit Feather Huzzah	ESP8266 (32-bit Tensilica Xtensa	WiFi (802.11 b/g/n)	17	17	1 (10-bit)	Yes	$22
Raspberry Pi	ARM Cortex-A72 (1.5 GHz, Quad)	None (requires adapter)	40	40	N/A	No	$45
Raspberry Pi Zero W	ARM Cortex-A53 (1 GHz, Single)	WiFi, Bluetooth	40	40	N/A	No	$15
ESP32-C3 WROOM	ESP32-C3 (32-bit RISC-V)	WiFi, Bluetooth	34	34	6 (12-bit)	No	$10
Particle Photon	STM32F205 ARM Cortex M3	WiFi (802.11 b/g/n)	18	18	8 (12-bit)	Yes	$25
Asus Tinker Board 2	ARM Cortex-A72 (1.8 GHz, Quad)	Ethernet, WiFi, Bluetooth	40	40	N/A	No	$110
Omega2	MIPS24k (580 MHz)	WiFi, Ethernet	18	18	N/A	Yes	$15

5.2.1 Microcontroller Selection Rationale

The Arduino Nano 33 IoT has been selected for the Research Project due to its hardware feature combination, user-friendliness, and suitability for IoT applications. The board is suitable choice for IoT projects that need both local and remote communication because it includes a SAMD21 CortexM0+ microcontroller with built-in Wi-Fi and Bluetooth connectivity. The Arduino Nano 33 IoT is the best option for the research project because of its balance between processing power, connectivity options, development support, and affordability.

5.2.2 Temperature and Humidity Sensor Selection

The DHT22, SHT45, and BME280 temperature and humidity sensors, as well as their compatibility with the Arduino Nano 33 IoT microcontroller, are compared in this section of the analysis. The evaluation looks at the sensor's specifications, including supply voltage, ranges and accuracy for temperature, humidity, and atmospheric pressure, as well as power usage and response times. The availability of documentation and tutorials, pinout configuration, scaling, and communication protocols for each sensor are also covered. A summary of these sensor is shown in Table 7. All specifications are from their respective datasheets in Appendix H.

Table 7 Atmospheric sensor comparison table

Sensor Model	Supply Voltage (VDC)	Temp. Range (°C)	Temp. Accuracy (°C)	RH Range (%)	RH Accuracy (%)	Atm. Pressure Range (hPa)	Atm. Pressure Accuracy (hPa)	Power Usage
DHT22	3.3 - 6	-40 to 125	±0.5	0 - 100	±2	N/A	N/A	1.5mA (max)
SHT45	2.4 - 5.5	-40 to 125	±0.1	0 - 100	±1.5	N/A	N/A	0.9µA (typical)
BME280	1.71 - 3.6	-40 to 85	±0.5	0 - 100	±3	300 - 1100	±1	0.6µA (typical)

5.2.3 Temperature and Humidity Sensor Selection Rationale

The Adafruit BME280 sensor is the choses sensor because it measures atmospheric pressure which enables more precise calculations for TWL. Like the DHT22, the BME280 provides a wealth of tutorials and support materials, making it appropriate for new users. Additionally, the BME280 supports both the I2C and SPI communication protocols and integrates with the Arduino Nano 33 IoT microcontroller. This adaptability makes scaling up in bigger projects easier. In conclusion, the BME280 is the best option for this project because of its features, usability, and affordability.

5.3 Controller Circuit

The main controller circuit consists of the Ardunio Nano 33 IoT microcontroller, the CTA sensor circuit, power and control wiring, and the I2C communications wiring to the BME280 sensor. See Figure 4 for complete circuit board layout for reference. The the Ardunio Nano 33 IoT microcontroller is the PCB module on the left-hand side and the resistors, opamp and transistor on the right-hand side make up the anemometer circuit. The anemometer circuit design is detailed in Anemometer Design. All components are soldered and joined on a blank circuit board. The left-hand side of the Arduino Nano are the power in, analogue, and I2C comms pins. The 9V power supply is segregate to the bottom left-hand corner of the circuit board to minimise interference to the 2 sensors. No additional shielding was required.

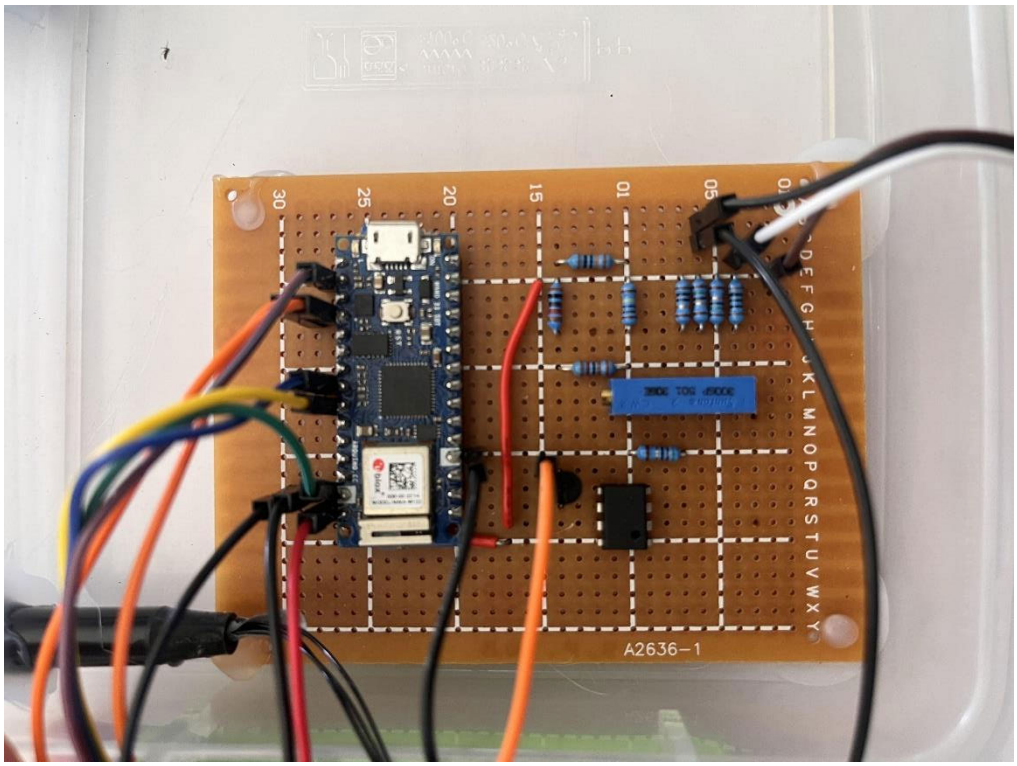

Figure 4 Prototype controller circuit board layout

5.4 Anemometer Design

5.4.1 FS7 Anemometer Sensor

Due to occasional very low airflows, a constant temperature anemometer was selected over the conventional 3-cup or propeller-type anemometers for this project. The specific constant temperature anemometer, FS7.0.1L.195, is a mass flow sensor used for various gases. Low power consumption (60mA, 135mW during heating), high resolution capabilities (0.01m/s), a wide range (0 - 100 m/s), and high accuracy (<3%) met selection criteria for the anemometer. The sensor is mounted in a duct

mounted flow probe fixed to side of the housing. The sensor element is designed so that the element runs parallel to the direction of air flow as per manufactures specifications. The sensor must be aligned so the flow passes over the active sensor surface. See Figure 5 and Figure 6 for probe mounting and sensor element. The full specifications can be found in the datasheet in Appendix H

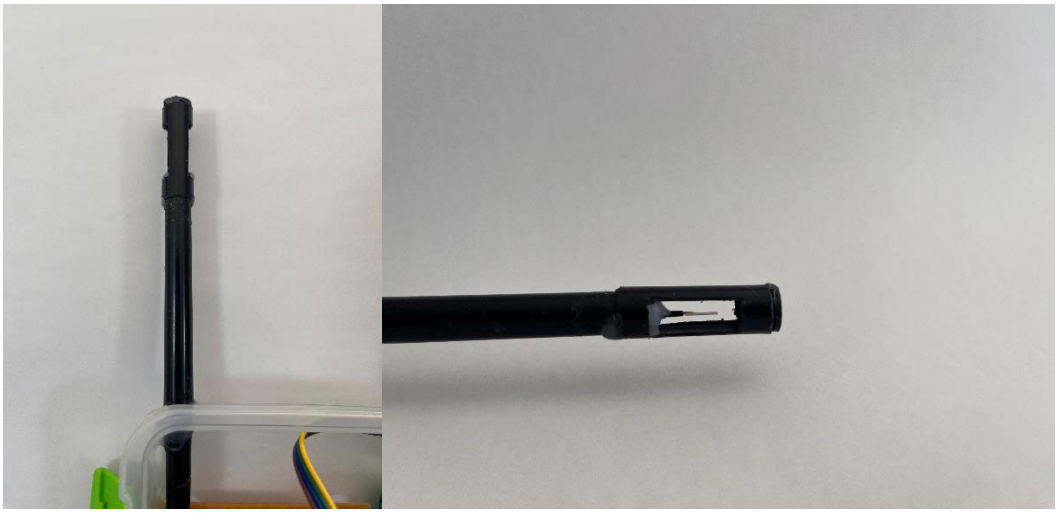

Figure 5 Anemometer probe

Figure 6 FS7 CTA sensor

5.4.2 Anemometer Circuit

The circuit employs a feedback circuit for temperature regulation of the heater situated on the low sensor. This is included to reduce the impact of the thermal energy dissipation of the heater during air velocity changes. This control allows the sensor to maintain a uniform temperature gradient between the heater and the temperature sensor allowing consistent and accurate output voltage.

The power output is converted to the voltage output signal through a bridge circuit. After calibration, flow rate can then accurately be calculated or converted from the output signal. An integrated Pt1200 temperature sensor is used in the sensor to offset the medium temperature. The whole sensor is a mere 6.9mm (long) x 2.4mm (wide) x 0.2mm (thick). See Appendix H for full specifications.

The circuit diagram for the anemometer sensor is show in Figure 7.

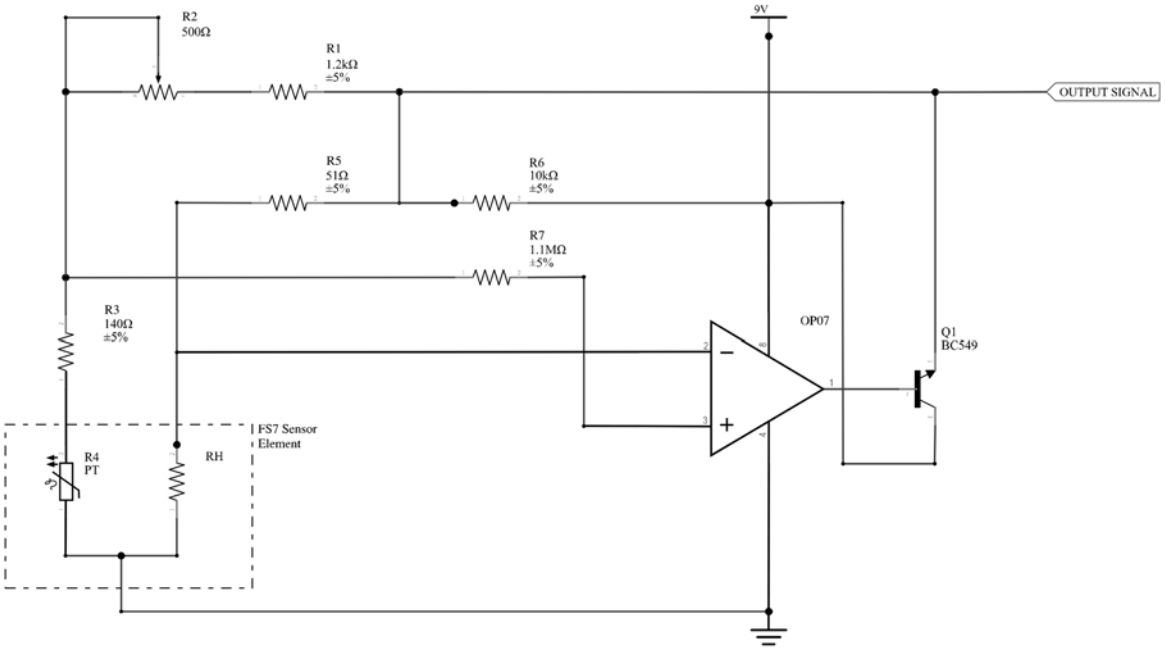

Figure 7 Constant temperature anemometer circuit schematic

The circuit for the anemometer consists of the following components:

- FS7.0.1L.195 iST Thermal gas flow sensor
- R1 – 1.2kΩ resistor
- R2 – 500Ω variable resistor
- R3 – 140Ω resistor
- R5 – 51Ω resistor
- R6 – 10kΩ resistor
- R7 – 1.1MΩ resistor
- BC 539 NPN Transistor
- OP07CP Operational Amplifier

R3 resistor set the temperature difference between the sensor heater and the medium (air). The R2 resistor, is used for calibration purposes adjust output voltages in line with known air velocities. R7 resistor acts as a stabiliser for the circuit.

5.5 Housing

The main housing for the TWL sensor prototype was sourced from a Sistema sandwich container Figure 8. When the sensor is not attached, the housing meets an estimated IP66 standard, indicating full dust protection and resistance to powerful water jets. However, with the sensors attached, the protection rating is reduced to IP52, which safeguards against dust ingress and vertically falling water droplets. This level of protection was necessary to guard the prototype against water dripping from the tunnel crown.

Figure 8 Prototype housing (Woolworths, 2023)

To further prevent water ingress, the sensor openings were strategically positioned at the bottom of the housing. An in-line garden watering filter screen was incorporated to provide an atmospheric to the housing while minimising the entry of both dust and water. See Figure 9 for anemometer and atmospheric probe.

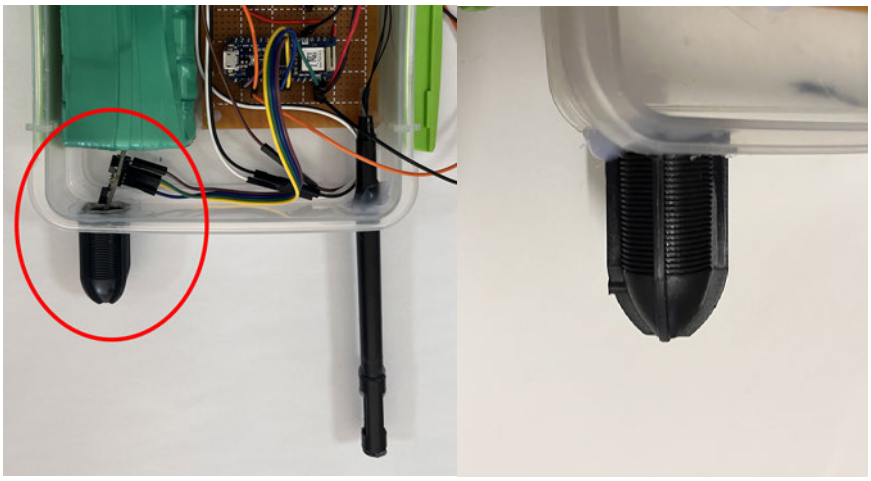

Figure 9 Dust screen and atmospheric barrier

Inside the housing, there is adequate space to accommodate the customised circuit board, battery, and associated wiring. The housing is easily opened and closed, facilitating access for maintenance

and testing procedures. The clear housing provides clear visibility to the onboard LED indication on the Arduino Nano 33 IoT microcontroller.

The total cost for the housing was $5.00 AUD (Woolworths) and $3.25 AUD (Bunnings) for the in-line filter screen.

5.6 Battery and Power Usage

Based on calculations, the system's power consumption was calculated at 75mA when full power input is directed to the Arduino Nano IoT microcontroller, considering both an analogue and I2C input. However, measurements taken using a Fluke 179 multimeter showed actual usage to be 66mA during the periods of processing and heating the anemometer and BME280 elements. The minimum current draw from the sensor was recorded at 21mA, noting that sleep mode is not utilise on the Arduino microcontroller.

The power source for the prototype comes from a battery bank comprising five Energizer MAX batteries. Each of these batteries has a capacity of 600mAh, totalling the capacity to 3000mAh for the battery bank, see Figure 10.

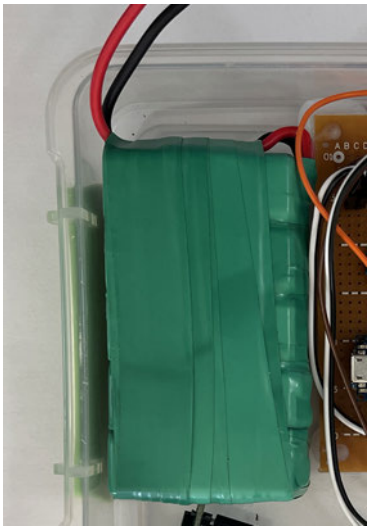

Figure 10 Battery bank - 5 x 9V (Energizer MAX)

Under continuous operation at 60mA, each battery is projected to last 8 hours, at which point the battery voltage drops to 6.0V, see Figure 11 for discharge performance curve. It is important to note that this voltage drop affects the accuracy of the anemometer sensor. However, the BME280 sensor's voltage remains relatively consistent, and its performance is largely unaffected until the battery voltage drops below the 5.0V mark.

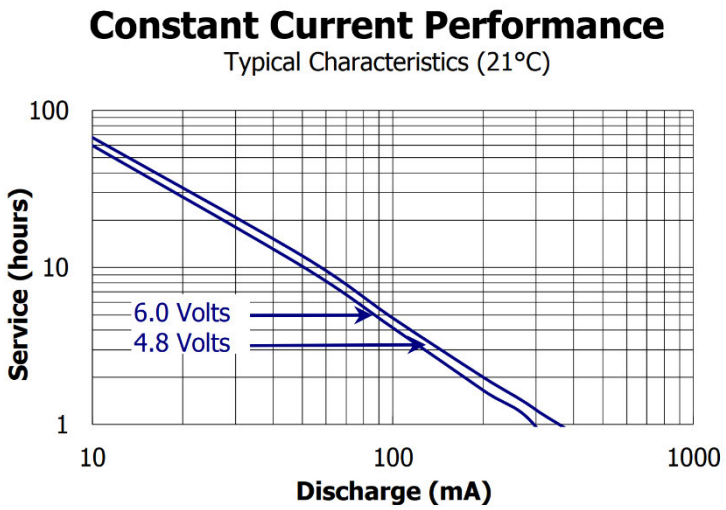

Figure 11 Battery discharge curve for Energizer MAX 9V batteries (Energizer, 2023)

Considering a continuous operational current of 66mA, the battery bank is estimated to last approximately 45.45 hours, or 1.89 days. By adjusting the update and heating intervals to 5-minute durations, the average hourly current reduces to 21mA. This adjustment consequently extends the battery's capacity to approximately 142.86 hours, or 5.95 days. Further adjusting the run and heating times for the Arduino and sensors to 10 minutes reduces average significantly to just 11mA, increasing battery capacity to 272.72hrs (11.4 days) assuming a linear approach.

The introduction of a sleep mode could further mitigate power consumption. However, it's pertinent to highlight that employing the use of this could compromise the accuracy of the anemometer sensor due to the required heating times.

5.7 Programming and Coding

This section examines the software design for the TWL prototype. A critical review of the code will identify its key features, error-checking mechanisms, fail-safes, and potential areas for improvement. The full code can be found in Appendix F.

5.7.1 Libraries and Dependencies

The code employs several libraries:

- Wire.h: Enables I2C communication with devices.
- Adafruit_Sensor.h & Adafruit_BME280.h: BME280 sensor libraries
- thingProperties.h: Defines properties related to the Arduino IoT Cloud.
- TWLOutput.h: Stores TWL calculation data in matrices

5.7.2 Global Variables and Calibration Constants

The BME280 sensor is initialised using Adafruit_BME280 bme. Calibration offsets for temperature (temperatureOffset) and humidity (humidityOffset) are defined to fine-tune sensor readings during testing. Constants related to wind speed calculation (V_0, k, and n) are initialised. An array for the last NUM_READINGS (set to 5) for temperature, humidity, and wind speed is defined to maintain a recent history of readings.

5.7.3 System Initialisation

The setup() function includes serial communication rate and then check for the presence of the BME280 sensor over I2C. Averaging data is initialised to zero readying for average value error checking. The code then establishes the connection to the Arduino IoT Cloud and prints debug information if any.

5.7.4 Continuous Monitoring and Data Acquisition

Sensor readings for temperature, humidity, and wind speed are obtained from the sensors and converted to usable outputs. Validation checks are performed on these readings to ensure they lie within physical range of the device. A warning is printed for any reading that falls out of range. If all readings are valid, the TWL value is computed using the getTWLValue function. The program then compares the current readings to their recent averages using a 5-point moving average method to detect significant variances. It provides warning if any variance is detected. Valid readings are updated and sent to the Arduino IoT cloud and printed to the serial monitor.

5.7.5 Error Checks and Fail-safe

5.7.5.1 Sensor validation

The code checks if temperature, humidity, and wind speed readings are within valid ranges.

5.7.5.2 Variance check

The code flags if a new reading significantly deviates from the average of recent readings.

5.7.5.3 Sensor initialisation

The system will stall if the BME280 sensor is not detected, preventing any invalid operations with missing data. This is tested in the

5.7.6 Utility Functions

The followings list and provides summarised explanation for each function:

- calculateAverage(): Computes the average of an array of readings.
- VoltageToWindSpeed(): Transforms raw voltage values to wind speed values.
- Functions (getWindSpeedIndex, getTemperatureIndex, getHumidityIndex) are used to map raw sensor values to indices, used in matrix-based TWL calculations.
- getTWLValue(): Determines the TWL value based on wind speed, temperature, and humidity.

5.7.7 Areas for Improvements

5.7.7.1 Enhanced Calibration

While the code includes basic calibration offsets for temperature and humidity, a more comprehensive calibration procedure can ensure better accuracy. Result for calibration testing are found in Section 6.

5.7.7.2 Additional Error Handling

Introducing a retry mechanism during sensor initialisation can add robustness to the system. .

5.7.7.3 Memory Efficiency

Storing readings in arrays consumes memory. Given that embedded systems typically have limited memory, alternative data structures or algorithms could be explored for efficiency.

5.7.7.4 Adaptive Sampling Rate

An adaptive sampling rate based on changes in environmental conditions might provide more timely updates during rapidly changing conditions and save power during stable conditions.

5.7.7.5 Coding Summary

The prototype code offers a robust starting point for a TWL sensor prototype, integrating sensor interfacing, data validation, and cloud connectivity. With the identified areas for improvement, the system can be further refined to enhance its reliability and efficiency in real-world applications within construction tunnels.

5.8 IoT Cloud Platform and Dashboard

5.8.1 Overview of Arduino IoT Cloud and Dashboard

The Arduino IoT Cloud is a platform designed to provide a streamlined environment for developing and overseeing Internet of Things (IoT) projects. Central to its offering is the ability to securely manage data, configure devices, and present real-time visualisations via a dashboard (Arduino, 2023). Arduino IoT Cloud was employed for the Project to facilitate communication between the TWL sensor prototype and the user interface. By utilising the dashboard feature on the platform, it allowed for the real-time display of data, using widgets to visualise the parameters and measurement readings.

5.8.2 Connection Using thingProperties.h File

Connection to the Arduino IoT Cloud is established using the thingProperties.h file. This file is automatically generated when creating a new "Thing" (device) on the Arduino IoT Cloud platform. The thingProperties.h file contains definitions and initialisations of cloud-bound variables, facilitating the seamless integration between the Arduino code and the cloud (Arduino, 2023). During runtime, the platform-specific library reads these cloud-bound properties, ensuring data is transmitted between the device and the cloud.

5.8.3 Arduino Nano 33 IoT WiFi Connectivity

The Arduino Nano 33 IoT is equipped with a built-in WiFi module, which was utilised to connect the sensor to the tunnel’s temporary WiFi network. Credentials for the WiFi connection, including the network SSID and password, were stored in a separate header file called “secret.h”. This ensures that sensitive connection details are removed from the main application code, providing a higher degree of security for the prototype.

5.8.4 Dashboard and Widgets

The dashboard was customised for the Project's designed output display data through four primary widgets:

- *Temperature*
- *Humidity*
- *Wind Speed*
- *TWL Index*

The dashboard layout and outputs are displayed in Figure 12.

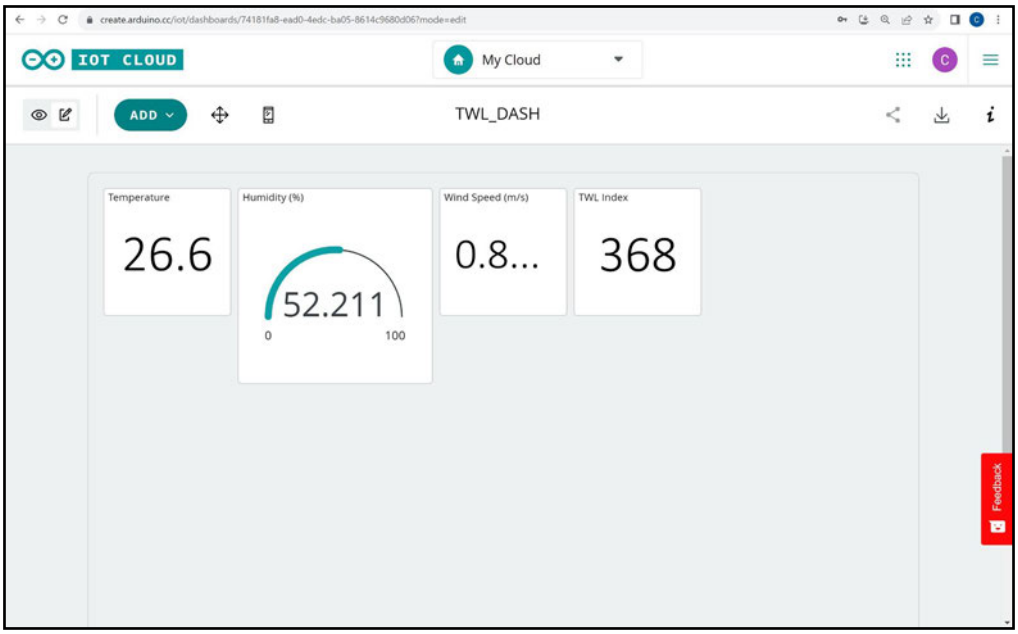

Figure 12 The TWL Sensor prototype Arduino IoT Cloud dashboard

5.8.5 Subscription Details

Arduino Clout offers a free subscription tier for small scale project's which was employed on the Project. The free subscription allowed for the registration of one Thing (device) and supported up to five cloud-bound variables. A notable limitation of this free tier is that it only offers 24hr data retention. Therefore, to prevent data loss, historical data had to be downloaded daily to ensure consistent data was captured for data analysis.

6 Calibration and Testing

6.1 Anemometer Calibration

This section outlines the experimental procedure established to calibrate the CTA sensor. Both workshop and field testing were carried out to ascertain the accuracy of this calibration. A calibrated Kestrel 5400 meter served as a benchmark to validate the results. Specific constants from King's Law were determined for wind speed conversions in relation to output voltage used in the prototype's coding.

The accuracy and reliability of fluid dynamics measurements largely depend on the calibration of constant temperature anemometers, as they are particularly sensitive to their operating conditions. To determine the voltage output at a given air velocity, King's law is used.

$$U = U_0 \cdot \sqrt{1 + k \cdot \overline{v}^n}$$

Where:

- U is the output signal voltage.
- U_0 represents the value of constant temperature difference (ΔT) between the heater and fluid at no flow speed.
- k is the fluidic dependent constant.
- v is the fluid velocity.
- n is a constant determined during calibration (generally between 0.48 – 0.52)

To calibrate the FS7 constant temperature anemometer sensor, the sensor was inserted into the centre of a 1000mm long x 90mm conduit and tested with varying air velocities. The conduit provided even air flow across the sensor. The sensor was mounted parallel in the direction of airflow to minimise angular response. The setup for calibrating the sensor is shown in Figure 13.

Figure 13 Setup for calibrating the CTA sensor.

The sensor was mounted in a probe tube like arrangement in Figure 14.

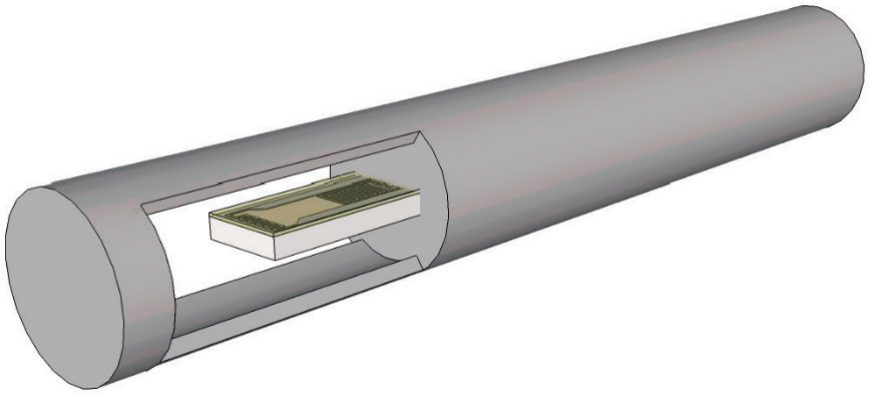

Figure 14 Constant temperature anemometer general probe mounting arrangement (iST, 2023)

The probe was inserted into the test air tunnel (conduit) for the test, positioned in the centre of the tube. This arrangement is shown in Figure 15.

Figure 15 Wind tunnel testing apparatus for CTA sensor calibration

A 2-speed hair dryer was used to provide air velocities through the wind tunnel conduit at speeds from 0.1 – 6m/s. To achieve variable speeds, the 2-speed control was used along with restricting intake on the hairdryer. Each time, velocities were checked by removing the probe and checking air velocity with the Kestrel 5400 meter. The probe was then re-inserted for a period of 1 minute before checking voltage, allowing significant time for temperature balancing of the sensor.

The sensor circuit's maximum output 7.9V (not connect), however the Arduino A0 pin can only accept a maximum input of 5V. To account for this, a maximum air velocity was set for the sensor at 6m/s, which is 600% higher than its typical operating conditions. This adjustment reduced the sensor's maximum output voltage to 5.00V. To determine the output voltage at 0m/s, the sensor was covered, revealing an output of 3.2V. Thus, the sensor's voltage range was set between 3.2V and 5.0V. Given the exponential nature of the calibration readings, measurements were taken at 0.1m/s increments to determine the calibration curve. Specifically, the voltage outputs were determined for velocities at 0m/s (3.20V), 3m/s (4.60V), and 6m/s (4.99V). These results facilitated the calculation of the linearised constants n and k.

The values n and k are calculated using flow calibration at 3 separate points:

1. Initial value or zero flow – $U_0 = 0$

   Using the variable resistor (R2), the output voltage was set to 5 volts with 6m/s airflow. The airflow was removed, and the output voltage was taken at 0m/s airflow with sensor covered, which was 3.20V.

2. Mid-point of measuring range (3m/s)

   At 3m/s the output voltage is recorded as 4.60V.

3. End point of measuring range

   At 6m/s the output voltage was recorded as 4.99V.

Calculating *n* is then deduced to 2 taking equations 2 and 3 from the output voltage readings.

$$n = \frac{\overline{v}_{50\%}}{\overline{v}_{100\%}} = 0.5$$

Finally, *k* can then be found by using the following equation:

$$k = \frac{\left(\frac{U_{50\%}}{U_0}\right)^2 - 1}{\overline{v}_{50\%}^{\,1/n}} = \frac{1.0157}{3^{0.5}} = 0.58641$$

A full calibration curve during testing and calibrating is shown in Figure 16.

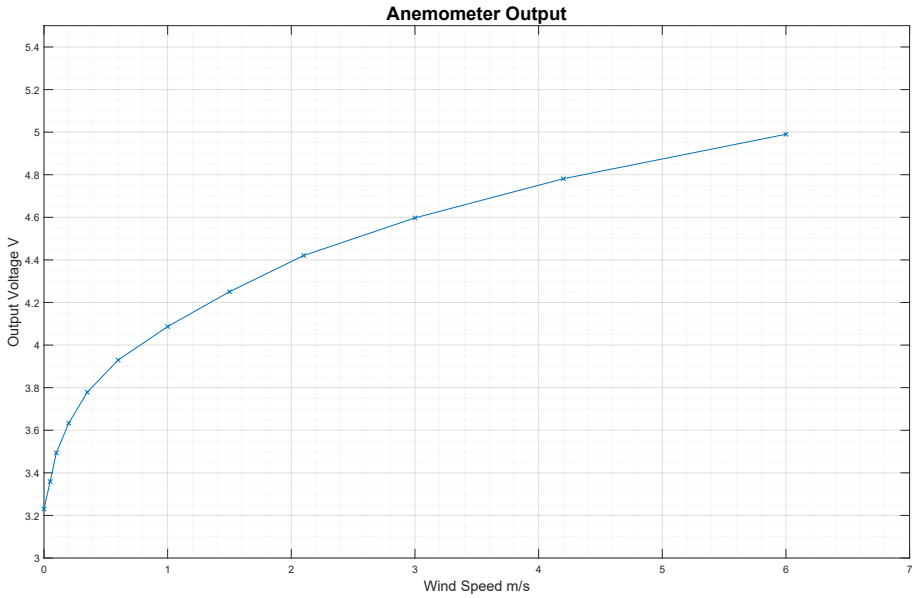

Figure 16 Anemometer calibration curve

Calibration was verified by checking results by linearisation. Using U_0, k, and n, the linearised characteristic is found for full range calibration. To check by linearisation, the reverse function of **Error! Reference source not found.** is used.

$$\overline{v} = \frac{[(U - U_0)(U + U_0)]^{1/n}}{\left(k^{1/n}\right) \cdot U_0^{2/n}}$$

Where:

- v is the fluid velocity
- U is the measure output signal voltage
- U_0 is initial voltage at 0m/s 3.24V

Using real measured n, k, and U_0 values with **Error! Reference source not found.**, the linearisation curve in Figure 17 is attained.

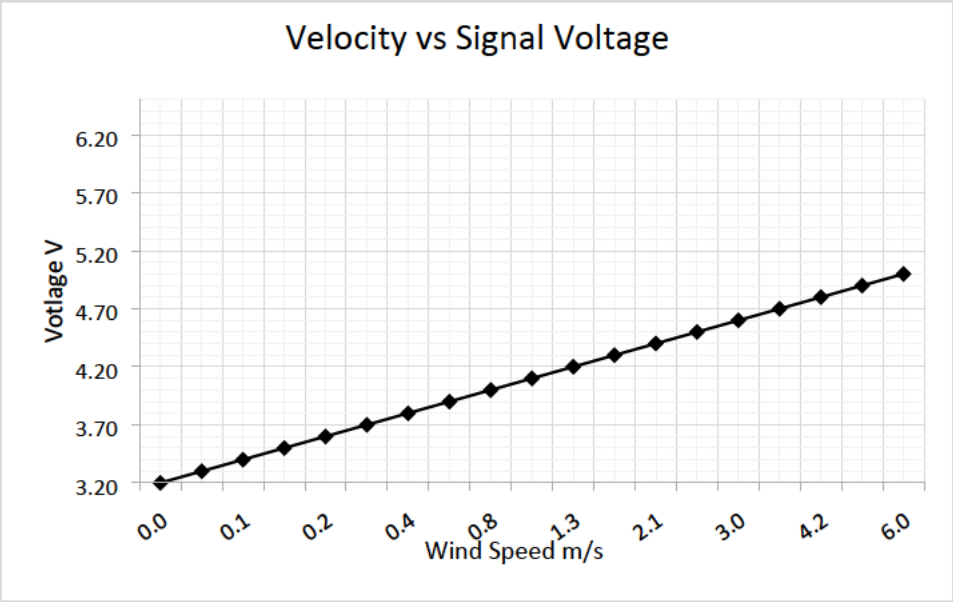

Figure 17 Linearised calibration curve

6.1.1 Calibration Summary

The calibration of the constant anemometer was successfully completed, achieving accuracy within <2% of the known calibrated meter, the Kestrel 5400. From this process, values for n, k, and Uo constants were derived. These constants provided the foundation for the real-time conversion of analogue sensor voltages to wind speed. Furthermore, calibration and linearisation curves for the anemometer were developed and plotted, revealing no inconsistencies in the data.

6.2 Accuracy Testing

To test the accuracy and reliability of the TWL prototype sensor, a comprehensive evaluation encompassing both workshop and on-site field testing was carried out. Initially, measurements were taken in workshop setting to minimise variability. Following this controlled phase, the sensor was deployed within the tunnel on site to ascertain its performance under real-world conditions. Throughout both stages, measurement data was recorded for the prototype and benchmarked against readings from a calibrated Kestrel 5400 meter, the standard on site testing instrument. This was to establish a baseline for comparison and accuracy verification.

A statistical evaluation of measurement data incorporating Mean Absolute Percentage Error (MAPE) and Pearson correlation techniques. The associated mathematical representations for these methods are:

$$MAPE_{var} = \frac{1}{n}\sum\left(\frac{|Actual - Measured|}{|Actual|}\right) \times 100\%$$

$$r = \frac{n\left(\sum xy\right) - (\sum x)(\sum y)}{\sqrt{\left[n\sum x^2 - (\sum x)^2\right]\left[n\sum y^2 - (\sum y)^2\right]}}$$

Where:

- n is the number of paired data points.
- x is the Prototype's values.
- y is the Kestrel meter's values.

Table 8 Shows the readings taken during workshop testing of the prototype and the Kestrel 5400 meter. Temperature and humidity were kept at atmospheric conditions and the wind speed varied in 0.5m/s – 2.0 m/s in 0.5 m/s increments (0.5, 1.0, 1.5, and 2.0m/s) using a hair dryer through a PVC conduit.

Table 8 Workshop testing in controlled environment - Prototype vs Kestrel 5400.

Prototype Temperature °C	Kestrel Temperature °C	Prototype Humidity %	Kestrel Humidity %	Prototype Wind Speed m/s	Kestrel Windspeed m/s	Prototype TWL	Kestrel TWL
26.0	26.1	29.5	29.6	0.5	0.6	369	377
26.0	26.1	29.6	29.6	0.6	0.6	377	377
26.0	26.1	29.4	29.6	0.6	0.5	369	369
26.0	26.1	29.3	29.6	0.4	0.4	357	357
26.0	26.1	29.3	29.6	0.6	0.5	377	369
26.0	26.1	29.2	29.6	1.0	1.0	383	383
26.1	26.1	29.2	29.6	1.2	0.9	381	378
26.1	26.1	29.3	29.6	1.1	1.1	382	381
26.1	26.1	29.3	29.6	0.9	0.9	383	384
26.2	26.1	30.8	29.7	1.0	1.0	383	383
26.2	26.1	29.8	29.7	1.5	1.5	373	367
26.2	26.2	29.6	29.7	1.4	1.5	378	368
26.1	26.2	29.7	29.7	1.4	1.5	378	368
26.1	26.2	29.6	29.7	1.5	1.5	373	368
26.1	26.2	29.8	29.7	1.5	1.6	373	364
26.1	26.2	30.0	29.8	1.9	1.9	358	354
26.1	26.3	30.1	29.8	1.8	2.0	358	352
26.1	26.3	30.1	29.8	1.8	2.0	358	352

26.1	26.3	30.1	29.8	1.9	2.1	358	349
26.1	26.3	30.4	29.8	1.9	2.0	358	352

Findings from workshop testing are recorded in Table 9 Statistical analysis summary of readings and outputs.

Table 9 Statistical analysis summary of readings and outputs

	Temperature	**Humidity**	**Wind Speed**	**Thermal Work Limit**
Mean – Prototype °C	26.1°C	29.7%	1.2 m/s	371
Mean – Kestrel °C	26.2°C	29.7%	1.3 m/s	368
MAPE	0.38%	0.34%	16.67%	2.21%
Correlation	0.08	0.78	0.99	0.92

The prototype's readings, when compared with the Kestrel meter's data, show promising on its accuracy for deployment in construction tunnel settings. MAPE values elucidate its precision, while the correlation coefficients solidify the prototype's alignment with established benchmarks. Future iterations must focus on further honing its precision, capitalising on insights from the correlation and accuracy analyses undertaken.

6.3 Redundancy Testing

Redundance testing was carried out to ascertain the resilience of the TWL sensor. These tests serve to simulate potential hardware failures and understand how the system reacts in such situations.

6.3.1 Simulation of BME280 Sensor Failure and System Response

When the BME280 sensor was disconnected to emulate a hardware failure, the following observations were noted:

1. The temperature and humidity output value were "*NaN*" both on the serial monitor and the cloud platform indicating that the system was unable to retrieve and process the required data from this sensor.
2. Wind speed values remained unaffected and maintained a constant reading suggesting wind speed measurements are isolated from the BME280's temperature and humidity readings and not resulting in complete system failure.
3. The TWL calculation also produce "NaN" on both the serial and cloud outputs, pointing to the critical dependency of the TWL measurement on the data from the BME280 sensor.

6.3.2 Simulation of Anemometer Failure and System Response

In a similar manner, the anemometer was intentionally disconnected to assess the system's reaction:

1. The temperature and humidity readings were not impacted by this failure. They remained constant and accurate, signifying that these metrics are independent of wind speed measurements.
2. The wind speed readings were directly affected, producing "NaN" displayed in the serial and cloud outputs.
3. As with the BME280 sensor failure, the TWL reading displayed "NaN" in both outputs, again emphasising the reliance of the TWL metric on precise readings from all its input sensors.

6.3.3 Actions from Outcomes

Backup procedures were incorporated into the coding following this sequence of test for improvement to device resilience. Data validity checks were incorporated for temperature, humidity, and wind speed readings. Before processing these values for TWL calculation, the system first verifies whether they fall within expected operational ranges. In the event of readings that are out of the expected range, error messaging was added. This coding is shown in lines 41 through 73 in the Project code listed in Appendix F. This not only assists in immediate fault detection but also expedites the troubleshooting process.

6.4 Reliability Testing

The reliability testing was carried out during second stage of testing. To test the reliability the prototype was subjected to continuous operation in simulated construction environment. Historic data from the cloud was downloaded and analysed and battery checks were carried out.

6.4.1 Testing Environment

The prototype was placed in a controlled garage environment for a continuous duration of 24 hours. This was done to emulate the conditions of a construction tunnel without the associated logistical challenges. To further enhance the simulation, a fan was installed to introduce airflow mimicking the ventilation systems in actual construction tunnels. This would test the sensor's capability to function accurately even with varying airflow conditions, which is a known variable in construction tunnels.

6.4.2 Data Analysis

The historical data from the cloud was downloaded daily for the analysis. The readings displayed minimal discrepancies, emphasising the potential robustness of the device. However, some issues were observed, notably gaps in the data where readings that should have been captured at 10-minute

intervals were missing. Out of an expected 144 readings for the 24-hour period (assuming a reading every 10 minutes), only 138 readings were successfully received. This indicates a data loss rate of approximately 4.17%. There are several potential reasons for these missing data points. One primary concern is the location of the device in relation to the Wi-Fi router. Given that the device relies on an internet connection for data transmission to the IoT cloud, any intermittent connectivity issues could lead to data loss. Additionally, potential data loss during transmission to the IoT cloud is another area that needs exploration.

Battery voltage was testing at beginning of the test showing 9.50V at the beginning of test and 9.25V showing a 0.25V drop over the course of the test. No noticeable or significant variations in readings were noted.

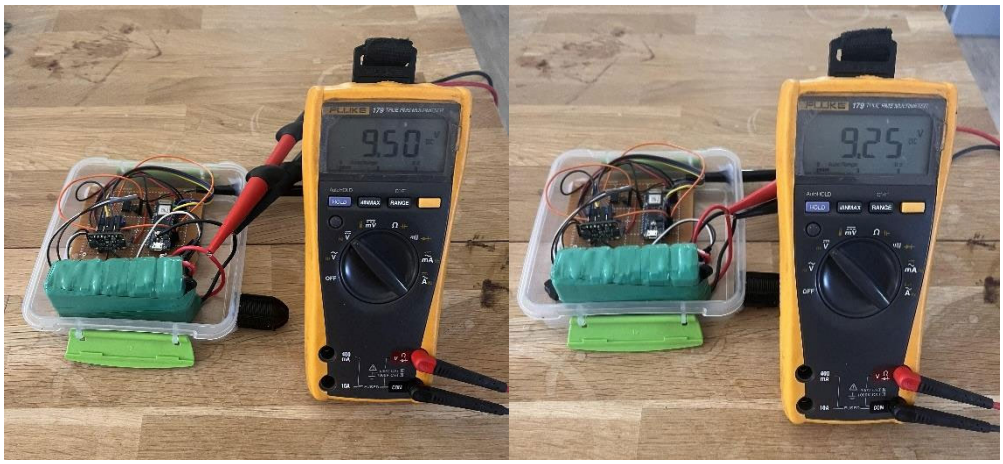

Figure 18 Battery voltages pre and post workshop test.

In conclusion, while the prototype showed promise in terms of data consistency, there remains room for improvement. Further testing and modifications might be required to optimise the device for real-world tunnel construction environments.

6.5 Failure Testing

Resilience testing it critical to determine the prototype's ability to handle failures efficiently. To evaluate the prototype's failure handling capabilities, failure testing was carried out in a controlled workshop environment. The sensor was exposed to abrupt changes in environmental conditions. Specifically, sudden spikes were introduced in temperature, humidity, and wind speed. These alterations were made sequentially and then in combinations to simulate the various challenges the device might encounter in real-world scenarios.

6.5.1 System's Response Time and Reliability

The sensor's response time was monitored during introduction of sudden spikes to of temperature, humidity, and wind speed. Delay time was reduced to monitor changes to system output and the serial monitor was used for monitoring measurement data. It should be noted that the measurement data is subject to processing and delay times. The time taken by the sensor to detect these changes, adjust its readings, and transmit this information was recorded. The millis() function was utilised to capture processing time for each iteration to monitor response times. On average, with no error warnings, an iteration took 179ms to produce all measurement outputs. The total time include 0.5 second delay was 679ms. The BME280 sensor had the slowest response time and longest settling time based on serial print output. Response time was 2-3 iterations (1.358 – 2.037s) and settling time was 5-6 iterations (3.395 – 4.047s). Noting that the data sheet for this sensor states a 1s response time. The FS7 had a response time of 1-2 iterations (0.659 – 1.358s) and settling time of 2-3 iterations (1.358 – 2.037s). Comparable to its datasheet, stating a response time of ~200ms. The reliability of these readings, in terms of accuracy and consistency, was also assessed against a Kestrel 5400 meter which was used for benchmarking.

6.5.2 Data Validity

A 5-point moving average data error check is included in the coding. This checks current values against the average of the 5 previous values. Error tolerances for temperature, humidity, and windspeed were set to 2.0, 5.0, and 0.5 respectively. These were increased during response checking in 6.5.1, however they were reset to check data validation checker during the same rapid changes. As designed, the system produced warning errors for irregular and invalid data in the serial monitor.

In conclusion, the failure testing provided valuable insights into the resilience of the TWL sensor prototype. While it showcased certain strengths, it also highlighted areas where improvements could be made, ensuring the sensor is thoroughly prepared for the demanding conditions of tunnel construction sites.

6.6 Testing Outcomes

A summary of the testing results are as follows:

- Measurements data was evaluated using MAPE and Pearson correlation techniques. Workshop testing showed the prototype and Kestrel 5400 had similar readings under controlled conditions.
- The prototype had an average temperature of 26.1°C, humidity of 29.7%, wind speed of 1.2 m/s, and thermal work limit of 371. The Kestrel 5400 meter displayed 26.2°C, 29.7%, 1.3 m/s,

and 368 respectively. Correlation values suggest the prototype aligns well with the Kestrel 5400 meter.

- Simulations of BME280 sensor and anemometer failures were done. System reactions to these failures were observed. After testing, backup procedures and data validity checks were incorporated into the coding to improve device resilience.
- The prototype was tested in a simulated construction environment for 24 hours. Analysis of cloud data indicated a data loss rate of 4.17%. Battery voltage showed a 0.25V drop over the test duration.
- The prototype was tested in a controlled workshop with sudden environmental changes. Response time and reliability during these changes were recorded. The BME280 sensor took 1.358-2.037s to respond, and the FS7 took 0.659-1.358s. Data validity checks were performed, and warning errors were observed for irregular data.

6.7 Conclusion

The prototype underwent various tests in both workshop and field conditions, benchmarked against the Kestrel 5400 meter. Redundancy tests highlighted dependencies and the need for backup coding procedures. While reliability tests showed minor data losses, failure tests identified response times and resilience areas for improvement. For optimal tunnel construction performance, further testing and refinements are required.

7 Implementation and Analysis

The final physical stage saw the implementation and subsequent analysis of the TWL sensor prototype. This section details the experiences and outcomes associated with deploying the developed prototype sensor in a real-world environment.

7.1 On-Site Deployment

Due to unforeseen program changes and works on site, the prototype deployment lasted only for a duration of 32 hours. This time frame was short, however, a complete set of data over a consistent period was obtained, thereby still allowing for a comprehensive analysis of how the prototype operates under actual tunnel conditions.

7.2 7.2 Data Collection

Two sets of data were retrieved over the 32-hour deployment period due to the subscription of the IoT cloud program. The data was then collated into a single excel worksheet. The data was easily accessed remotely via the Arduino Cloud platform, a key feature of the prototype. The full set of raw data can be found in Appendix G.

7.3 Device Performance

During its time on-site, the device displayed stability and resilience. It operated without any failures, indicating the reliability of the prototype in tunnel environments. The prototype’s operation was consistent with the outcomes observed during the testing phase. This alignment suggests that the laboratory tests effectively replicated the conditions and challenges the prototype would face in actual tunnel environments.

7.4 Data Integrity and Quality

One of the significant concerns in deploying new devices in real-world scenarios is the reliability and integrity of the data they produce. For this prototype, the retrieved data showcased a high level of quality and consistency. No data loss incidents occurred throughout the deployment duration. This outcome indicates a level of reliability of the device's recording capability and the robustness of the Arduino IoT cloud as a storage solution. Furthermore, the data quality was consistently high. There were no visible irregularities or inconsistencies in the data sets. The system's log also did not record any warnings, suggesting the seamless operation of the device throughout its deployment. Such indicators provide confidence in the device's capability to deliver reliable and accurate readings in tunnel environments.

7.5 Testing

The calibration process of the CTA sensor, carried out in a workshop and field tests, were executed using the Kestrel 5400 meter as a validation benchmark. Through a series of structured experiments and wind tunnel testing with controlled air velocities, calibration yielded successful results with an accuracy of less than 2% deviation from the Kestrel 5400 meter. This process allowed for the derivation of key constants (n and k), forming the basis for converting sensor voltages to real-time wind speeds used in the prototype's coding.

The prototype underwent accuracy and reliability testing in both controlled workshop environments and on-site field conditions. Initial tests in the workshop again benchmarked the prototype against the industry-standard Kestrel 5400 meter, revealing a high degree of correlation in most metrics, though with room for improvement. Redundancy tests were conducted to simulate hardware failures, emphasising the sensor's dependencies highlighting the need for backup procedures in its coding. Reliability tests indicated a promising yet imperfect data consistency, with minor data losses. Finally, failure tests subjected the prototype to sudden environmental changes, identifying its response times and resilience while revealing areas for potential enhancement. Overall, while the sensor exhibited promise, further refinement is necessary to fully optimise it for real-world applications.

Overall, the prototype displayed promising results in terms of accuracy and redundancy. However, there are areas of improvement in reliability and failure handling. Further testing and modifications may be needed for optimal performance in tunnel construction environments.

7.6 Modelling and Scenario Analysis

The testing phase was carried out during winter 2023. Most major civil activities had been completed, and the tunnel's permanent ventilation system was already installed and commissioned. However, for the purpose of the simulations, data from a typical summer day in March was utilised, ensuring that the prototype's performance was assessed during times with extreme conditions and higher variance. MATLAB was used to carry out all simulations and calculations for this section.

7.6.1 Weather Data and Modelling

Hourly weather data from Rozelle on 6th March 2023 (Weather Underground, 2023) served as the foundation data for modelling. The dataset, shown in Figure 19, provided accurate hourly data of the climatic conditions on the chosen day.

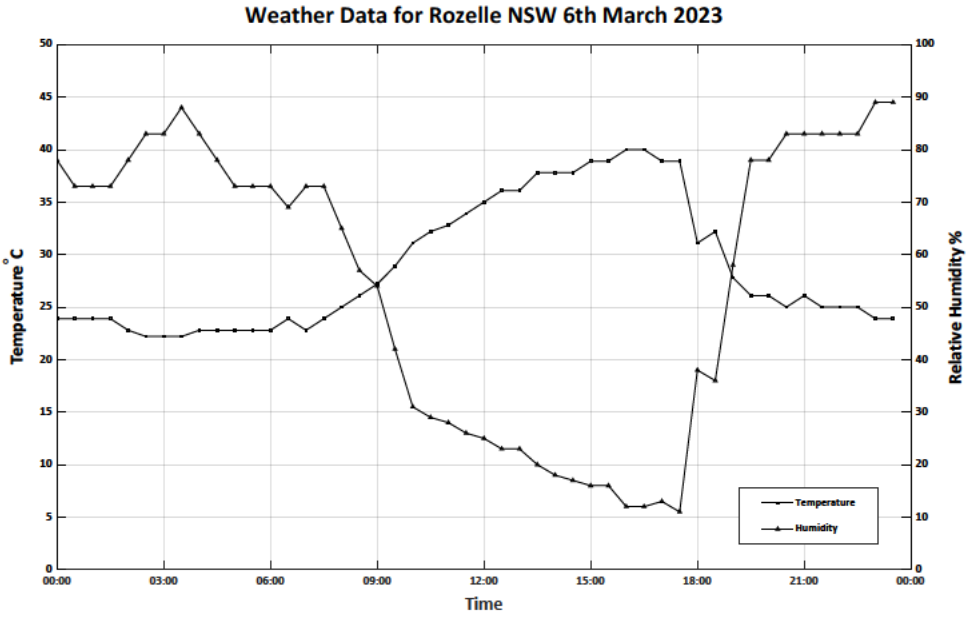

Figure 19 Hourly temperature and humidity data from Rozelle NSW used for simulations.

Using the dataset from Figure 19, and by applying a typical temperature ventilation windspeed of 0.3m/s, the theoretical and prototype TWL outputs were calculated. Figure 20 depicts the comparison of the theoretical and prototype's TWL index output, highlighting the accuracy of the prototype compared to Brake & Bate's calculation methodology.

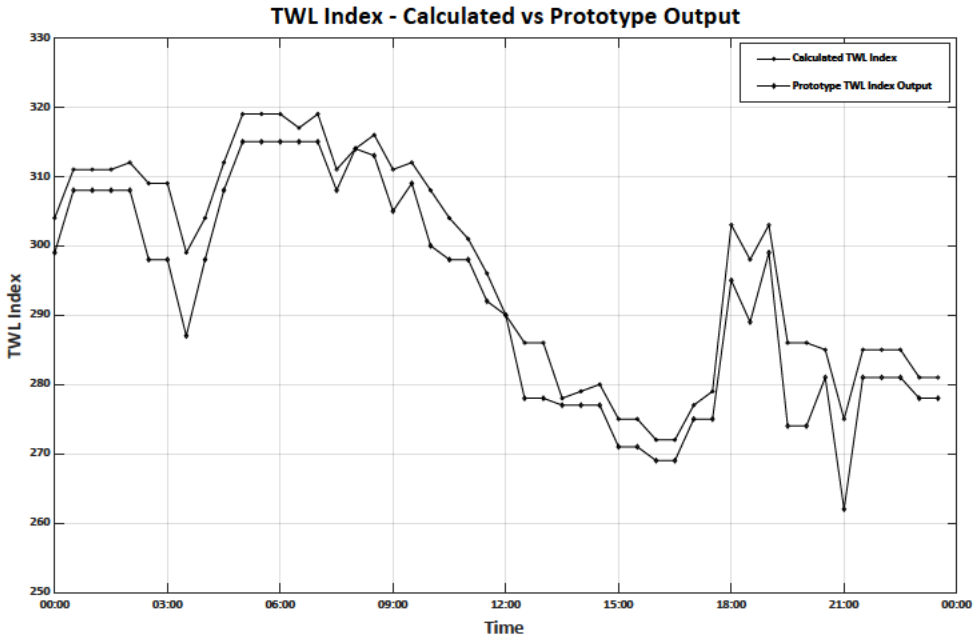

Figure 20 TWL Index output comparison – Theoretical vs Prototype

7.6.2 Correlation Analysis

To evaluate the level of similarity between the calculated and prototype TWL indices based on the data from Figure 19, a correlation matrix was constructed. This matrix, shown in Figure 21, yielded a Pearson's correlation coefficient of 0.9792, signifying a high degree of association between the data sets and therefore, a high level of accuracy of the prototype.

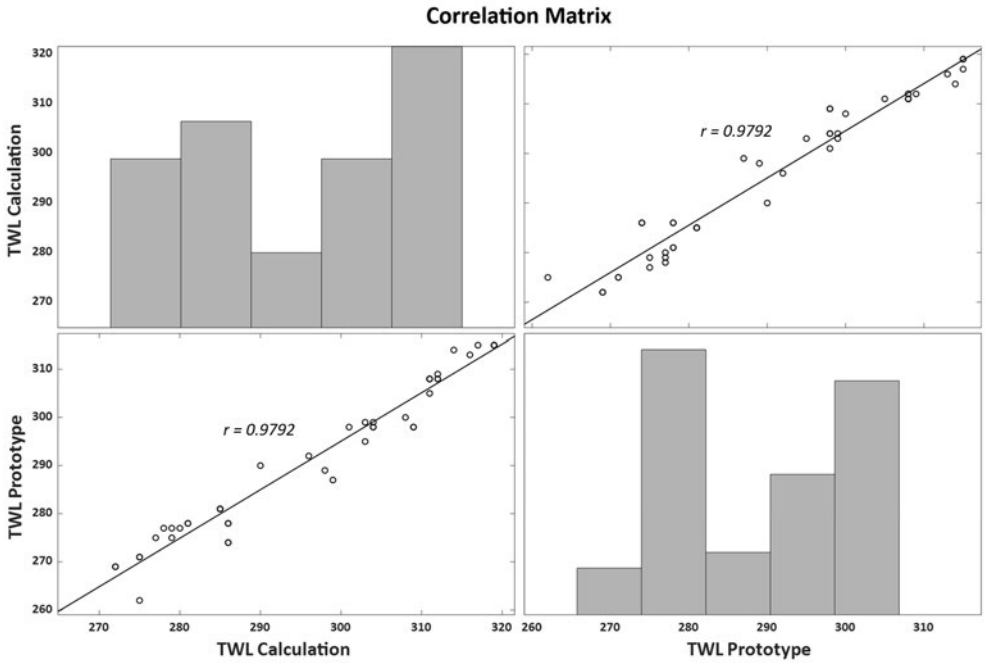

Figure 21 Correlation matrix – Theoretical vs Prototype TWL index output

7.6.3 Scenario Testing: Concrete Paving Pour

A specific construction activity was selected for the scenario testing, representing a concrete paving pour. This was introduced to study its impact on the tunnel environment and test variability performance during activities. This construction activity is known to rapidly influence the tunnel's microclimate.

The weather data for this scenario testing is presented in Figure 22.

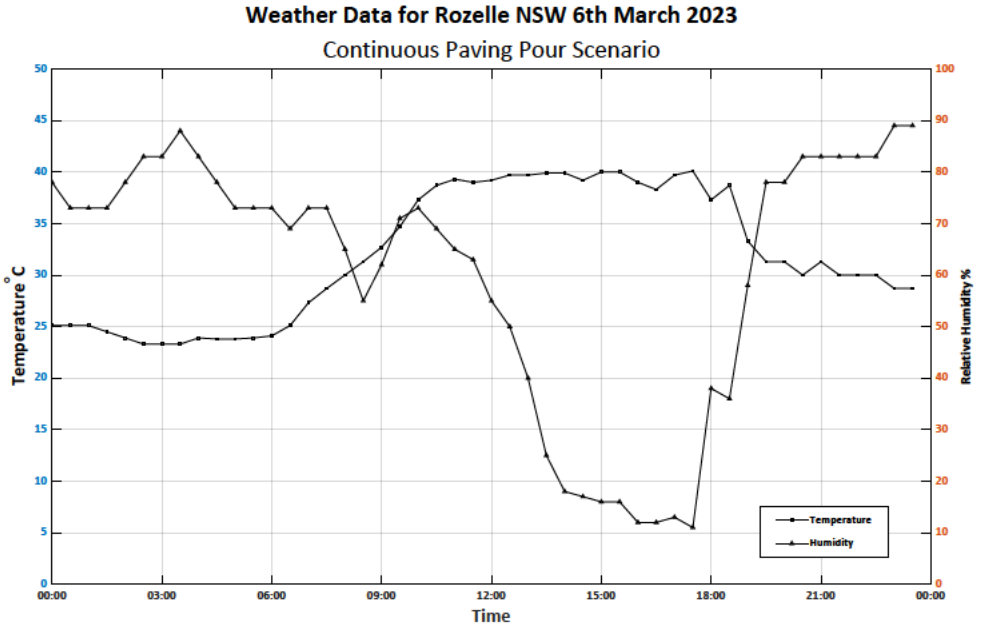

Figure 22 Adjusted hourly weather data for scenario testing

To simulate the thermal loading from the concrete paving pour, an average temperature loading of 1.1 was applied to the temperatures from the original data. This adjustment ensured that the temperatures never exceeded the maximum set point of 40°C. The time window for this scenario spanned from 8:00 AM to 10:30 AM, as indicated on Figure 23.

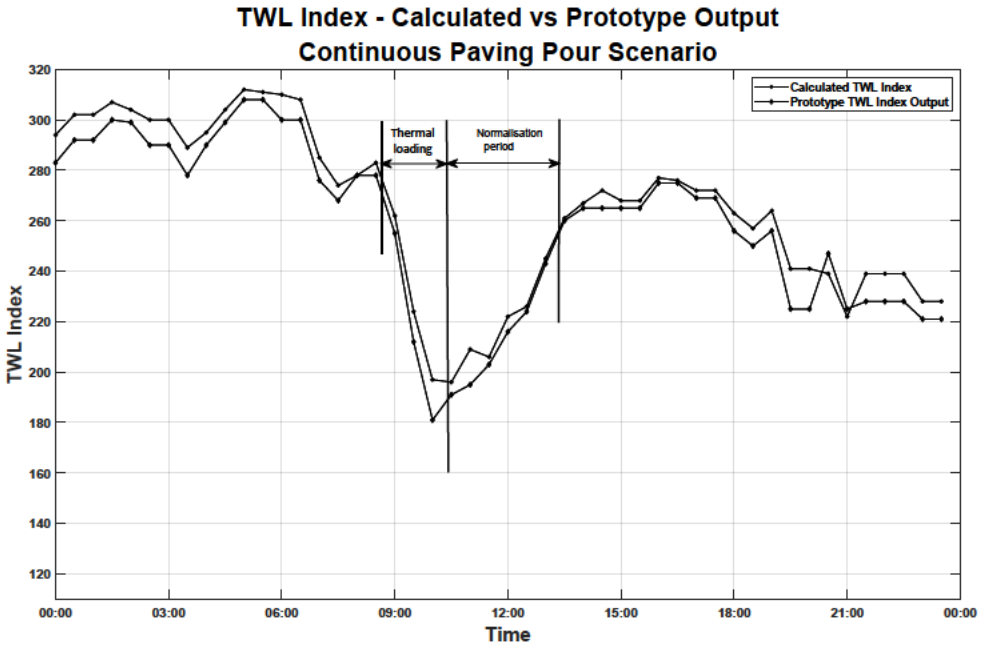

Figure 23 TWL index output comparison during scenario testing

Furthermore, considering the moisture release during the concrete curing process, an average loading of 1.4 was applied to the humidity values during the scenario activity. A normalisation period of approximately 3 hours is also applied allowing time for heat dissipation through the tunnel assuming a 0.3m/s windspeed and average flow path of 2.7km. It is important to note, temperature and humidity values for this scenario are estimations only.

7.6.4 Scenario Outcome

Following the implementation of the scenario data, the recalculated TWL index was assessed against the prototype's output. A subsequent correlation analysis for this scenario yielded a matrix presented in Figure 24. It was noted that even under these altered conditions, the prototype's performance was consistent with the calculated values with some improvement. The Pearson's correlation coefficient from this was 0.9937, supporting the close match between the calculated and prototype TWL index outputs.

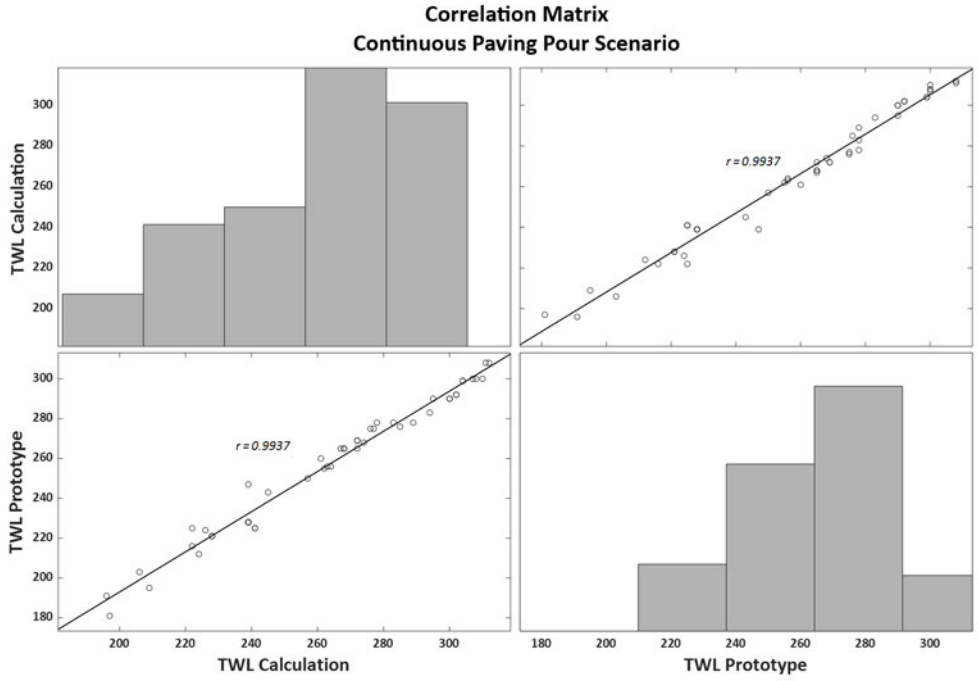

Figure 24 Correlation matrix for scenario testing – Theoretical vs Prototype TWL Index outputs

7.7 Effects of Wind Speed on TWL

Throughout testing and simulation stages, significant effects of wind speed were observed on the Thermal Work Limit (TWL). This section analyses these effects, underscoring the importance of choosing the appropriate anemometer for the prototype. TWL output from simulations were recorded and plotted to show these affects.

7.7.1 Wind Speed vs Humidity – TWL Relationship

As wind speed increases from 0.1 to 0.5, the slope for humidity and TWL becomes progressively more negative. This indicates that with increasing wind speeds in this range, the negative effect of humidity on TWL becomes more pronounced. From wind speeds 0.5 to 0.9, the slope becomes less negative, suggesting a diminishing effect of humidity on TWL.

7.7.2 Wind Speed vs Temperature – TWL Relationship

The average slope for temperature and TWL is consistently much more negative than the humidity-TWL relationship, suggesting that temperature has a stronger effect on TWL than humidity does across all wind speeds. From wind speeds 0.1 to 0.5, the average slope for temperature and TWL becomes more negative, showing a strengthening effect of temperature on TWL with increasing wind speeds.

After reaching its peak at a wind speed of 0.5, the slope becomes progressively less negative up to a wind speed of 0.9, indicating a weakening effect of temperature on TWL.

7.7.3 General Observations

The slopes for both relationships (humidity vs. TWL and temperature vs. TWL) are consistently negative across all wind speeds. This shows a clear negative correlation, meaning that as both temperature and humidity increase, the TWL decreases.

Even though both factors are negatively correlated with TWL, the magnitude of the slope for temperature vs. TWL is notably greater than that of humidity vs. TWL. This indicates that temperature has a stronger effect on TWL compared to humidity for the given wind speeds.

At lower windspeeds, the curve gradually but consistently rolls off indicating a greater effect of windspeeds <0.5m/s. This is shown in the mesh-grid plots 1 – 3 (top: 0.2 – 0.4m/s) in Figure 25 and Figure 26.

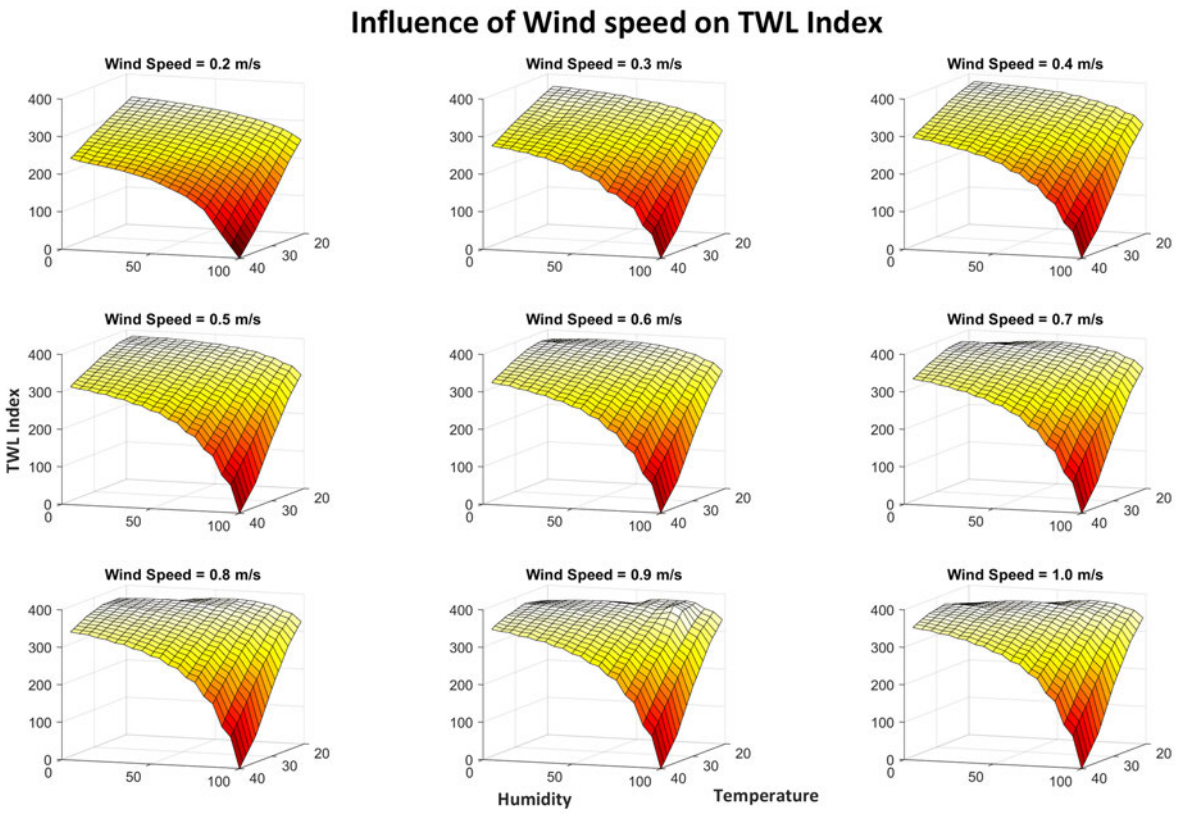

Figure 25 Windspeed effect on TWL output - 0.2 - 1.0m/s

Colour coding for the plots is as follows:

- White – TWL Index >300
- Yellow –TWL Index 200-300
- Orange – TWL Index 100-200
- Red – TWL Index 0-100

The top-right-hand quadrant of plots indicate the work environment approaching dangerous thermal conditions. See in Figure 26, it is evident during lower windspeeds, these levels are reaching this level much sooner showing minimal resistance to temperature and humidity. Alternatively, at higher windspeeds, temperature and humidity are resisted until temperatures >30° with humidity of 60% or greater. At this point the, roll off is considerable but TWL remains in the same zone above 200.

The anemometer selected and tested for the prototype achieved a 2% accuracy when compared to a calibrated Kestrel 5400 meter. A higher level of error, especially at low windspeeds and days with high temperature and humidity. The resolution of the prototype's anemometer was 0.01m/s where other sensors have ±0.1-0.2m/s not accounting for calibration error. To illustrate this, we could say that on a given day that is 38°C with humidity at 85%, and with a 0.2m/s error, the TWL output could read 173 (mid-range) with a 0.5m/s windspeed. Works can continue during this time with minimal control

measure, water and not working alone. If the true windspeed was 0.2m/s (allowing 0.05 error in the resolution), the true TWL output would be 116. This encroaches on the lower TWL index where recommended control measures are to leave the work front.

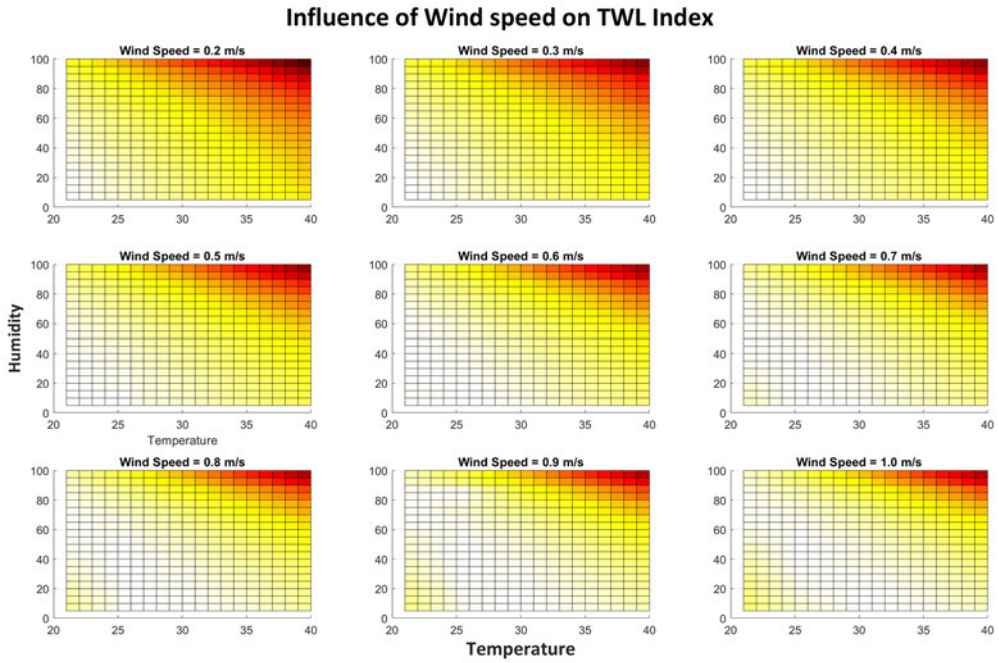

Figure 26 2D plot, Windspeed effect on TWL output - 0.2 - 1.0m/s.

In summary, both temperature and humidity have negative impacts on TWL, with temperature showing a stronger effect. Wind speed modulates these relationships, affecting the magnitude of the impact each factor has on TWL. This highlights the critical impacts tunnel ventilation can have on the work environment. From this exercise, a minimum airflow of 0.5m/s would be suggested for tunnel ventilation. This is in line with the current Tunnels Under Construction, Code of Practice NSW.

8 Conclusions

8.1 Literature

The literature review highlighted the importance of Thermal Work Limit (TWL) monitoring in tunnel environments because of health risks like heat stress. While various evaluation methods like predicted heat strain (PHS) and wet bulb globe temperature (WBGT) exist, TWL stands out for its precision. Most IoT sensor devices focus on environmental factors, with traditional TWL devices often being expensive and bulky. Hot-wire anemometry is vital for accurate TWL calculations. However, there are gaps in real-time TWL monitoring using portable IoT, system scalability, and the need for personalised solutions.

8.2 TWL Calculations

This dissertation thoroughly examines the works by Brake and Bates (2002) and provides a comprehensive outline of the calculation process for the TWL Index. The TWL calculation is the foundation of the prototype essential for providing accurate heat stress information and overall project success.

8.3 Optimisation of Sensor Positioning

The dissertation examined the optimisation of sensor positioning in a horseshoe-shaped construction tunnel. The unique tunnel design, combined with Mechanical and Electrical (M&E) equipment, created complex airflow patterns, making accurate measurement essential. To find the best location for the anemometer, a systematic grid-based analysis was conducted, capturing wind speeds at various points. The collected data underwent a detailed analysis to identify positions that closely matched average wind speed and showed minimal deviations. The optimal anemometer position was determined to be Row 5, Column 7, ensuring a reliable representation of tunnel ventilation dynamics.

8.4 Hardware Design

The hardware components selected for the Project prototype were chosen to ensure the device's optimal functionality and suitability for its specific purpose in tunnel environments. The decision to employ the Arduino Nano 33 IoT as the microcontroller, after evaluating ten potential options, reflected a clear focus on reliability and IoT compatibility. The integration of the Adafruit BME280 sensor provided accurate atmospheric readings and similarly, the adoption of the FS7 constant temperature anemometer, providing precise wind speed sensing capabilities. The components were housed securely within a protective housing to ensure the prototype was protected against external

environmental challenges. Collectively, the careful selection of these hardware components ensured that the Project prototype was not only robust but also perfectly tailored for its intended application.

8.5 Software Design

The software design for the TWL sensor prototype was examined detailing the programming and code intricacies essential for its operation. Libraries and dependencies were identified, primarily focusing on I2C communication for BME280 sensor interfacing, analogue interfacing for FS7 CTA sensor, and Arduino IoT Cloud connectivity. The system initialisation, continuous monitoring, and data acquisition processes were highlighted, emphasising data validation and the calculation of the TWL value. While the prototype's software demonstrated strength and reliability, specific areas for improvement, including enhanced calibration, error handling, and memory efficiency, were identified. The use of the Arduino IoT Cloud platform for the project enabled real-time data visualisation, via the IoT Cloud Dashboard.

8.6 Testing

The CTA sensor calibration used the Kestrel 5400 meter as a benchmark, resulting in under 2% deviation. The prototype underwent various tests in both workshop and field conditions. Redundancy tests highlighted dependencies and the need for backup coding procedures. While reliability tests showed minor data losses, failure tests identified response times and resilience areas for improvement. For optimal tunnel construction performance, further testing and refinements are required.

The on-site deployment of the prototype IoT Thermal Work Limit sensor in a tunnel environment has provided invaluable insights. Its flawless operation, combined with the high quality of data recorded, suggests that this device holds significant promise for future applications in similar settings. The subsequent chapters will delve deeper into the implications of these findings and chart the way forward for the potential scalability and commercialisation of this prototype.

8.7 Analysis

The modelling and scenario testing phase provided insights into the performance and reliability of the TWL sensor prototype. The high correlation coefficients in both the initial modelling and scenario testing demonstrate the prototype's capability to closely mirror theoretical calculations. Such results provide assurance in the prototype's utility and efficacy in real-world tunnel construction settings.

The research highlights the significant influence of wind speed on the TWL. Among the contributing factors, temperature demonstrates a more profound impact on TWL than humidity across varied wind

speeds. It's imperative to emphasise the precision in the anemometer, which was selected for the prototype, reiterating is accuracy of <2%. Furthermore, optimal tunnel ventilation, influenced by wind speed, emerges as crucial, with a minimum airflow recommendation of 0.5m/s. This aligns with the guidelines provided by the Tunnels Under Construction, Code of Practice NSW.

8.8 Project Cost

The total cost of the Project came to $225.36. This figure exceeded the budgeted estimate of $150.00 by $75.36, marking a 33% overspend. The cost could potentially decrease if sensors of a lesser quality were chosen for the project. A breakdown of the components and their respective costs is as per Table 10.

Table 10 Itemised Project costs

Part Description	**Cost**
Ardunio Nano 33 IoT Microcontroller	$45.95
Adafruit BME280 sensor	$28.95
FS7 CTA sensor	$42.00
PCB blank	$8.95
Components (resistors, transistor, opamp)	$18.72
Batteries	$34.95
Wiring accessories	$14.95
Housing	$4.99
Sundries	$11.95
Total Cost	$225.36

8.9 Future Works

In the development of the TWL prototype, several areas were found to show potential for future improvements and further exploration.

8.9.1 Battery Improvements

The current model utilises conventional batteries which were suitable for the prototype however they might not be the most sustainable or effective option for prolonged use. Future works could focus on:

- Integration of Lithium Batteries: Lithium batteries offer higher energy density, translating to longer battery life. Incorporating them could significantly extend the sensor's operational duration between battery replacements.

- Rechargeable Solutions: Implementing a rechargeable battery system would reduce the recurrent cost associated with battery replacements.

8.9.2 LoRaWAN Connectivity

While the current model operates effectively using WiFi protocol, changing communication protocol over to LoRaWAN could offer several advantages.

- Extended Range: LoRaWAN is known for its long-range capabilities, which would facilitate data transmission over larger distances, especially beneficial in extensive tunnel systems.
- Low Power Consumption: LoRaWAN's low power requirement aligns well with the aim of creating an energy-efficient device.
- Network Management: Network management becomes more streamlined allowing for better handling of multiple sensors when applied to a network of sensors.

8.9.3 Scalability

Scalability can be addressed in terms of both connectivity and networking. The following advancements could be made:

- Cloud integration with other air monitoring equipment: Integrating the sensor with existing air monitoring systems on the IoT cloud will provide a holistic view of the tunnel environment. This will enable real-time data sharing between devices, leading to more accurate and comprehensive safety assessments. The system could be designed to automatically pull data from various devices, thereby enhancing the overall efficiency and reliability of the monitoring process.
- Network capabilities between other devices and routers: To ensure uninterrupted data flow, the connectivity and data transmission between devices and network routers should be robust. Future works could explore:
    - Dynamic Routing: Implementing dynamic routing protocols to ensure data packets find the most efficient path between the sensor and the data collection centre.
    - Load Balancing: This would prevent any single router from being overwhelmed with traffic, ensuring smooth data transmission even during peak times.
    - Redundancy Measures: Introducing backup routers and pathways would ensure data transmission continuity, even in the event of a primary router failure.

8.9.4 Wearable TWL Device

The evolution of the sensor into a wearable format could ensure that safety management teams in tunnels have real-time data access. This could include:

- Ergonomic Design: The focus would be on creating a design that's comfortable for workers to wear during long hours, without hindering movement or causing a hazard.
- Real-time Alerts: There is potential to provide real-time alerts to workers and safety teams, ensuring immediate action during thermal limit breaches.
- Integration with Other Monitoring Systems: The wearable device could be designed to integrate with other existing tunnel air monitoring systems, providing a comprehensive safety solution.

References

Bernard, T.E, Ashley, C.D, & Kapanowski, D. (2022) Ability of Thermal Work Limit (TWL) to Assess Sustainable Heat Stress Exposures (2022), *Annals of Work Exposures and Health* 66, 1081–1085.

Ahmed, H., Bindekhain, J., Alshuweihi, M., Yunis, M. & Matar, N. (2020), 'Assessment of thermal exposure level among construction workers in UAE using WBGT, HSI and TWL indices', *Industrial Health* 58, 170–181.

Ali, M., Al-Azzawi, W., Jaber, M., Abd, S., Alkhayyat, A. & Rasool, Z. (2022), 'Improving coal mine safety with internet of things (IoT) based dynamic sensor information control system', *Physics and Chemistry of the Earth* 128(103225). doi:10.1016/j.pce.2022.103225.

Baker, R. (2000), Flow Measurement Handbook: Industrial Designs, *Operating Principles, Performance, and Applications*, Cambridge University Press.

Brake, D. (2002), The Deep Body Core Temperatures, Physical Fatigue and Fluid Status of Thermally Stressed Workers and the Development of Thermal Work Limit as an Index of Heat Stress, PhD thesis.

Brake, D. (2004), 'The application of a rational heat stress index (thermal work limit) to sports medicine', *https://www.mvaust.com.au/*. [Online; accessed May-2023].

Brake, D. & Bates, G. (2001), 'Fatigue in industrial workers under thermal stress on extended shift lengths', 51(7), 456–463. doi:10.1093/occmed/51.7.456.

Brake, D. & Bates, G. (2002a), 'Deep body core temperatures in industrial workers under thermal stress', 44(2), 125–135.

Brake, D. & Bates, G. (2002b), 'Limiting metabolic rate (thermal work limit) as an index of thermal stress', *Applied Occupational and Environmental Hygiene* 17(3), 176–186. doi:10.1080/104732202753438261.

Brake, D. & Bates, G. (2003), 'Fluid losses and hydration status of industrial workers under thermal stress working extended shifts', *Occupational and Environmental Medicine* 60(2). doi:10.1136/oem.60.2.90.

Brake, D. & T Nixon, T. (2008), Correctly estimating primary airflow requirements for underground metalliferous mines.

Brake, R. (2001), Proc. QLD mining industry occupational health and safety conference, in 'Fluid consumption, sweat rates and hydration status of thermally stressed underground miners and the implications for heat illness and shortened shifts', *Mine Ventilation Australia*. [Online; accessed May 2023].

Brake, R. & Bates, G. (2000), Proc. international conference on physiological and cognitive performance in extreme environments, in '*Occupational Heat Illness: An Interventional Study*', pp. 170–172. [Online; accessed May 2023].

Chan, A., Yi, W., Chan, D. & Wong, D. (2013), 'Using the Thermal Work Limit as an Environmental Determinant of Heat Stress for Construction Workers', *Journal of Management in Engineering* 29, 414–423.

CO2METER.COM (2023), 'Fixed vs portable gas detectors'. [Online; accessed May 2023].URL: *https://www.co2meter.com*

Dua, C., Lia, B., Lia, Y., Xua, M. & Yaoa, R. (2019), 'Modification of the predicted heat strain (phs)model in predicting human thermal responses for Chinese workers in hot environments', *Building and Environment* 165(106349). doi:10.1016/j.buildenv.2019.106349.

Fang, Z., Tang, T., Zheng, Z., Zhou, X., Liu, W. & Zhang, Y. (2021), 'Thermal responses of workers duringsummer: An outdoor investigation of construction sites in south china', Sustainable Cities and Society66(102705). doi:10.1016/j.scs.2020.102705.

Farshad, A., Montazer, S., Monazzam, M., Eyvazlou, M. & Mirkazemi, R. (2014), 'Heat stress level among construction workers', *Iranian Journal of Public Health* 43(4), 492–498.

Gariazzo, C., Taiano, L., Bonafede, M., Leva, A., Morabito, M., de' Donato, F. & Marinaccio, A.(2023), 'Association between extreme temperature exposure and occupational injuries among construction workers in Italy: An analysis of risk factors', *Environment International* 171(107677).doi:10.1016/j.envint.2022.107677.

Golbabaeia, F., Heidarib, H., Shamsipourc, A., Forushanid, A. & Gaeinie, A. (2019), 'A new outdoor environmental heat index (oehi) as a simple and applicable heat stress index for evaluation of outdoor workers', *Urban Climate* 29(100479). doi:10.1016/j.uclim.2019.100479.

Gun, R. (2019), 'Deaths in Australia from work-related heat stress, 2000 - 2015', *International Journal of Environmental Research and Public Health* 16(19).URL: https://www.mdpi.com/1660-4601/16/19/3601

Ioannou, L., Tsoutsoubi, L., Mantzios, K. & Flouris, A. (2019), 'A Free Software to Predict Heat Strain According to the iso 7933:2018', Industrial Health 57(6), 711–720.ISO (2018), Ergonomics of the thermal environment – Analytical determination and interpretation of heat stress using calculation of the predicted heat strain, Standard ISO 7933:2004, *International Organisation for Standardisation.*

Karen, A. & Myer, L. (2020), https://tunnelingworld.com/. [Online; accessed May-2023].

LaNasa, P. J. & Upp, E. L. (2014), 3 - types of fluid flow measurement, in Fluid Flow Measurement (Third Edition)', Butterworth-Heinemann, Oxford, pp. 31–44. URL: https://www.sciencedirect.com/science/article/pii/B9780124095243000034

Li, J., Wu, L. & Chen, H. (2023), 'Analysis of thermal comfort and threshold range of air supply parametersfor diferent types of work in humid-heat coal mines', *Case Studies in Thermal Engineering* 44(102826).doi:10.1016/j.cite.2023.102826.

Ligrani, P., Mahmood, G., Harrison, J., Clayton, C. & Nelson, D. (2001), 'Flow structure and local Nusselt number variations in a channel with dimples and protrusions on opposite walls', International *Journal of Heat and Mass Transfer* 44(23), 4413–4425. URL: https://www.sciencedirect.com/science/article/pii/S0017931001001016

Meng, J., Tabosa, E., Xie, W., Runge, K., Bradshaw, D. & Manlapig, E. (2016), 'A review of turbulence measurement techniques for flotation', *Minerals Engineering* 95, 79–95.URL: https://www.sciencedirect.com/science/article/pii/S0892687516301583

Merzkirch, W., Vitkin, D. & Xiong, W. (1998), 'Quantitative fow visualization', Meccanica 33, 503–516.Miller, V. & Bates, G. (2002), 'Empirical validation of a new heat stress index', *Journal of Occupational Health and Safety Australian and New Zealand* 18(6), 145–153. doi:10.1093/annhyg/mem035.

Miller, V. & Bates, G. (2007), 'The thermal work limit is a simple reliable heat index for the protec-tion of workers in thermally stressful environments', *Annals of Occupational Hygiene* 51(6), 553–561.doi:10.1093/annhyg/mem035.

Montazer, S., Farshad, A., Monazzam, M., Eyvazlou, M., Yaraghi, A. & Mirkazemi, R. (2013), 'Assessment of construction workers' hydration status using urine specific gravity', *International Journal of Occupational Medicine and Environmental Health* 26, 762–769.Ng, K. (2014), 'Feeling the heat'. [Online; accessed May 2023].URL: https://www.amsj.com.au/feeling-heat/

Roghanchi, P. & Kocsis, K. (2018), 'Challenges in selecting an appropriate heat stress index to protect workers in hot and humid underground mines', *Safety and Health at Work* 9, 10–16.doi:10.1016/j.shaw.2017.04.002.

Saidi, A. & Gauvin, C. (2023), 'Towards real-time thermal stress prediction systems for workers', 113(103405).

Saini, T., Rana, D., Attri, S., Chaturvedi, P. & Dutt, V. (2022), Forecasting of Air Pollution via a Low-Cost IoT-Based Monitoring System, *Springer Nature*, pp. 25–35. Doi: 10.1007/978-3-030-73885-3.

Sajad Zarea, S., Shirvanb, H., Hemmatjoc, R., Nadrid, F., Jahanie, Y., Jamshidzadehf, K. & Pay-darf, P. (2019), 'A comparison of the correlation between heat stress indices (utci, wbgt, wbdt,tsi) and

physiological parameters of workers in Iran', *Weather and Climate Extremes* 26(100213).doi:10.1016/j.wace.2019.100213.

Shakerian, S., Habibnezhad, M., Ojha, A., Lee, G., Liu, Y., Jebelli, H. & Lee, S. (2021), 'Assessing occupational risk of heat stress at construction: A worker-centric wearable sensor-based approach', *Safety Science* 142(105395). Doi:/10.1016/j.ssci.2021.105395.

Shekhter, Y. (2011), 'Hot-wire and hot-film anemometers'. [Online; accessed June 2023].URL: https://www.thermopedia.com

Sua, Y., Tiana, M., Li, J., Zhanga, X. & Zhaoa, P. (2022), 'Numerical study of heat and moisture transfer in thermal protective clothing against a coupled thermal hazardous environment', *International Journal of Heat and Mass Transfer* 194(122989). doi:10.1016/j.ijheatmasstransfer.2022.122989.

Sydney, New South Wales, Australia Weather History 2023 *Weather Underground*. Available at: https://www.wunderground.com/ [Online; accessed 10 October 2023).

Tavoularis, S. (2005), Measurement in Fluid Mechanics, Cambridge University Press. [Online; accessed June2023].

Ueno, S. (2020), 'Comparison of correction factor for both dynamic total thermal insulation and evaporative resistance between iso 7933 and iso 9920', *Journal of Physical Anthropology* 39(23). doi:10.1186/s40101-020-00235-9.

Yang, B., Yao, H., Yang, P., Guo, Y., Wang, F., Yang, C., Li, A. & Che, L. (2022), 'Effects of thermal and acoustic environments on workers' psychological and physiological stress in deep underground spaces', *Building and Environment* 212(108830). doi:10.1016/j.buildenv.2022.108830.

Yunpeng, H., Mingnian, W., Qiling, W., Dagang, L. & Jianjun, T. (2019), 'Field test of thermal environment and thermal adaptation of workers in high geothermal tunnel', *Building and Environment* 160(106174). doi:10.1016/j.buildenv.2019.106174.

Zhou, P., Feng, Y., Zhou, F., Wei, Z., Gou, S., Xu, H. & Wang, Z. (2023), 'Evaluation system of worker comfort for high geothermal tunnel during construction: A case study on the highway tunnel with the highest temperature in China', *Tunnelling and Underground Space Technology* 135(105028). doi:10.1016/j.tust.2023.105028.

Zijun Li, Z., Wang, J., Xu, Y., Li, G., Yuan, T. & Zhang, M. (2022), 'Heat hazard control in excavation engineering: Numerical simulation of heat transfer characteristics of high temperature tunnel with movable thermal insulation layer', *Thermal Science and Engineering Progress* 32(101393). doi:10.1016/j.tsep.2022.101393.

Appendix A Project Specification

ENG4111/4112 Research Project

Project Specification

For: Chism Long

Title: Development of a low cost IoT device to accurately measure thermal work conditions for workers in tunnelling environments.

Major: Electrical and Electronic Engineering

Supervisors: Habib Alehossein & Tobias Low

Enrollment: ENG4111 – EXT S1, 2023

ENG4112 – EXT S2, 2023

Project Aim: To design and develop a new low-cost IoT air monitoring device equipped and linked to appropriate sensors and software codes which can provide accurate Thermal Work Limit Data and readings to monitor air quality and safety of people working in underground construction tunnels.

Research Gap: An IoT device which monitors Thermal Work Limit in tunneling environments has not yet been developed. This Project will cover the development, testing and implementation of said device.

Programme: Version 3, 31st March 2023

1. Liaise with Joint Venture Project teams for Research Project onsite approval and air monitoring testing requirements.
2. Research existing IoT devices used in tunneling and mining.
3. Research Thermal Work Limit impacts, conditions and requirements.
4. Research aerodynamic specifications and determine impacts, limitations and considerations for measurement and sensor locations.
5. Research and evaluate available hardware, equipment, and materials including microcontrollers and sensors.
6. Review and evaluate available IoT cloud platforms, web-based and application software for IoT devices.

7. Design IoT device with selected hardware and sensors to suit tunnel environments.
8. Test and analyze accuracy of sensors including calibration methodology for tunnel environments.
9. Develop coding for prototype including debugging and simulations.
10. Build prototype and calibration of sensors locally.
11. Test device operation and analyze results for accuracy and reliability.
12. Set up IoT cloud platform including and carry out testing between device and cloud. Set up dashboards or interface for user friendly environment.
13. Install device at selected location on site in the tunnel. Determine affects on sensor readings/data in relation to positioning of device.
14. Run and monitor data from selected platform. Discuss site readings and compare with device readings. Review issues, implications and possible improvements with site team

If time and resource permit:

15. Review energy consumption of device and investigate possible improvements for hardware/software.
16. Approach project team for implementation on other projects.

Appendix B Project timeline

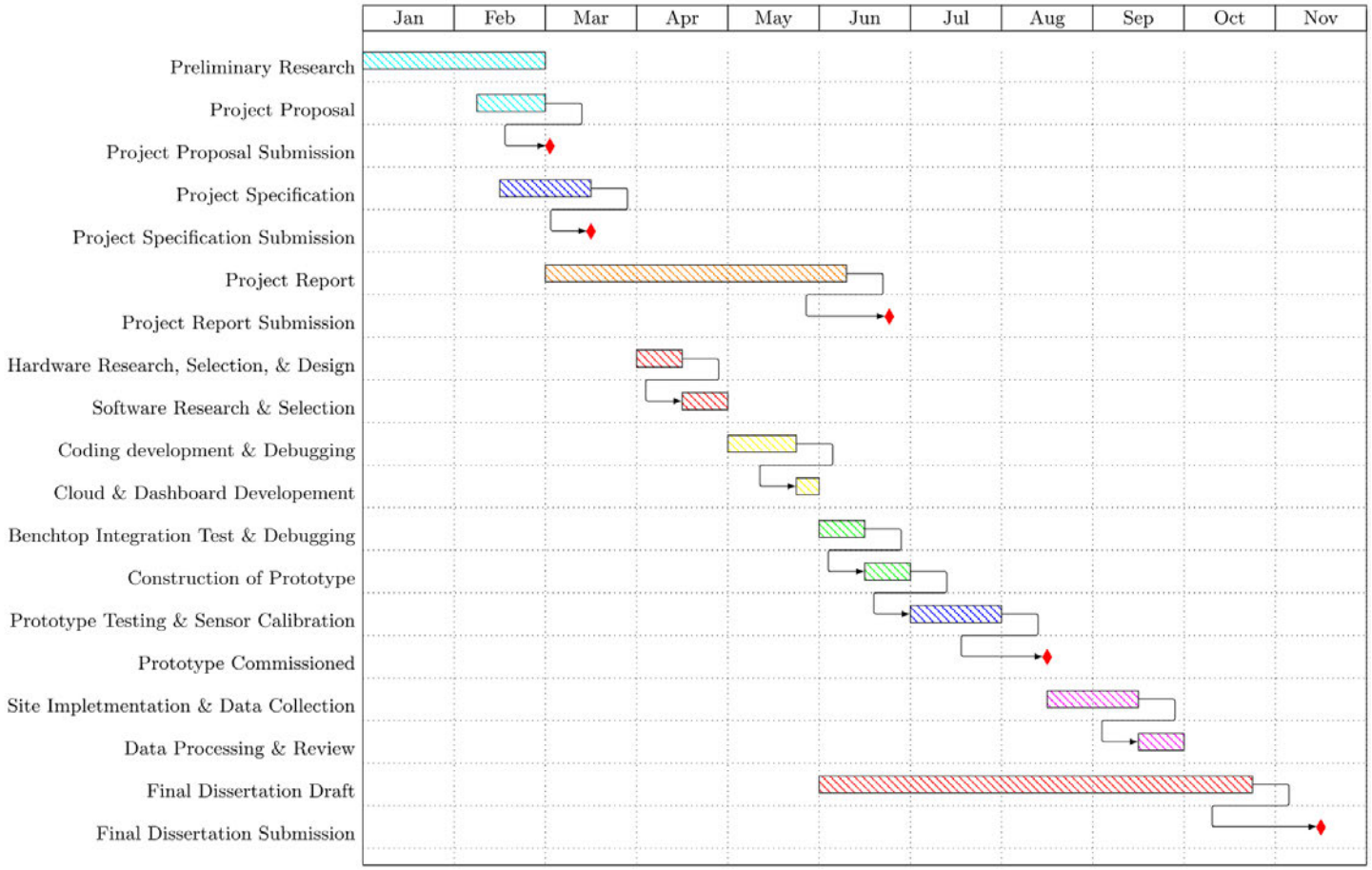

Appendix C Project Risk Assessment

Steps	Activity / Task	Hazard	Risk	Risk Ranking	Control Measures	Residual Risk	Who is Responsible
1	Design IoT TWL Sensor	Poor design of device Malfunctioning device Incorrect hardware	Device malfunction or fire Device failure Project incompletion Incorrect data for system	4B	Assessment of all hardware for suitability and compatibility	2D	Chism Long
2	Code program for sensor	Poor coding Insufficient coding sequence	Device failure Project incompletion Incorrect data for system Safety teams provided wrong information	4B	Fail safe coding Include cross and error checking in coding Simulation testing to be carried out prior to build	2D	Chism Long
3	Build prototype	Using hand tools Using soldering iron Poor construction of device	Cuts, burns, abrasions Faulty device Rework to repair device	3C	Use correct gloves for task Use correct tools for task Ensure ares is well ventilated	1E	Chism Long
4	Testing and calibration of sensor	Incorrect calibration Insufficient testing	Incorrect data for system Safety teams provided wrong information Wrong alerts sent to safety team Site delays from false alarms Loss of time and money	4B	Calibrate with known device Try range of testing for each device separately and integrated Recheck regulary prior to deployment to check for calibration drift	2D	Chism Long
5	Work in commissioning zone	Live equipment Changing conditions of equipment	Electroculation Struck by moving equipment Personnel injury	4C	Commissioning zone permit required Commissioning zone training required Treat all equipment as live	2E	Chism Long, spotter
6	Use EWP	Working at height Plant / personnel interaction Overhead obstructions Poorly maintained EWP	Fall from height Personnel injury Drop object from height Machine failure Personnel crushed	4B	Only ticketed and VOC'ed personnel to Operate EWP. Spotter to be in place for each Work area. Spotter to guide traffic and personnel around the Barricaded EWP work area. Spotter to be trained in operation of ground controls to be able to lower the EWP in the event of emergency	3D	Chism Long
7	Install sensor	Incorrect mounting of device Incorrect handling of device Poor lighting Other crews working in area	Device drop from tunnel crown Personnel injury Other dropped objects - fixings and fasteners	4B	Use correct handling techniques Provide drop zone Use additional lighting where required Ensure device is mounted securely before leaving work area Use spotter to control pedestrian access	2D	Chism Long
8	Monitor readings and analyse data	Misread readings Faulty data	Wrong alerts sent to safety team Site delays from false alarms Loss of time and money Poor findings for report Unsuccessful report	3B	Cross check readings with site measured readings Use Kestrell Meter onsite for continual poor reading Recalibrate sensors Identify outlier readings Notify safety team of any irregular readings	1E	Chism Long
9	Remove sensor	Incorrect handling of device Poor lighting	Device drop from tunnel crown Personnel injury Other dropped objects - fixings and fasteners	4B	Use correct handling techniques Provide drop zone Use additional lighting where required Ensure all equipment and fasteners are removed before leaving work area	2D	Chism Long

Appendix D Anemometer Circuit

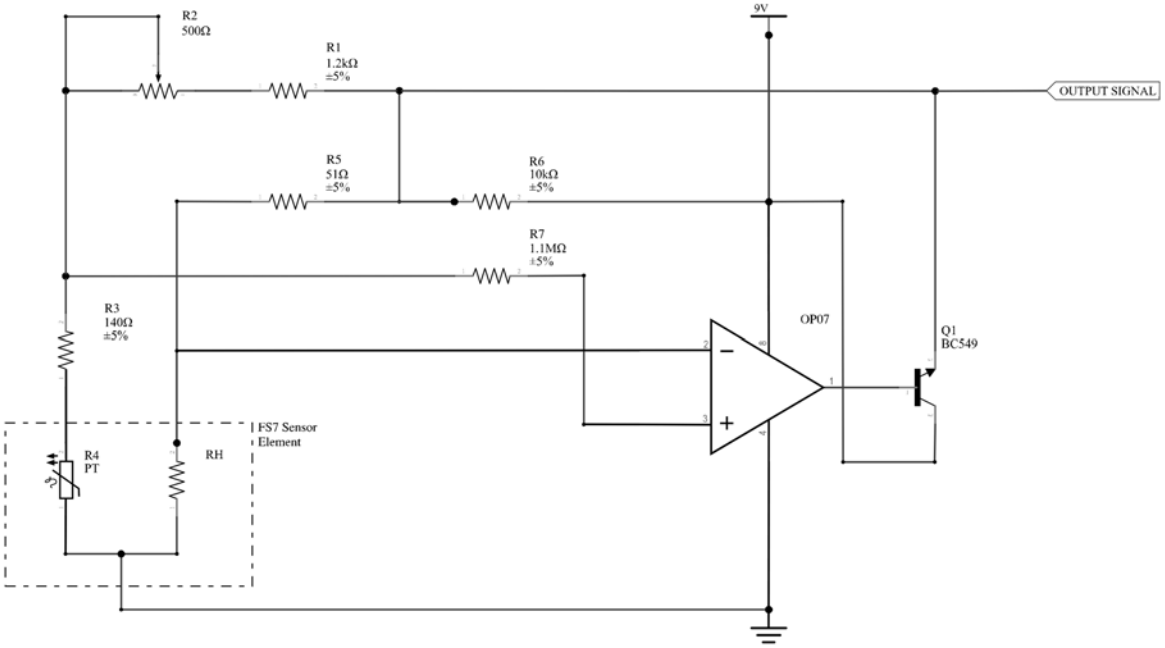

Appendix E System Circuit

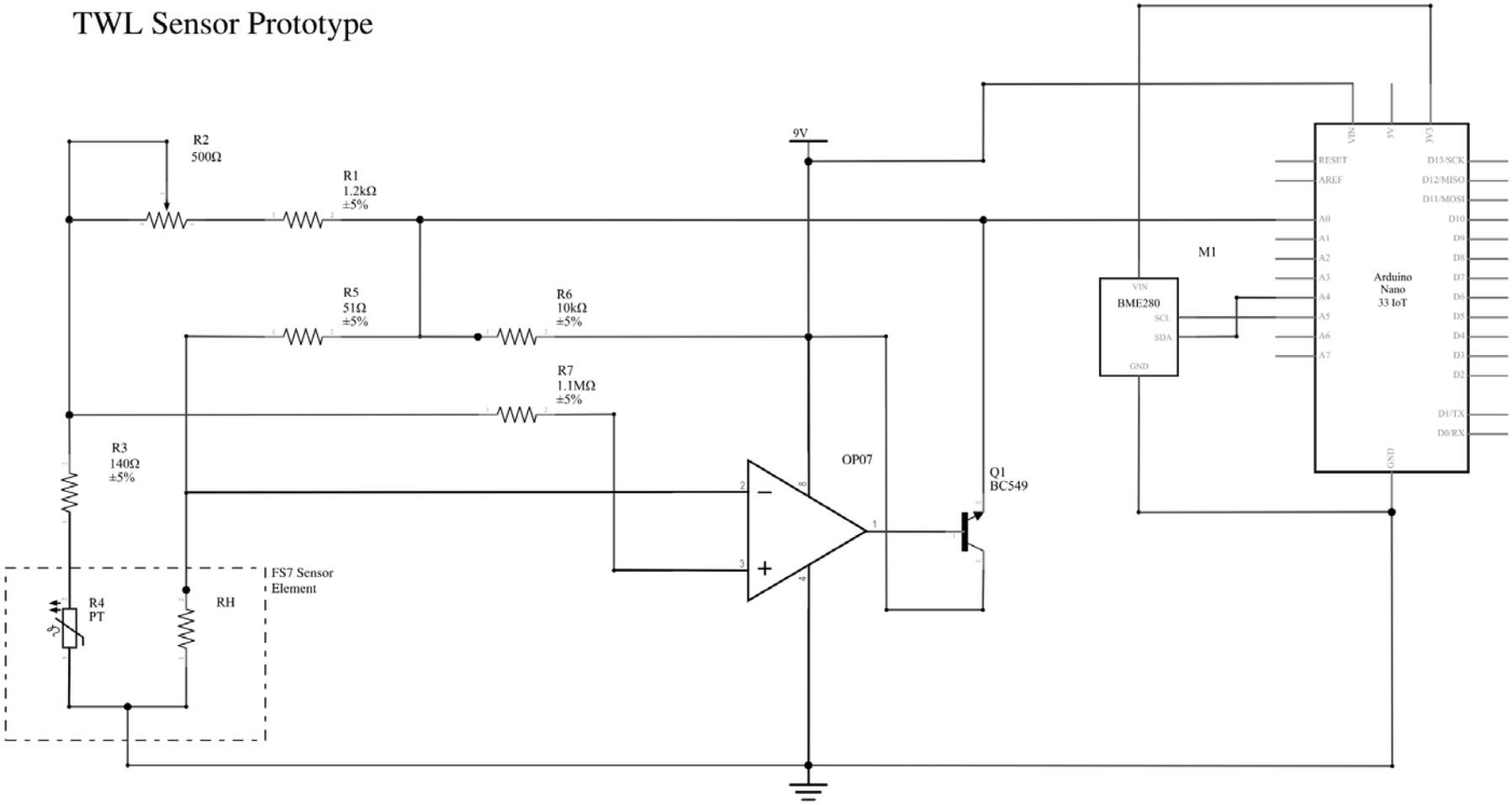

Appendix F Project Coding

```
#include <Wire.h>
#include <Adafruit_Sensor.h>
#include <Adafruit_BME280.h>
#include <thingProperties.h>
#include <TWLOutput.h>

// Create instance for BME280
Adafruit_BME280 bme;

// Offset values for calibration
float temperatureOffset = 0.1;
float humidityOffset = 0.0;

// CTA calibration characteristics
float V_0 = 3.20;   // Volts - signal voltage at zero wind speed
float k = 0.58641;  // unitless - fluidic constant
float n = 0.5;      // unitless - ratio relative to windspeed

// error checking characteristics
const int NUM_READINGS = 5;
float temperatureReadings[NUM_READINGS];  // the readings from the analog input
float humidityReadings[NUM_READINGS];
float windSpeedReadings[NUM_READINGS];
int readIndex = 0;  // the index of the current reading

void setup() {
 Serial.begin(9600);

 if (!bme.begin(0x76)) {
  Serial.println("Could not find a valid BME280 sensor, check wiring!");
  while (1);
 }

 // Initialise all readings to 0
 for (int i = 0; i < NUM_READINGS; i++) {
  temperatureReadings[i] = 0;
  humidityReadings[i] = 0;
  windSpeedReadings[i] = 0;
 }

 // Connect to Arduino IoT Cloud and check error messages
 initProperties();
 ArduinoCloud.begin(ArduinoIoTPreferredConnection);
 setDebugMessageLevel(2);
 ArduinoCloud.printDebugInfo();
}

void loop() {
```

```
  ArduinoCloud.update();

  float temperature = bme.readTemperature() + temperatureOffset;
  float humidity = bme.readHumidity() + humidityOffset;
  float windSpeed = VoltageToWindSpeed(analogRead(A0));

  bool isTemperatureValid = temperature >= 21.0 && temperature <= 40.0;
  bool isHumidityValid = humidity >= 5.0 && humidity <= 100.0;
  bool isWindSpeedValid = windSpeed >= 0.0 && windSpeed <= 1.0;

  if (!isTemperatureValid) Serial.println("Warning: Temperature out of range!");
  if (!isHumidityValid) Serial.println("Warning: Humidity out of range!");
  if (!isWindSpeedValid) Serial.println("Warning: WindSpeed out of range!");

  if(isTemperatureValid && isHumidityValid && isWindSpeedValid) {
     float TWL = getTWLValue(windSpeed, temperature, humidity);

     // Save the readings in the array
     temperatureReadings[readIndex] = temperature;
     humidityReadings[readIndex] = humidity;
     windSpeedReadings[readIndex] = windSpeed;
     readIndex = (readIndex + 1) % NUM_READINGS;  // advance to the next position in the array

     // Calculate the averages
     float avgTemperature = calculateAverage(temperatureReadings, NUM_READINGS);
     float avgHumidity = calculateAverage(humidityReadings, NUM_READINGS);
     float avgWindSpeed = calculateAverage(windSpeedReadings, NUM_READINGS);

     // Check against the averages
     if (abs(temperature - avgTemperature) < 2.0 && abs(humidity - avgHumidity) < 5.0 &&
abs(windSpeed - avgWindSpeed) < 1.0) {
       // Update cloud properties
       cloudTemperature = temperature;
       cloudHumidity = humidity;
       cloudWindSpeed = windSpeed;
       cloudTWL = TWL;
       // print readings
       Serial.print("Temperature: ");
       Serial.print(temperature);
       Serial.println(" °C");
       Serial.print("Humidity: ");
       Serial.print(humidity);
       Serial.println(" %");
       Serial.print("Wind Speed: ");
       Serial.print(windSpeed);
       Serial.println(" m/s");
     } else {
       Serial.println("Warning: Irregular variance in readings!");
     }
   } else {
     Serial.println("Warning: Invalid data detected!");
```

```
    }

  delay(5000);  // delay timer
}

float calculateAverage(float* readings, int numReadings) {
  float sum = 0;
  for (int i = 0; i < numReadings; i++) {
    sum += readings[i];
  }
  return sum / numReadings;
}

float VoltageToWindSpeed(int analogValue) {
  float voltage = analogValue * (5.0 / 1023.0);
  if (voltage < 3.2) return 0.0;
  return pow((voltage - V_0) * (voltage + V_0), 1/n) / (pow(k, 1/n) * pow(V_0, 2/n));
}

int getWindSpeedIndex(float windSpeed) {
  return max(1, min(10, (int)(windSpeed * 10)));
}

int getTemperatureIndex(float temperature) {
  return max(1, min(20, (int)ceil(temperature) - 20 + 1));
}

int getHumidityIndex(float humidity) {
  return max(1, min(20, (int)ceil(humidity / 5.0)));
}

float getTWLValue(float windSpeed, float temperature, float humidity) {
  int matrix = getWindSpeedIndex(windSpeed) - 1;
  int row = getTemperatureIndex(temperature) - 1;
  int column = getHumidityIndex(humidity) - 1;

  return TWLData[matrix][row][column];
}
```

Appendix G Measurement Data Tables

time	temperature	humidity	windspeed	twl
2023-09-16T23:47:59.508Z	25.09	31.38	0.66	379
2023-09-16T23:52:56.87Z	25.23	30.87	0.84	381
2023-09-16T23:57:54.139Z	25.41	30.41	0.64	379
2023-09-17T00:02:51.409Z	26.03	29.65	0.79	379
2023-09-17T00:07:48.676Z	25.72	30.54	0.73	382
2023-09-17T00:12:45.945Z	25.84	29.94	0.8	382
2023-09-17T00:17:43.315Z	25.92	29.87	0.79	382
2023-09-17T00:22:40.585Z	26.15	29.45	0.84	381
2023-09-17T00:27:37.755Z	26.32	29.15	0.58	372
2023-09-17T00:32:35.533Z	26.69	30.1	0.87	379
2023-09-17T00:39:45.834Z	27.61	26.88	0.79	376
2023-09-17T00:44:50.167Z	26.55	28.75	0.71	379
2023-09-17T00:49:54.502Z	26.51	29.58	0.72	379
2023-09-17T00:54:58.836Z	26.98	28.53	0.55	372
2023-09-17T00:59:56.924Z	27.49	27.19	0.59	368
2023-09-17T01:05:31.561Z	27.59	28.23	0.57	368
2023-09-17T01:10:29.644Z	27.78	25.51	0.69	375
2023-09-17T02:15:42.687Z	28.25	26.52	0.66	372
2023-09-17T02:20:39.956Z	28.26	26.4	0.55	364
2023-09-17T02:26:33.842Z	28.4	25.48	0.77	373
2023-09-17T02:34:24.373Z	27.03	26.06	0.83	380
2023-09-17T02:39:28.708Z	26.45	26.86	0.54	372
2023-09-17T02:44:33.144Z	26.38	27.33	0.7	379
2023-09-17T02:49:37.476Z	27.89	26.57	0.84	380
2023-09-17T02:54:41.812Z	28.33	26.26	0.57	364
2023-09-17T02:59:45.941Z	28.38	26	0.68	372
2023-09-17T03:04:50.172Z	28.51	26.26	0.51	364
2023-09-17T03:09:54.304Z	28.66	25.87	0.56	364
2023-09-17T03:14:58.33Z	28.65	25.46	0.8	379
2023-09-17T03:20:02.461Z	28.65	25.27	0.72	373
2023-09-17T03:25:06.487Z	28.69	25.6	0.81	379
2023-09-17T03:30:10.616Z	28.67	25.67	0.63	372
2023-09-17T03:35:12.698Z	28.81	25.72	0.89	379
2023-09-17T03:40:09.966Z	28.86	25.51	0.67	372
2023-09-17T03:45:07.235Z	28.98	25.46	0.8	379
2023-09-17T03:50:04.405Z	29.14	25.57	0.65	367
2023-09-17T03:55:01.569Z	29.24	24.9	0.55	365
2023-09-17T03:59:58.838Z	29.21	24.9	0.63	372
2023-09-17T04:04:56.004Z	28.98	26.99	0.78	373
2023-09-17T04:09:53.273Z	29.06	26.32	0.69	367
2023-09-17T04:14:50.442Z	29.14	27.41	0.8	372

2023-09-17T04:19:47.711Z	29.14	26.91	0.77	372
2023-09-17T04:24:44.885Z	28.71	25.61	0.82	379
2023-09-17T04:29:42.147Z	28.06	23.96	0.86	378
2023-09-17T04:34:39.523Z	27.77	24.85	0.82	379
2023-09-17T04:39:36.889Z	27.71	25.77	0.57	368
2023-09-17T04:44:34.26Z	27.73	26.03	0.67	375
2023-09-17T04:49:31.628Z	27.71	26.26	0.52	368
2023-09-17T04:54:29.104Z	27.79	26.84	0.76	376
2023-09-17T04:59:26.475Z	27.82	26.44	0.66	375
2023-09-17T05:04:23.844Z	27.85	26.9	0.51	368
2023-09-17T05:09:21.216Z	27.85	26.82	0.75	376
2023-09-17T05:14:18.485Z	27.83	27.23	0.56	368
2023-09-17T05:19:15.856Z	27.9	27.43	0.78	376
2023-09-17T05:24:13.228Z	27.86	27.85	0.83	380
2023-09-17T05:29:10.496Z	27.89	27.56	0.78	376
2023-09-17T05:34:07.868Z	27.98	27.5	0.79	376
2023-09-17T05:39:05.14Z	28.09	27.34	0.69	372
2023-09-17T05:44:02.507Z	28.06	27.21	0.62	372
2023-09-17T05:48:59.879Z	28.08	27.61	0.75	373
2023-09-17T05:53:57.044Z	28.13	27.72	0.66	372
2023-09-17T05:58:54.314Z	28.23	27.63	0.51	364
2023-09-17T06:03:51.685Z	28.26	26.71	0.8	379
2023-09-17T06:08:49.056Z	28.36	25.51	0.55	364
2023-09-17T06:13:46.428Z	28.33	25.06	0.69	372
2023-09-17T06:18:43.799Z	28.29	25.57	0.52	364
2023-09-17T06:23:41.068Z	28.21	27.28	0.78	373
2023-09-17T06:28:38.438Z	28.2	28.21	0.53	364
2023-09-17T06:33:35.707Z	28.27	28.68	0.72	373
2023-09-17T06:38:33.078Z	28.32	28.05	0.64	372
2023-09-17T06:43:30.452Z	28.24	28.6	0.76	373
2023-09-17T06:48:27.823Z	28.21	29.26	0.54	364
2023-09-17T06:53:25.196Z	28.21	29.22	0.57	364
2023-09-17T06:58:22.478Z	28.15	30.17	0.8	373
2023-09-17T07:03:19.835Z	28.13	30.7	0.55	363
2023-09-17T07:08:17.205Z	28.08	31.01	0.62	367
2023-09-17T07:13:14.578Z	28.05	31.2	0.65	367
2023-09-17T07:18:12.06Z	28	31.39	0.51	367
2023-09-17T07:23:09.423Z	27.96	31.53	0.54	367
2023-09-17T07:28:06.69Z	27.93	31.6	0.58	367
2023-09-17T07:33:04.062Z	27.89	31.11	0.77	376
2023-09-17T07:38:01.228Z	27.86	31.69	0.57	367
2023-09-17T07:42:58.599Z	27.86	31.69	0.8	377
2023-09-17T07:47:55.869Z	27.87	31.77	0.7	376
2023-09-17T07:52:53.138Z	27.85	31.9	0.8	376
2023-09-17T07:57:50.509Z	27.83	32.64	0.86	377

2023-09-17T08:02:47.879Z	27.8	33.68	0.69	371
2023-09-17T08:07:45.249Z	27.57	34.2	0.86	377
2023-09-17T08:12:42.62Z	27.49	34.58	0.54	367
2023-09-17T08:17:39.992Z	27.45	34.42	0.74	376
2023-09-17T08:22:51.084Z	27.44	34.81	0.66	371
2023-09-17T08:27:48.353Z	27.41	35.44	0.61	368
2023-09-17T08:32:45.847Z	27.45	35.73	0.77	374
2023-09-17T08:37:43.197Z	27.48	37.07	0.84	375
2023-09-17T08:42:40.673Z	27.43	37.38	0.82	375
2023-09-17T08:47:38.045Z	27.34	37.24	0.62	368
2023-09-17T08:52:35.518Z	27.24	37.25	0.63	368
2023-09-17T08:57:32.89Z	27.25	37.24	0.51	361
2023-09-17T09:02:30.28Z	27.27	37.22	0.79	374
2023-09-17T09:07:27.739Z	27.33	36.88	0.73	374
2023-09-17T09:12:25.116Z	27.41	36.75	0.53	361
2023-09-17T09:17:22.579Z	27.42	37.13	0.5	361
2023-09-17T09:22:19.95Z	27.39	37.72	0.84	375
2023-09-17T09:27:17.433Z	27.39	37.67	0.73	374
2023-09-17T09:32:14.797Z	27.3	37.54	0.56	361
2023-09-17T09:37:12.267Z	27.22	37.47	0.76	374
2023-09-17T09:42:09.741Z	27.23	38.06	0.54	361
2023-09-17T09:47:07.216Z	27.16	38.06	0.68	368
2023-09-17T09:52:04.689Z	27.11	40.26	0.87	374
2023-09-17T09:57:02.161Z	27.06	39.37	0.72	374
2023-09-17T10:01:59.537Z	26.93	38.68	0.88	378
2023-09-17T10:06:57.122Z	26.91	37.89	0.77	377
2023-09-17T10:11:54.48Z	26.86	37.77	0.87	378
2023-09-17T10:16:52.056Z	26.83	38.53	0.77	377
2023-09-17T10:21:49.606Z	26.83	39.48	0.55	366
2023-09-17T10:26:47.004Z	26.78	37.93	0.69	372
2023-09-17T10:31:44.581Z	26.75	38.41	0.8	378
2023-09-17T10:36:42.058Z	26.69	39	0.66	372
2023-09-17T10:41:39.53Z	26.64	39.09	0.86	378
2023-09-17T10:46:37.115Z	26.63	39.29	0.65	372
2023-09-17T10:51:34.58Z	26.63	38.83	0.83	378
2023-09-17T10:56:32.075Z	26.66	39.41	0.56	366
2023-09-17T11:01:29.642Z	26.65	39.2	0.68	372
2023-09-17T11:06:27.204Z	26.63	39.01	0.6	372
2023-09-17T11:11:24.703Z	26.59	38.96	0.79	377
2023-09-17T11:16:22.254Z	26.56	38.98	0.54	366
2023-09-17T11:21:19.833Z	26.5	39.33	0.8	377
2023-09-17T11:26:17.416Z	26.48	39.1	0.84	378
2023-09-17T11:31:14.982Z	26.46	39.31	0.61	372
2023-09-17T11:36:12.558Z	26.46	39.76	0.51	366
2023-09-17T11:41:10.031Z	26.42	40.32	0.86	377

2023-09-17T11:46:07.607Z	26.39	40.75	0.88	377
2023-09-17T11:51:05.193Z	26.37	40.99	0.6	365
2023-09-17T11:56:02.657Z	26.33	41.16	0.53	365
2023-09-17T12:01:00.338Z	26.3	41.45	0.66	371
2023-09-17T12:05:57.979Z	26.25	41.64	0.78	374
2023-09-17T12:10:55.487Z	26.2	41.71	0.82	377
2023-09-17T12:15:53.072Z	26.17	41.59	0.8	374
2023-09-17T12:20:50.538Z	26.1	41.79	0.76	374
2023-09-17T12:25:48.115Z	26.07	41.68	0.71	374
2023-09-17T12:30:45.692Z	26.05	41.71	0.64	371
2023-09-17T12:35:43.265Z	25.99	41.41	0.83	380
2023-09-17T12:40:40.841Z	25.96	41.34	0.55	370
2023-09-17T12:45:38.52Z	25.91	41.43	0.74	378
2023-09-17T12:50:36.096Z	25.89	41.46	0.87	380
2023-09-17T12:55:33.672Z	25.87	41.64	0.64	375
2023-09-17T13:00:31.35Z	25.85	42.15	0.89	380
2023-09-17T13:05:28.927Z	25.87	43.21	0.76	378
2023-09-17T13:10:26.708Z	25.83	43.79	0.57	370
2023-09-17T13:15:24.283Z	25.83	43.81	0.54	370
2023-09-17T13:20:21.962Z	25.82	44.46	0.58	370
2023-09-17T13:25:19.642Z	25.84	44.81	0.69	375
2023-09-17T13:30:17.319Z	25.84	45.18	0.53	364
2023-09-17T13:35:14.998Z	25.84	46.03	0.74	375
2023-09-17T13:40:12.779Z	25.83	46.71	0.54	364
2023-09-17T13:45:10.355Z	25.8	47.44	0.58	364
2023-09-17T13:50:08.034Z	25.8	47.22	0.58	364
2023-09-17T13:55:05.816Z	25.79	47.31	0.64	370
2023-09-17T14:00:03.493Z	25.77	48.42	0.52	364
2023-09-17T14:05:01.171Z	25.79	48.28	0.66	370
2023-09-17T14:09:58.955Z	25.76	48.93	0.85	377
2023-09-17T14:14:56.733Z	25.72	48.87	0.61	370
2023-09-17T14:19:54.425Z	25.72	48.94	0.58	364
2023-09-17T14:24:52.091Z	25.71	49.24	0.88	377
2023-09-17T14:29:49.873Z	25.69	49.68	0.73	375
2023-09-17T14:34:47.652Z	25.68	50.04	0.73	373
2023-09-17T14:39:45.433Z	25.67	49.96	0.71	375
2023-09-17T14:44:43.112Z	25.63	50.1	0.84	376
2023-09-17T14:49:40.893Z	25.6	50.43	0.8	373
2023-09-17T14:54:38.572Z	25.55	50.55	0.53	362
2023-09-17T14:59:36.15Z	25.52	50.75	0.62	368
2023-09-17T15:04:33.828Z	25.5	50.72	0.68	368
2023-09-17T15:09:31.512Z	25.49	50.94	0.71	373
2023-09-17T15:14:29.186Z	25.46	50.8	0.65	368
2023-09-17T15:19:26.762Z	25.42	51.29	0.74	373
2023-09-17T15:24:24.44Z	25.42	51.31	0.64	368

2023-09-17T15:29:22.119Z	25.38	51.58	0.81	376
2023-09-17T15:34:19.897Z	25.34	51.66	0.7	368
2023-09-17T15:39:17.576Z	25.33	51.74	0.56	362
2023-09-17T15:44:15.254Z	25.3	51.77	0.67	368
2023-09-17T15:49:13.034Z	25.28	51.51	0.81	376
2023-09-17T15:54:10.714Z	25.26	51.8	0.84	376
2023-09-17T15:59:08.495Z	25.23	51.78	0.69	368
2023-09-17T16:04:06.275Z	25.19	51.68	0.86	376
2023-09-17T16:09:04.056Z	25.17	51.78	0.51	362
2023-09-17T16:14:01.837Z	25.17	51.55	0.52	362
2023-09-17T16:18:59.619Z	25.13	51.61	0.75	373
2023-09-17T16:23:57.399Z	25.09	51.91	0.88	376
2023-09-17T16:28:55.183Z	25.06	51.69	0.83	376
2023-09-17T16:33:52.961Z	25.04	51.88	0.55	362
2023-09-17T16:38:50.741Z	25.01	51.81	0.55	362
2023-09-17T16:43:48.42Z	24.99	51.72	0.73	378
2023-09-17T16:48:46.098Z	24.96	52	0.84	380
2023-09-17T16:53:43.779Z	24.91	52.14	0.67	373
2023-09-17T16:58:41.456Z	24.9	52.18	0.88	380
2023-09-17T17:03:39.237Z	24.86	52.54	0.81	380
2023-09-17T17:08:36.916Z	24.85	52.64	0.66	373
2023-09-17T17:13:34.705Z	24.83	52.83	0.59	368
2023-09-17T17:18:32.477Z	24.84	52.79	0.88	380
2023-09-17T17:23:30.258Z	24.8	53.02	0.72	378
2023-09-17T17:28:27.937Z	24.8	53.05	0.83	380
2023-09-17T17:33:25.82Z	24.79	53.04	0.52	368
2023-09-17T17:38:23.607Z	24.75	53.29	0.53	368
2023-09-17T17:43:21.382Z	24.73	53.31	0.58	368
2023-09-17T17:48:19.163Z	24.69	53.47	0.65	373
2023-09-17T17:53:16.944Z	24.6	53.64	0.7	373
2023-09-17T17:58:14.725Z	24.62	53.34	0.85	380
2023-09-17T18:03:12.506Z	24.63	53.13	0.85	380
2023-09-17T18:08:10.288Z	24.6	52.95	0.83	380
2023-09-17T18:13:08.07Z	24.59	53.07	0.71	378
2023-09-17T18:18:05.849Z	24.52	53.26	0.83	380
2023-09-17T18:23:03.63Z	24.52	52.98	0.81	380
2023-09-17T18:28:01.411Z	24.51	52.99	0.61	373
2023-09-17T18:32:59.09Z	24.46	53.28	0.76	378
2023-09-17T18:37:56.768Z	24.45	53.18	0.52	368
2023-09-17T18:42:54.549Z	24.43	53.09	0.61	373
2023-09-17T18:47:52.33Z	24.42	52.97	0.83	380
2023-09-17T18:52:50.11Z	24.38	53.04	0.64	373
2023-09-17T18:57:47.892Z	24.35	53.11	0.63	373
2023-09-17T19:02:45.775Z	24.32	52.95	0.81	380
2023-09-17T19:07:43.556Z	24.31	52.78	0.82	380

2023-09-17T19:12:41.44Z	24.27	52.79	0.6	373
2023-09-17T19:17:39.322Z	24.24	52.61	0.51	368
2023-09-17T19:22:37.206Z	24.24	52.33	0.78	378
2023-09-17T19:27:34.987Z	24.18	52.39	0.57	368
2023-09-17T19:32:32.768Z	24.12	52.44	0.67	373
2023-09-17T19:37:30.549Z	24.13	52.34	0.75	378
2023-09-17T19:42:28.33Z	24.11	52.43	0.83	380
2023-09-17T19:47:26.11Z	24.07	52.53	0.72	378
2023-09-17T19:52:23.892Z	24.05	52.35	0.79	378
2023-09-17T19:57:21.776Z	24.03	52.31	0.59	368
2023-09-17T20:02:19.556Z	24.02	52.09	0.69	373
2023-09-17T20:07:17.448Z	23.95	52.1	0.58	373
2023-09-17T20:12:15.322Z	23.98	51.84	0.89	376
2023-09-17T20:17:13.107Z	24	51.53	0.63	377
2023-09-17T20:22:11.092Z	23.92	51.37	0.89	376
2023-09-17T20:27:08.876Z	23.86	51.01	0.64	377
2023-09-17T20:32:06.758Z	23.84	50.42	0.76	377
2023-09-17T20:37:04.642Z	23.83	50.24	0.77	377
2023-09-17T20:42:02.421Z	23.82	50.13	0.55	373
2023-09-17T20:47:00.306Z	23.88	50	0.82	376
2023-09-17T20:51:58.295Z	23.8	49.62	0.69	377
2023-09-17T20:56:56.071Z	23.71	49.27	0.7	380
2023-09-17T21:01:53.852Z	23.81	49.07	0.78	380
2023-09-17T21:06:51.735Z	23.77	49.11	0.73	380
2023-09-17T21:11:49.621Z	23.81	49.06	0.72	380
2023-09-17T21:16:47.502Z	23.84	48.65	0.6	373
2023-09-17T21:21:45.393Z	23.82	48.68	0.51	373
2023-09-17T21:26:43.27Z	23.85	49.03	0.81	376
2023-09-17T21:31:41.152Z	23.84	48.03	0.85	376
2023-09-17T21:36:39.035Z	23.86	48.06	0.79	380
2023-09-17T21:41:36.92Z	23.85	47.71	0.59	373
2023-09-17T21:46:34.908Z	23.84	48.07	0.7	377
2023-09-17T21:51:32.789Z	23.87	48.34	0.69	377
2023-09-17T21:56:30.671Z	23.92	49.18	0.58	373
2023-09-17T22:01:28.554Z	23.92	49.64	0.66	377
2023-09-17T22:06:26.541Z	23.91	50.41	0.86	376
2023-09-17T22:11:24.423Z	23.9	50.27	0.88	376
2023-09-17T22:16:22.41Z	23.89	49.33	0.61	377
2023-09-17T22:21:20.395Z	23.89	48.97	0.8	376
2023-09-17T22:26:18.279Z	23.9	49.18	0.74	380
2023-09-17T22:31:16.266Z	23.91	48.36	0.77	380
2023-09-17T22:36:14.147Z	23.91	49.59	0.66	377
2023-09-17T22:41:12.032Z	23.9	49.83	0.58	373
2023-09-17T22:46:09.915Z	23.92	49.26	0.8	376
2023-09-17T22:51:07.695Z	23.95	49.36	0.89	376

2023-09-17T22:56:05.579Z	23.98	49.33	0.79	380
2023-09-17T23:01:03.472Z	24.01	48.68	0.54	370
2023-09-17T23:06:01.346Z	24.02	47.87	0.66	375
2023-09-17T23:10:59.234Z	24.03	48.73	0.81	381
2023-09-17T23:15:57.112Z	24.1	47.53	0.82	381
2023-09-17T23:20:54.995Z	24.14	48.21	0.65	375
2023-09-17T23:25:52.879Z	24.14	48.33	0.73	379
2023-09-17T23:30:50.762Z	24.17	48.4	0.65	375
2023-09-17T23:35:48.551Z	24.19	46.89	0.6	375
2023-09-17T23:40:46.431Z	24.21	48.08	0.58	370
2023-09-17T23:45:44.311Z	24.24	48.08	0.83	381
2023-09-17T23:50:42.09Z	24.28	47.68	0.85	381
2023-09-17T23:55:39.871Z	24.31	47.9	0.59	370
2023-09-18T00:00:37.755Z	24.32	47.91	0.81	381
2023-09-18T00:05:35.536Z	24.36	47.4	0.9	381
2023-09-18T00:10:33.317Z	24.41	47.31	0.8	379
2023-09-18T00:15:31.098Z	24.44	47.52	0.55	370
2023-09-18T00:20:28.778Z	24.48	47.13	0.79	379
2023-09-18T00:25:26.558Z	24.52	47.02	0.56	370
2023-09-18T00:30:24.441Z	24.58	46.76	0.77	379
2023-09-18T00:35:22.222Z	24.62	46.88	0.5	370
2023-09-18T00:40:20.105Z	24.67	47.48	0.64	375
2023-09-18T00:45:18.093Z	24.71	47.13	0.77	379
2023-09-18T00:50:15.874Z	24.75	46.94	0.88	381
2023-09-18T00:55:13.757Z	24.79	46.86	0.55	370
2023-09-18T01:00:11.537Z	24.84	46.63	0.65	375
2023-09-18T01:05:09.317Z	24.89	46.69	0.86	381
2023-09-18T01:10:07.098Z	24.91	46.77	0.56	370
2023-09-18T01:15:04.778Z	24.95	46.67	0.66	375
2023-09-18T01:20:02.559Z	25	46.44	0.56	370
2023-09-18T01:25:00.236Z	25.07	46.31	0.57	364
2023-09-18T01:29:58.017Z	25.11	46.49	0.68	370
2023-09-18T01:34:55.797Z	25.17	46.74	0.54	364
2023-09-18T01:39:53.579Z	25.21	46.63	0.69	370
2023-09-18T01:44:51.257Z	25.28	46.56	0.84	377
2023-09-18T01:49:49.041Z	25.33	46.15	0.79	375
2023-09-18T01:54:46.93Z	25.4	46.75	0.68	370
2023-09-18T01:59:44.703Z	25.45	46.92	0.63	370
2023-09-18T02:04:42.484Z	25.48	46.58	0.79	375
2023-09-18T02:09:40.264Z	25.52	46.29	0.78	375
2023-09-18T02:14:37.943Z	25.54	46.12	0.87	377
2023-09-18T02:19:35.622Z	25.6	45.8	0.61	370
2023-09-18T02:24:33.299Z	25.62	45.59	0.51	364
2023-09-18T02:29:30.977Z	25.66	45.39	0.68	370
2023-09-18T02:34:28.658Z	25.69	45.44	0.5	364

2023-09-18T02:39:26.949Z	25.72	45.19	0.69	370
2023-09-18T02:44:24.533Z	25.73	45.28	0.67	370
2023-09-18T02:49:22.204Z	25.76	45.08	0.62	370
2023-09-18T02:54:19.883Z	25.77	44.75	0.54	370
2023-09-18T02:59:17.458Z	25.8	44.53	0.65	375
2023-09-18T03:04:15.137Z	25.85	44.51	0.62	375
2023-09-18T03:09:12.816Z	25.9	44.67	0.83	380
2023-09-18T03:14:10.597Z	25.95	44.47	0.83	380
2023-09-18T03:19:08.377Z	26.04	44.47	0.51	365
2023-09-18T03:24:06.056Z	26.07	44.38	0.74	374
2023-09-18T03:29:03.837Z	26.1	44.66	0.75	374
2023-09-18T03:34:01.619Z	26.12	44.55	0.57	365
2023-09-18T03:38:59.196Z	26.13	44.43	0.66	371
2023-09-18T03:43:56.975Z	26.17	44.52	0.57	365
2023-09-18T03:48:54.654Z	26.2	44.66	0.74	374
2023-09-18T03:53:52.333Z	26.23	44.93	0.62	371
2023-09-18T03:58:49.908Z	26.28	44.87	0.56	365
2023-09-18T04:03:47.586Z	26.31	45.02	0.7	371
2023-09-18T04:08:45.162Z	26.31	45.17	0.69	365
2023-09-18T04:13:42.738Z	26.36	45.04	0.53	358
2023-09-18T04:18:40.312Z	26.37	45.06	0.74	371
2023-09-18T04:23:37.892Z	26.46	44.58	0.85	377
2023-09-18T04:28:35.464Z	26.58	43.9	0.88	377
2023-09-18T04:33:33.041Z	26.66	43.55	0.86	377
2023-09-18T04:38:30.617Z	26.72	42.46	0.62	371
2023-09-18T04:43:28.295Z	26.8	41.65	0.69	371
2023-09-18T04:48:25.982Z	26.87	41.48	0.67	371
2023-09-18T04:53:23.55Z	26.94	41.06	0.8	377
2023-09-18T04:58:21.126Z	26.94	40.81	0.82	377
2023-09-18T05:03:18.805Z	26.83	41.51	0.59	365
2023-09-18T05:08:16.38Z	26.77	42.01	0.51	365
2023-09-18T05:13:13.956Z	26.75	42.42	0.85	377
2023-09-18T05:18:11.635Z	26.75	42.6	0.59	365
2023-09-18T05:23:09.211Z	26.77	42.82	0.78	374
2023-09-18T05:28:06.787Z	26.77	43.13	0.78	374
2023-09-18T05:33:04.466Z	26.8	43.14	0.62	371
2023-09-18T05:38:02.041Z	26.82	43.3	0.55	365
2023-09-18T05:42:59.618Z	26.85	43.46	0.61	371
2023-09-18T05:47:57.195Z	26.88	43.62	0.84	377
2023-09-18T05:52:54.678Z	26.87	43.77	0.58	365
2023-09-18T05:57:52.364Z	26.87	43.95	0.71	374
2023-09-18T06:02:50.028Z	26.89	44.12	0.81	377
2023-09-18T06:07:47.498Z	26.9	44.16	0.58	365
2023-09-18T06:12:44.974Z	26.88	44.22	0.79	374
2023-09-18T06:17:42.547Z	26.84	44.53	0.54	365

Appendix H Datasheets

Arduino® Nano 33 IoT

Product Reference Manual
SKU: ABX00027

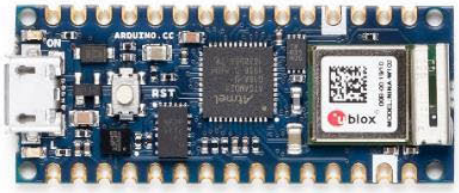

Description

The Arduino Nano 33 IoT and Arduino Nano 33 IoT with headers are a miniature sized module containing a Cortex M0+ SAMD21 processor, a Wi-Fi®+Bluetooth® module based on ESP32, a crypto chip which can securely store certificates and pre-shared keys and a 6 axis IMU. The module can either be mounted as a DIP component (when mounting pin headers), or as a SMT component, directly soldering it via the castellated pads.

Target areas:

Maker, enhancements, basic IoT application scenarios

Arduino® Nano 33 IoT

Features

- **SAMD21G18A**
  - **Processor**
    - 256KB Flash
    - 32KB Flash
    - Power On Reset (POR) and Brown Out Detection (BOD)
  - **Peripherals**
    - 12 channel DMA
    - 12 channel event system
    - 5x 16 bit Timer/Counter
    - 3x 24 bit timer/counter with extended functions
    - 32 bit RTC
    - Watchdog Time
    - CRC-32 generator
    - Full speed Host/Device USB with 8 end points
    - 6x SERCOM (USART, I^2C, SPI, LIN)
    - Two channel I^2S
    - 12 bit 350ksps ADC (up to 16 bit with oversampling)
    - 10 bit 350ksps DAC
    - External Interrupt Controller (up to 16 lines)

- **Nina W102**
  - **Module**
    - Dual Core Tensilica LX6 CPU at up to 240MHz
    - 448 KB ROM, 520KB SRAM, 2MB Flash
  - **WiFi**
    - IEEE 802.11b up to 11Mbit
    - IEEE 802.11g up to 54MBit
    - IEEE 802.11n up to 72MBit
    - 2.4 GHz, 13 channels
    - -96 dBm sensitivity
  - **Bluetooth® BR/EDR**
    - Max 7 peripherals
    - 2.4 GHz, 79 channels
    - Up to 3 Mbit/s
    - 8 dBm output power at 2/3 Mbit/s
    - 11 dBm EIRP at 2/3 Mbit/s
    - -88 dBm sensitivity
  - **Bluetooth® Low Energy**
    - Bluetooth® 4.2 dual mode
    - 2.4GHz 40 channels
    - 6 dBm output power
    - 9 dBm EIRP
    - -88 dBm sensitivity
    - Up to 1 Mbit/
  - **MPM3610** (DC-DC)
    - Regulates input voltage from up to 21V with a minimum of 65% efficiency @minimum load
    - More than 85% efficiency @12V
  - **ATECC608A** (Crypto Chip)
    - Cryptographic co-processor with secure hardware based key storage
    - Protected storage for up to 16 keys, certificates or data
    - ECDH: FIPS SP800-56A Elliptic Curve Diffie-Hellman
    - NIST standard P256 elliptic curve support
    - SHA-256 & HMAC hash including off-chip context save/restore
    - AES-128 encrypt/decrypt, galois field multiply for GCM
  - **LSM6DSL** (6 axis IMU)
    - Always-on 3D accelerometer and 3D gyroscope
    - Smart FIFO up to 4 KByte based
    - ±2/±4/±8/±16 g full scale
    - ±125/±250/±500/±1000/±2000 dps full scale

Contents

1 The Board

As all Nano form factor boards, Nano 33 IoT and Nano 33 IoT with headers does not have a battery charger but can be powered through USB or headers.

NOTE: Arduino Nano 33 IoT and Nano 33 IoT with headers only supports 3.3V I/Os and is **NOT** 5V tolerant so please make sure you are not directly connecting 5V signals to this board or it will be damaged. Also, as opposed to Arduino Nano boards that support 5V operation, the 5V pin does NOT supply voltage but is rather connected, through a jumper, to the USB power input.

1.1 Application Examples

Weather station: Using the Arduino Nano 33 IoT or Nano 33 IoT with headers together with a sensor and a OLED display, we can create a small weather station communicating temperature, humidity etc. directly to your phone.

Air quality monitor: Bad air quality may have serious effects on your health. By assembling the board, with a sensor and monitor you can make sure that the air quality is kept in indoor-environments. By connecting the hardware assembly to an IoT application/API, you will receive real time values.

Air drum: A quick and fun project is to create a small air drum. Connect your board and upload your sketch from the Create Web Editor and start creating beats with your audio workstation of your choice.

2 Ratings

2.1 Recommended Operating Conditions

Symbol	Description	Min	Max
	Conservative thermal limits for the whole board:	-40 °C (40 °F)	85°C (185 °F)

2.2 Power Consumption

Symbol	Description	Min	Typ	Max	Unit
VINMax	Maximum input voltage from VIN pad	-0.3	-	21	V
VUSBMax	Maximum input voltage from USB connector	-0.3	-	21	V
PMax	Maximum Power Consumption	-	-	TBC	mW

3 Functional Overview

3.1 Board Topology

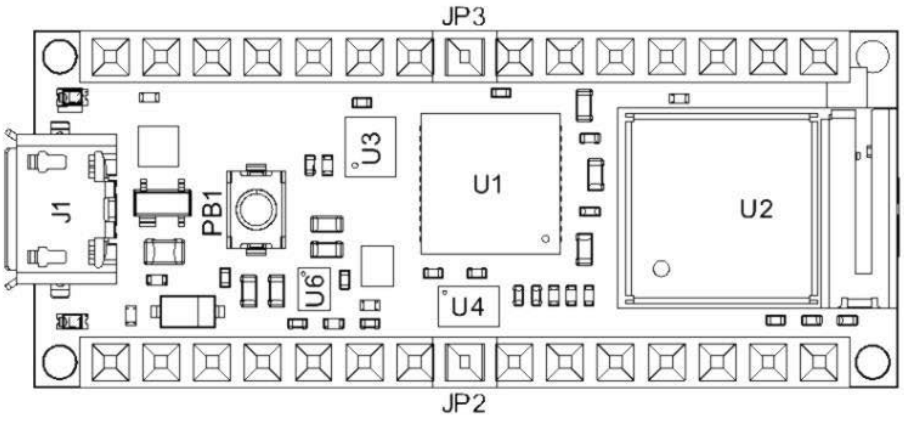

Board topology top

Ref.	Description	Ref.	Description
U1	ATSAMD21G18A Controller	U3	LSM6DSOXTR IMU Sensor
U2	NINA-W102-00B WiFi/BLE Module	U4	ATECC608A-MAHDA-T Crypto Chip
J1	Micro USB Connector	PB1	IT-1185-160G-GTR Push button

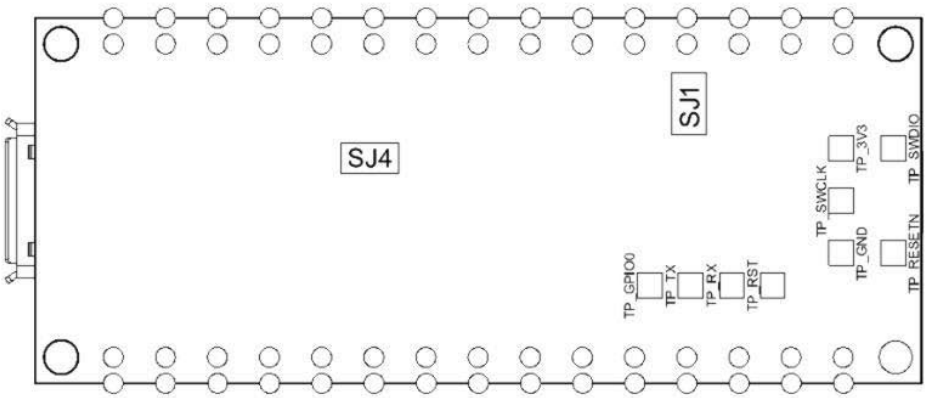

Board topology bottom

Ref.	Description	Ref.	Description
SJ1	Open solder bridge (VUSB)	SJ4	Closed solder bridge (+3V3)

Ref.	Description	Ref.	Description
TP	Test points	xx	Lorem Ipsum

3.2 Processor

The Main Processor is a Cortex M0+ running at up to 48MHz. Most of its pins are connected to the external headers, however some are reserved for internal communication with the wireless module and the on-board internal I^2C peripherals (IMU and Crypto).

NOTE: As opposed to other Arduino Nano boards, pins A4 and A5 have an internal pull up and default to be used as an I^2C Bus so usage as analog inputs is not recommended.

Communication with NINA W102 happens through a serial port and a SPI bus through the following pins.

SAMD21 Pin	SAMD21 Acronym	NINA Pin	NINA Acronym	Description
13	PA08	19	RESET_N	Reset
39	PA27	27	GPIO0	Attention Request
41	PA28	7	GPIO33	Acknowledge
23	PA14	28	GPIO5	SPI CS
21	GPIO19	UART RTS		
24	PA15	29	GPIO18	SPI CLK
20	GPIO22	UART CTS		
22	PA13	1	GPIO21	SPI MISO
21	PA12	36	GPIO12	SPI MOSI
31	PA22	23	GPIO3	Processor TX Nina RX
32	PA23	22	GPIO1	Processor RX Nina TX

3.3 WiFi/BT Communication Module

Nina W102 is based on ESP32 and is delivered with a pre-certified software stack from Arduino. Source code for the firmware is available **[9]**.

NOTE: Reprogramming the wireless module's firmware with a custom one will invalidate compliance with radio standards as certified by Arduino, hence this is not recommended unless the application is used in private laboratories far from other electronic equipment and people. Usage of custom firmware on radio modules is the sole responsibility of the user.

Some of the module's pins are connected to the external headers and can be directly driven by ESP32 provided SAMD21's corresponding pins are aptly tri-stated. Below is a list of such signals:

SAMD21 Pin	SAMD21 Acronym	NINA Pin	NINA Acronym	Description
48	PB03	8	GPIO21	A7
14	PA09	5	GPIO32	A6
8	PB09	31	GPIO14	A5/SCL
7	PB08	35	GPIO13	A4/SDA

3.4 Crypto

The crypto chip in Arduino IoT boards is what makes the difference with other less secure boards as it provides a secure way to store secrets (such as certificates) and accelerates secure protocols while never exposing secrets in plain text.

Source code for the Arduino Library that supports the Crypto is available **[10]**

3.5 IMU

The board has an embedded 6 axis IMU which can be used to measure board orientation (by checking the gravity acceleration vector orientation) or to measure shocks, vibration, acceleration and rotation speed.

Source code for the Arduino Library that supports the IMU is available **[11]**

3.6 Power Tree

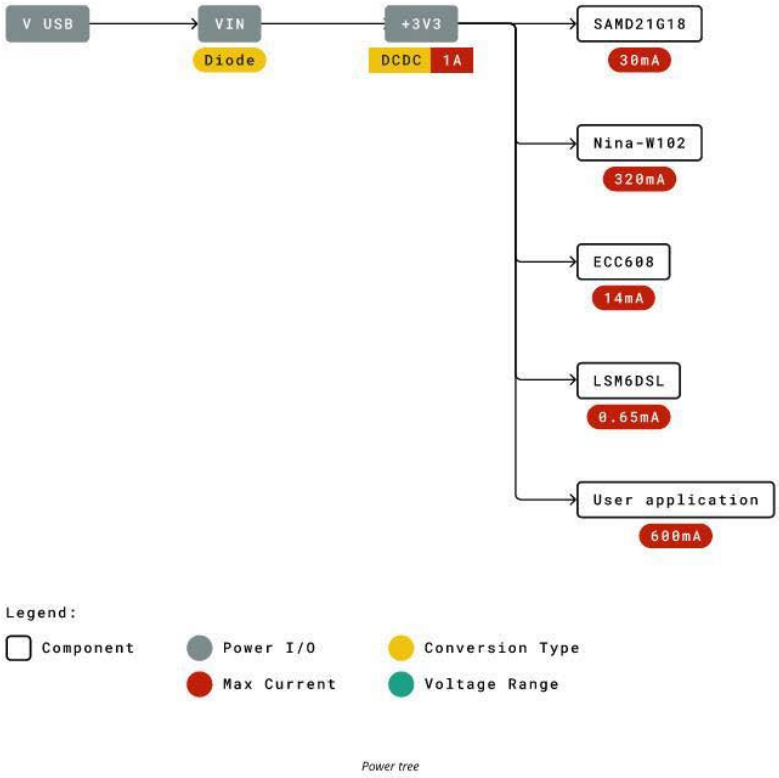

Power tree

4 Board Operation

4.1 Getting Started - IDE

If you want to program your board while offline you need to install the Arduino Desktop IDE [1] To connect the Arduino 33 IoT to your computer, you'll need a Micro-B USB cable. This also provides power to the board, as indicated by the LED.

4.2 Getting Started - Arduino Web Editor

All Arduino boards, including this one, work out-of-the-box on the Arduino Web Editor [2], by just installing a simple plugin.

The Arduino Web Editor is hosted online, therefore it will always be up-to-date with the latest features and support for all boards. Follow **[3]** to start coding on the browser and upload your sketches onto your board.

4.3 Getting Started - Arduino IoT Cloud

All Arduino IoT enabled products are supported on Arduino IoT Cloud which allows you to Log, graph and analyze sensor data, trigger events, and automate your home or business.

4.4 Sample Sketches

Sample sketches for the Arduino 33 IoT can be found either in the "Examples" menu in the Arduino IDE or in the "Documentation" section of the Arduino Pro website [4]

4.5 Online Resources

Now that you have gone through the basics of what you can do with the board you can explore the endless possibilities it provides by checking exciting projects on ProjectHub **[5]**, the Arduino Library Reference **[6]** and the online store **[7]** where you will be able to complement your board with sensors, actuators and more

4.6 Board Recovery

All Arduino boards have a built-in bootloader which allows flashing the board via USB. In case a sketch locks up the processor and the board is not reachable anymore via USB it is possible to enter bootloader mode by double-tapping the reset button right after power up.

5 Connector Pinouts

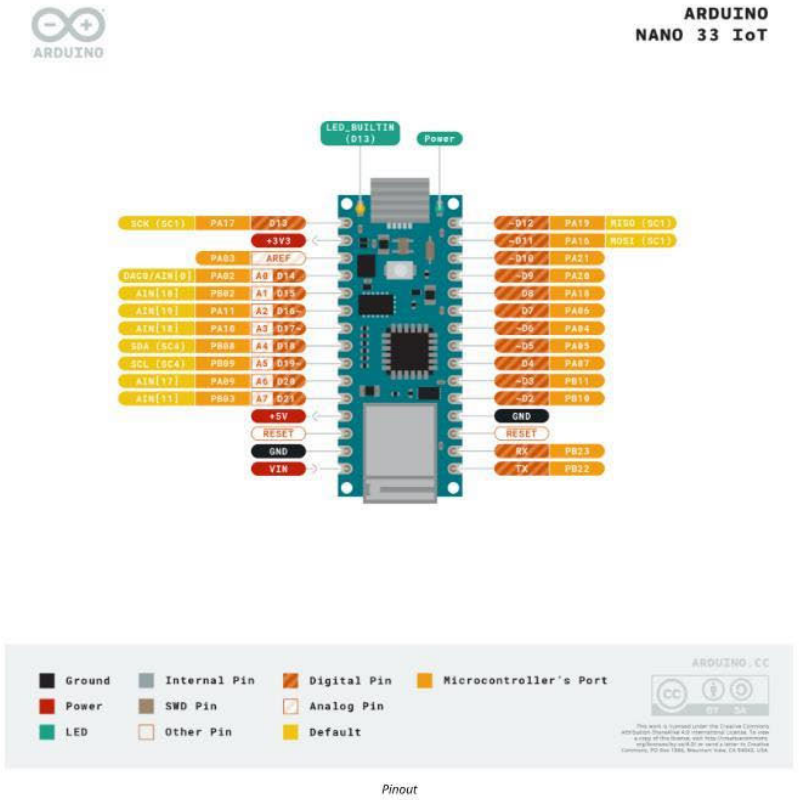

Pinout

5.1 USB

Pin	Function	Type	Description
1	VUSB	Power	Power Supply Input. If board is powered via VUSB from header this is an Output **(1)**
2	D-	Differential	USB differential data -
3	D+	Differential	USB differential data +
4	ID	Analog	Selects Host/Device functionality
5	GND	Power	Power Ground

1. The board can support USB host mode only if powered via the V_{USB} pin and if the jumper close to the VUSB pin is shorted.

5.2 Headers

The board exposes two 15 pin connectors which can either be assembled with pin headers or soldered through castellated vias.

Pin	Function	Type	Description
1	D13	Digital	GPIO
2	+3V3	Power Out	Internally generated power output to external devices
3	AREF	Analog	Analog Reference; can be used as GPIO
4	A0/DAC0	Analog	ADC in/DAC out; can be used as GPIO
5	A1	Analog	ADC in; can be used as GPIO
6	A2	Analog	ADC in; can be used as GPIO
7	A3	Analog	ADC in; can be used as GPIO
8	A4/SDA	Analog	ADC in; I2C SDA; Can be used as GPIO **(1)**
9	A5/SCL	Analog	ADC in; I2C SCL; Can be used as GPIO **(1)**
10	A6	Analog	ADC in; can be used as GPIO
11	A7	Analog	ADC in; can be used as GPIO
12	VUSB	Power In/Out	Normally NC; can be connected to VUSB pin of the USB connector by shorting a jumper
13	RST	Digital In	Active low reset input (duplicate of pin 18)
14	GND	Power	Power Ground
15	VIN	Power In	Vin Power input
16	TX	Digital	USART TX; can be used as GPIO
17	RX	Digital	USART RX; can be used as GPIO
18	RST	Digital	Active low reset input (duplicate of pin 13)
19	GND	Power	Power Ground
20	D2	Digital	GPIO
21	D3/PWM	Digital	GPIO; can be used as PWM
22	D4	Digital	GPIO
23	D5/PWM	Digital	GPIO; can be used as PWM
24	D6/PWM	Digital	GPIO, can be used as PWM
25	D7	Digital	GPIO
26	D8	Digital	GPIO
27	D9/PWM	Digital	GPIO; can be used as PWM
28	D10/PWM	Digital	GPIO; can be used as PWM
29	D11/MOSI	Digital	SPI MOSI; can be used as GPIO
30	D12/MISO	Digital	SPI MISO; can be used as GPIO

5.3 Debug

On the bottom side of the board, under the communication module, debug signals are arranged as 3x2 test pads with 100 mil pitch. Pin 1 is depicted in Figure 3 – Connector Positions

Pin	Function	Type	Description
1	+3V3	Power Out	Internally generated power output to be used as voltage reference
2	SWD	Digital	SAMD11 Single Wire Debug Data
3	SWCLK	Digital In	SAMD11 Single Wire Debug Clock
4	UPDI	Digital	ATMega4809 update interface
5	GND	Power	Power Ground
6	RST	Digital In	Active low reset input

6 Mechanical Information

6.1 Board Outline and Mounting Holes

The board measures are mixed between metric and imperial. Imperial measures are used to maintain a 100 mil pitch grid between pin rows to allow them to fit a breadboard whereas board length is Metric.

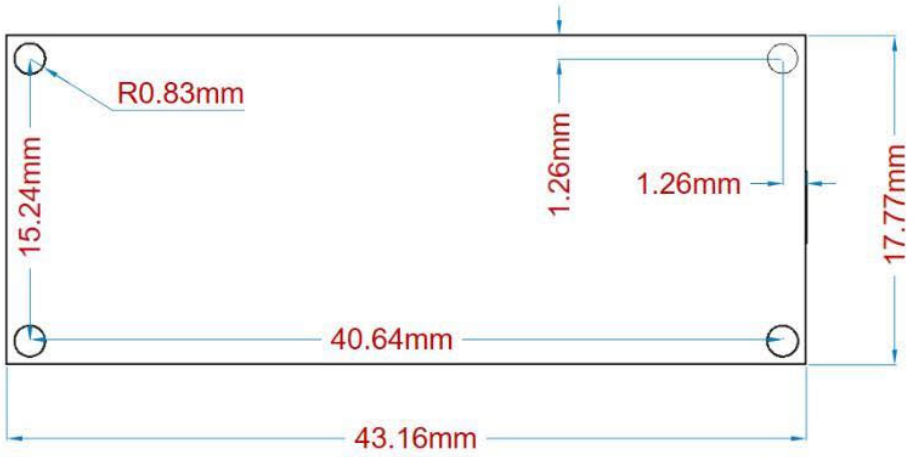

Layout

6.2 Connector Positions

The view below is from top however it shows Debug connector pads which are on the bottom side. Highlighted pins are pin 1 for each connector'

Top view:

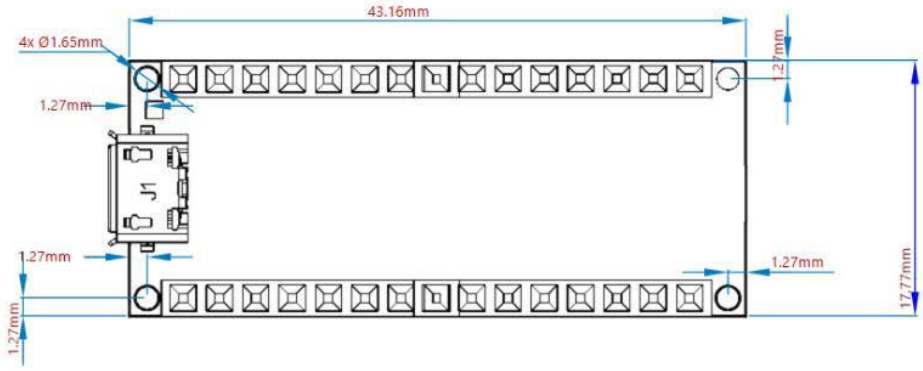

Top side connectors

Bottom view:

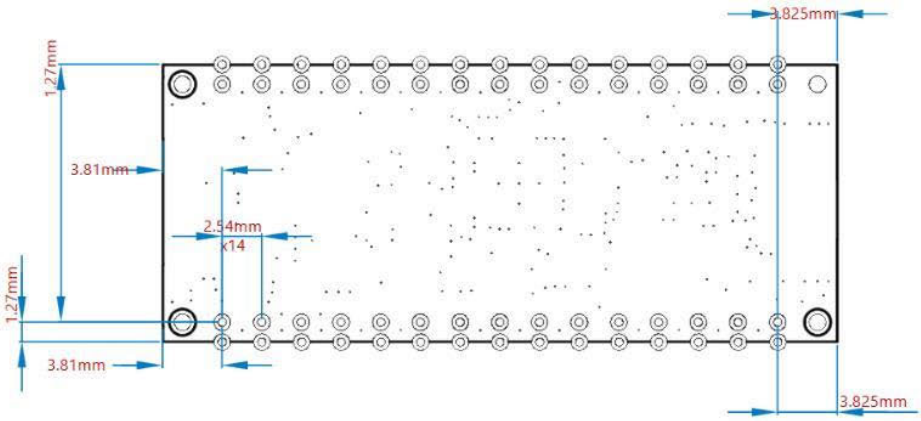

Bottom side connectors

7 Certifications

7.1 Declaration of Conformity CE DoC (EU)

We declare under our sole responsibility that the products above are in conformity with the essential requirements of the following EU Directives and therefore qualify for free movement within markets comprising the European Union (EU) and European Economic Area (EEA).

7.2 Declaration of Conformity to EU RoHS & REACH 211 01/19/2021

Arduino boards are in compliance with RoHS 2 Directive 2011/65/EU of the European Parliament and RoHS 3 Directive 2015/863/EU of the Council of 4 June 2015 on the restriction of the use of certain hazardous substances in electrical and electronic equipment.

Substance	Maximum limit (ppm)
Lead (Pb)	1000
Cadmium (Cd)	100
Mercury (Hg)	1000
Hexavalent Chromium (Cr6+)	1000
Poly Brominated Biphenyls (PBB)	1000
Poly Brominated Diphenyl ethers (PBDE)	1000
Bis(2-Ethylhexyl} phthalate (DEHP)	1000
Benzyl butyl phthalate (BBP)	1000
Dibutyl phthalate (DBP)	1000
Diisobutyl phthalate (DIBP)	1000

Exemptions : No exemptions are claimed.

Arduino Boards are fully compliant with the related requirements of European Union Regulation (EC) 1907 /2006 concerning the Registration, Evaluation, Authorization and Restriction of Chemicals (REACH). We declare none of the SVHCs (https://echa.europa.eu/web/guest/candidate-list-table), the Candidate List of Substances of Very High Concern for authorization currently released by ECHA, is present in all products (and also package) in quantities totaling in a concentration equal or above 0.1%. To the best of our knowledge, we also declare that our products do not contain any of the substances listed on the "Authorization List" (Annex XIV of the REACH regulations) and Substances of Very High Concern (SVHC) in any significant amounts as specified by the Annex XVII of Candidate list published by ECHA (European Chemical Agency) 1907 /2006/EC.

7.3 Conflict Minerals Declaration

As a global supplier of electronic and electrical components, Arduino is aware of our obligations with regards to laws and regulations regarding Conflict Minerals, specifically the Dodd-Frank Wall Street Reform and Consumer Protection Act, Section 1502. Arduino does not directly source or process conflict minerals such as Tin, Tantalum, Tungsten, or Gold. Conflict minerals are contained in our products in the form of solder, or as a component in metal alloys. As part of our reasonable due diligence Arduino has contacted component suppliers within our supply chain to verify their continued compliance with the regulations. Based on the information received thus far we declare that our products contain Conflict Minerals sourced from conflict-free areas.

8 FCC Caution

Any Changes or modifications not expressly approved by the party responsible for compliance could void the user's authority to operate the equipment.

This device complies with part 15 of the FCC Rules. Operation is subject to the following two conditions:

(1) This device may not cause harmful interference

(2) this device must accept any interference received, including interference that may cause undesired operation.

FCC RF Radiation Exposure Statement:

1. This Transmitter must not be co-located or operating in conjunction with any other antenna or transmitter.
2. This equipment complies with RF radiation exposure limits set forth for an uncontrolled environment.
3. This equipment should be installed and operated with minimum distance 20cm between the radiator & your body.

English: User manuals for license-exempt radio apparatus shall contain the following or equivalent notice in a conspicuous location in the user manual or alternatively on the device or both. This device complies with Industry Canada license-exempt RSS standard(s). Operation is subject to the following two conditions:

(1) this device may not cause interference

(2) this device must accept any interference, including interference that may cause undesired operation of the device.

French: Le présent appareil est conforme aux CNR d'Industrie Canada applicables aux appareils radio exempts de licence. L'exploitation est autorisée aux deux conditions suivantes :

(1) l' appareil nedoit pas produire de brouillage

(2) l'utilisateur de l'appareil doit accepter tout brouillage radioélectrique subi, même si le brouillage est susceptible d'en compromettre le fonctionnement.

IC SAR Warning:

English This equipment should be installed and operated with minimum distance 20 cm between the radiator and your body.

French: Lors de l' installation et de l' exploitation de ce dispositif, la distance entre le radiateur et le corps est d 'au moins 20 cm.

Important: The operating temperature of the EUT can't exceed 85°C and shouldn't be lower than -40°C.

Hereby, Arduino S.r.l. declares that this product is in compliance with essential requirements and other relevant provisions of Directive 2014/53/EU. This product is allowed to be used in all EU member states.

Frequency bands	Maximum output power (EIRP)
2402-2480MHz(EDR)	6.24 dBm
2402-2480MHz(BLE)	6.30 dBm
2412-2472MHz(2.4G WiFi)	13.61 dBm

9 Company Information

Company name	Arduino S.r.l
Company Address	Via Andrea Appiani,2520900 MONZA

10 Reference Documentation

Reference	Link
Arduino IDE (Desktop)	https://www.arduino.cc/en/software
Arduino IDE (Cloud)	https://create.arduino.cc/editor
Cloud IDE Getting Started	https://create.arduino.cc/projecthub/Arduino_Genuino/getting-started-with-arduino-web-editor-4b3e4a
Forum	http://forum.arduino.cc/
SAMD21G18	https://ww1.microchip.com/downloads/aemDocuments/documents/MCU32/ProductDocuments/DataSheets/SAM-D21DA1-Family-Data-Sheet-DS40001882G.pdf
NINA W102	https://content.u-blox.com/sites/default/files/NINA-W10_DataSheet_UBX-17065507.pdf
ECC608	https://ww1.microchip.com/downloads/aemDocuments/documents/SCBU/ProductDocuments/DataSheets/ATECC608A-CryptoAuthentication-Device-Summary-Data-Sheet-DS40001977B.pdf
MPM3610	https://www.monolithicpower.com/pub/media/document/MPM3610_r1.01.pdf
NINA Firmware	https://github.com/arduino/nina-fw
ECC608 Library	https://github.com/arduino-libraries/ArduinoECCX08
LSM6DSL Library	https://github.com/stm32duino/LSM6DSL
ProjectHub	https://create.arduino.cc/projecthub?by=part&part_id=11332&sort=trending
Library Reference	https://www.arduino.cc/reference/en/
Arduino Store	https://store.arduino.cc/

11 Revision History

Date	Revision	Changes
03/08/2022	2	Reference documentation links updates
15/04/2021	1	General datasheet updates

Innovative Sensor Technology
physical. chemical. biological.

FS7.A.1L.195

Thermal Mass Flow Sensor

Optimal for various gas flow applications up to 150 °C

Benefits & Characteristics

- Easy adaptation in various applications and housings
- Simple signal processing
- Simple calibration
- Stable platinum technology
- Excellent long-term stability
- Excellent reproducibility
- Symmetrical heater design and heightened sensitivity

Illustration[1)]

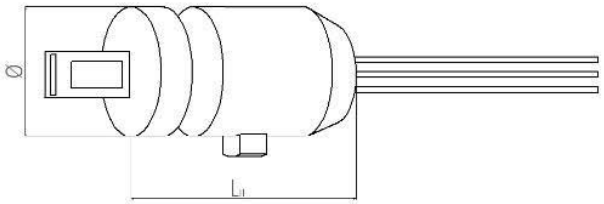

1) For actual size, see dimensions

Technical Data

Dimensions (L x W x H / H2 in mm):	Ø 6.0 (±0.1) mm, L_H = 14 (±0.2) mm (complete dimensions in application note)
Operating measuring range:	0 m/s to 100 m/s
Response sensitivity:	0.01 m/s
Accuracy:	< 3 % of the measured value (dependent on the electronics and calibration)
Response time t_{63}:	~200 ms (jump from 0 to 10000 sccm)
Operating temperature range:	-20 °C to +150 °C
Temperature sensitivity:	< 0.1 %/K (dependent on the electronics)
Connection:	3 pins, AWG 30/7, stranded wire, insulated with PTFE, 195 mm long
Heater:	R_H (0 °C) = 45 Ω ±1 %
Reference element:	R_S (0 °C) = 1200 Ω ±1 %
Voltage range (nominal):	2 V to 5 V (at Δ T = 30 K (0 m/s ≤ v_{gas} ≤ 100 m/s)
Maximum heater voltage:	3 V (at 0 m/s)
Construction:	Moulded plastic housing

iST Innovative Sensor Technology
physical. chemical. biological.

Product Photo

Pin Assignment

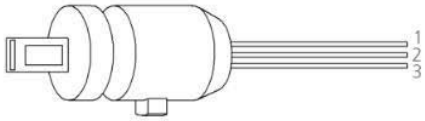

1	2	3
heater	temperature sensor	GND

Order Information

Description:	Item number:	Former main reference:
FS7.A.1L.195	103706	050.00217

Additional Electronics

Description:	Item number:	Former main reference:
Flow Demo Board FS7 - board without sensor	104017	160.00022
Flow Demo Board FS7 - board with FS7 sensor (with housing)	104018	160.00023

RoHS

Innovative Sensor Technology IST AG, Stegrütistrasse 14, 9642 Ebnat-Kappel, Switzerland
Phone: +41 71 992 01 00 | Fax: +41 71 992 01 99 | Email: info@ist-ag.com | www.ist-ag.com

Innovative Sensor Technology
physical. chemical. biological.

Additional Documents

	Document name:
Application Note:	AFFS7_E

Innovative Sensor Technology IST AG, Stegrütistrasse 14, 9642 Ebnat-Kappel, Switzerland
Phone: +41 71 992 01 00 | Fax: +41 71 992 01 99 | Email: info@ist-ag.com | www.ist-ag.com

Adafruit BME280 Humidity + Barometric Pressure + Temperature Sensor Breakout

Created by lady ada

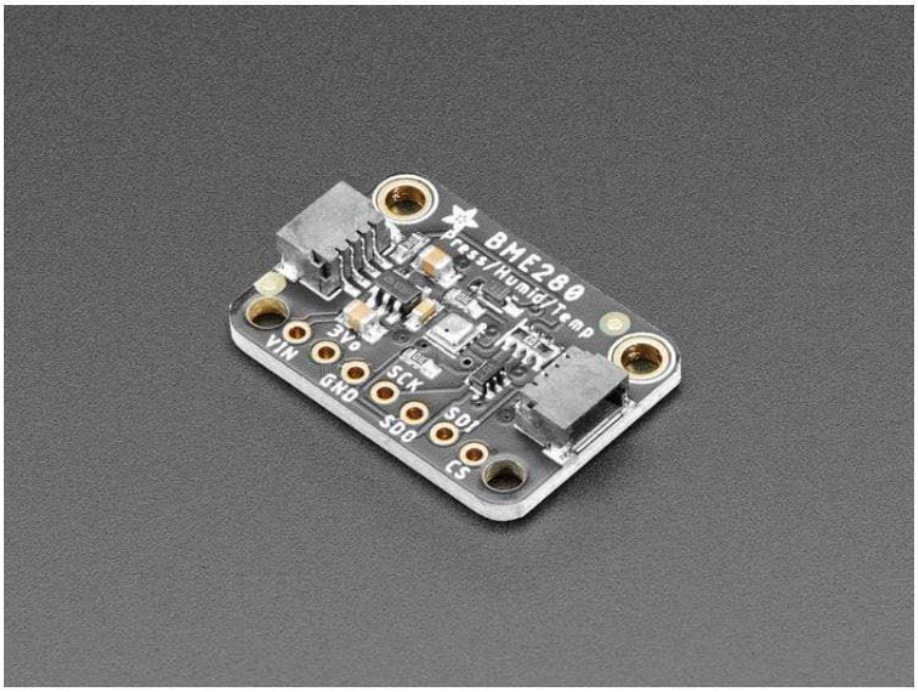

https://learn.adafruit.com/adafruit-bme280-humidity-barometric-pressure-temperature-sensor-breakout

Last updated on 2023-08-29 02:58:21 PM EDT

Table of Contents

Overview

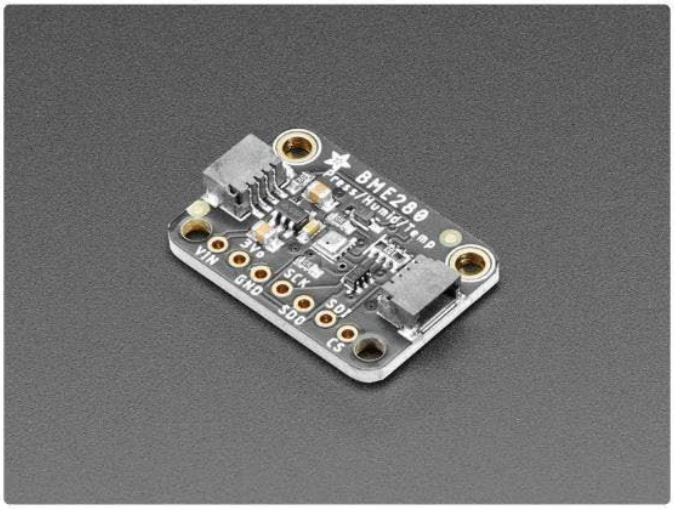

Bosch has stepped up their game with their new BME280 sensor, an environmental sensor with temperature, barometric pressure and humidity! This sensor is great for all sorts of weather/environmental sensing and can even be used in both I2C and SPI!

This precision sensor from Bosch is the best low-cost sensing solution for measuring humidity with ±3% accuracy, barometric pressure with ±1 hPa absolute accuraccy, and temperature with ±1.0°C accuracy. Because pressure changes with altitude, and the pressure measurements are so good, you can also use it as an altimeter with ±1 meter accuracy!

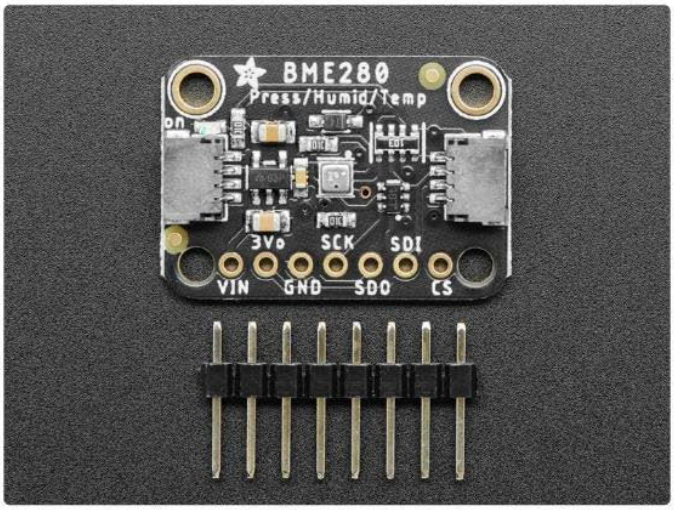

The BME280 is the next-generation of sensors from Bosch, and is the upgrade to the BMP085/BMP180/BMP183 - with a low altitude noise of 0.25m and the same fast conversion time. It has the same specifications, but can use either I2C or SPI. For simple easy wiring, go with I2C. If you want to connect a bunch of sensors without worrying about I2C address collisions, go with SPI.

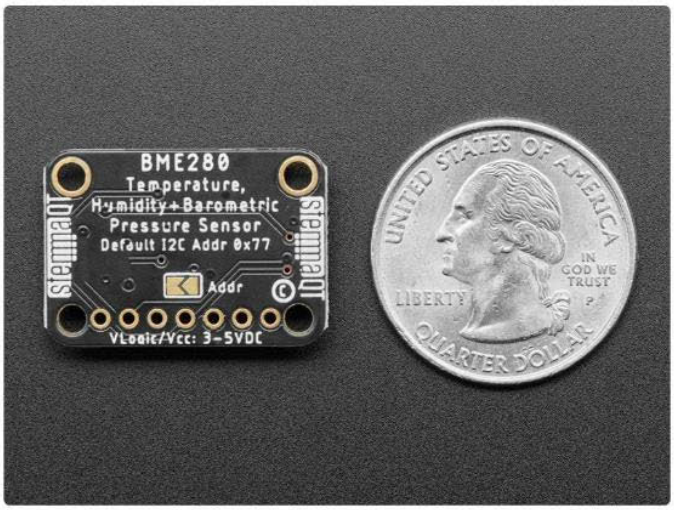

Nice sensor right? So we made it easy for you to get right into your next project. The surface-mount sensor is soldered onto a PCB and comes with a 3.3V regulator and level shifting so you can use it with a 3V or 5V logic microcontroller without worry.

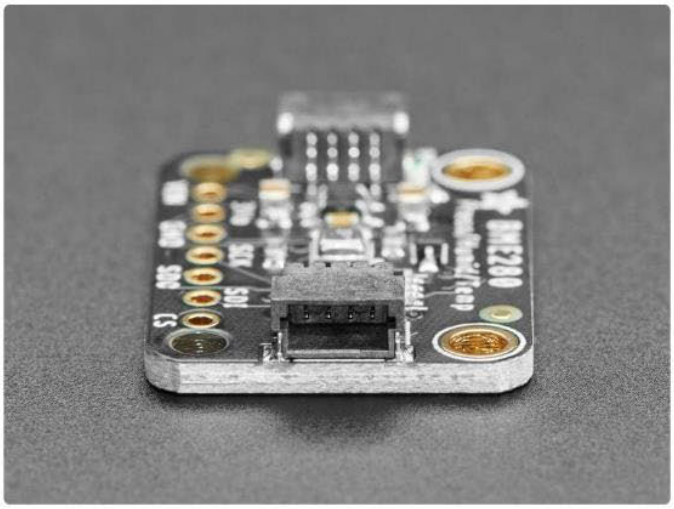

The breakout is made in the STEMMA QT form factor (), making them easy to interface with. The STEMMA QT connectors () on either side are compatible with the SparkFun

Qwiic () I2C connectors. This allows you to make solderless connections between your development board and the BME280 or to chain it with a wide range of other sensors and accessories using a compatible cable ().

There are two versions of this board - the STEMMA QT version shown above, and the original header-only version shown below. Code works the same on both!

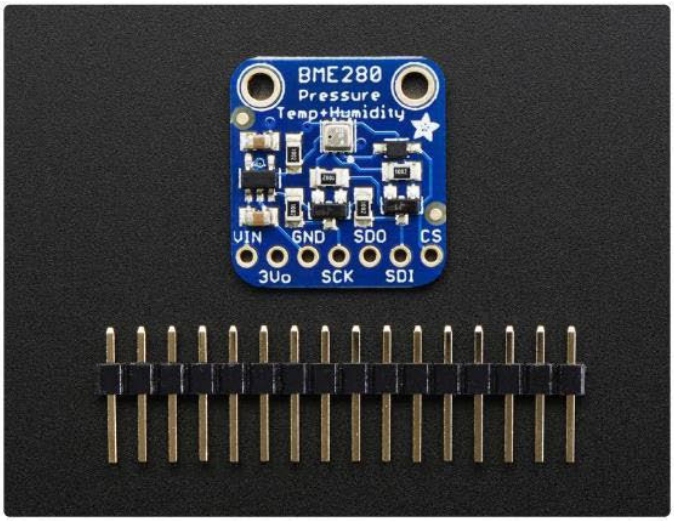

Pinouts

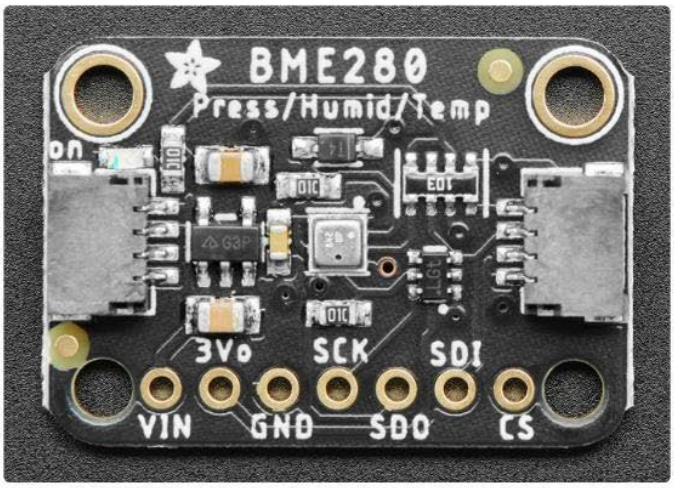

Power Pins:

- Vin - this is the power pin. Since the sensor chip uses 3 VDC, we have included a voltage regulator on board that will take 3-5VDC and safely convert it down. To power the board, give it the same power as the logic level of your microcontroller - e.g. for a 5V micro like Arduino, use 5V
- 3Vo - this is the 3.3V output from the voltage regulator, you can grab up to 100mA from this if you like
- GND - common ground for power and logic

SPI Logic pins:

All pins going into the breakout have level shifting circuitry to make them 3-5V logic level safe. Use whatever logic level is on Vin!

- SCK - This is the SPI Clock pin, its an input to the chip
- SDO - this is the Serial Data Out / Microcontroller In Sensor Out pin, for data sent from the BMP183 to your processor
- SDI - this is the Serial Data In / Microcontroller Out Sensor In pin, for data sent from your processor to the BME280

- CS - this is the Chip Select pin, drop it low to start an SPI transaction. Its an input to the chip

If you want to connect multiple BME280's to one microcontroller, have them share the SDI, SDO and SCK pins. Then assign each one a unique CS pin.

I2C Logic pins:

- SCK - this is also the I2C clock pin, connect to your microcontrollers I2C clock line.
- SDI - this is also the I2C data pin, connect to your microcontrollers I2C data line.
- STEMMA QT () - These connectors allow you to connectors to dev boards with S TEMMA QT connectors or to other things with various associated accessories ()

Leave the other pins disconnected.

I2C Address

By default, the I2C address is 0x77. If you add a jumper from SDO to GND with a wire, or by soldering the ADDR jumper on the back closed, the address will change to 0x76. This non-default address will need to be specified in user code. See library docs for specifics.

Don't forget to update your user code to also specify the non-default I2C address if it is used.

Assembly

Your board may look a little different - the assembly process is the same!

TEXAS INSTRUMENTS
OP07, OP07C, OP07D
SLOS099H – SEPTEMBER 1983 – REVISED MARCH 2023

OP07x Precision Operational Amplifiers

1 Features

- Low noise
- No external components required
- Replace chopper amplifiers at a lower cost
- Wide input-voltage range:
  0 V to ±14 V (typ, ±15-V supply)
- Wide supply-voltage range: ±3 V to ±18 V

2 Applications

- Analog input module
- Battery test
- Lab and field instrumentation
- Temperature transmitter
- Merchant network & server PSU

3 Description

The OP07C and OP07D (OP07x) devices offer low offset and long-term stability by means of a low-noise, chopperless, bipolar-input-transistor amplifier circuit. For most applications, external components are not required for offset nulling and frequency compensation. The true differential input, with a wide input-voltage range and outstanding common-mode rejection, provides maximum flexibility and performance in high-noise environments and in noninverting applications. Low bias currents and extremely high input impedances are maintained over the entire temperature range.

For improved performance and wider temperature range, see the next generation OPA207 with low power, and OPA202 with heavy capacitive load drive capability.

Package Information

PART NUMBER	PACKAGE(1)	BODY SIZE (NOM)
OP07C, OP07D	D (SOIC, 8)	4.90 mm × 3.91 mm
	P (PDIP, 8)	9.81 mm × 6.35 mm
	PS (SO, 8)	6.20 mm × 5.30 mm

(1) For all available packages and the OP07, see the orderable addendum at the end of the data sheet.

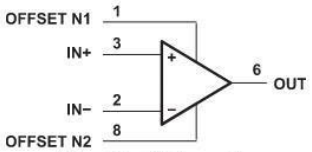

Simplified Schematic

Table of Contents

4 Revision History

NOTE: Page numbers for previous revisions may differ from page numbers in the current version.

Changes from Revision G (November 2014) to Revision H (July 2022)	Page
• Added supply condition to wide input voltage range feature bullet	1
• Changed VCC_+ to V+ and VCC_- to V−	3
• Changed supply voltage abbreviation from VCC+ and VCC– to V_S in *Absolute Maximum Ratings* and throughout the data sheet	4
• Changed note 5 in *Absolute Maximum Ratings* to include a note that fast-ramping shorts to the positive supply can damage the device	4
• Changed Electrostatic discharge Human-body model and Charged-device model from 1000 V to ±1000 V	4
• Added new values to *Thermal Information*	4
• Changed *Electrical Characteristics* format	5
• Changed parameter name from supply-voltage sensitivity to power supply rejection ratio in *Electrical Characteristics*	5
• Changed parameter name from input offset voltage to Input voltage noise density in *Electrical Characteristics*	5
• Changed input current noise density unit from nV/√Hz to pA/√Hz in *Electrical Characteristics*	5
• Changed parameter name from large-signal differential voltage gain to open-loop voltage gain in *Electrical Characteristics*	5
• Changed parameter name from peak output voltage to voltage output swing in Electrical Characteristics	5
• Changed functional block diagram	7
• Changed text to clarify how to adjust input mismatches using null pins in *Application Information*	8

Changes from Revision F (January 2014) to Revision G (November 2014)	Page
• Added *Applications*, *Device Information* table, *Pin Functions* table, *Handling Ratings* table, *Thermal Information* table, *Typical Characteristics*, *Feature Description* section, *Device Functional Modes*, *Application and Implementation* section, *Power Supply Recommendations* section, *Layout* section, *Device and Documentation Support* section, and *Mechanical, Packaging, and Orderable Information* section	1

Changes from Revision E (May 2004) to Revision F (January 2014)	Page
• Deleted *Ordering Information* table	1

5 Pin Configuration and Functions

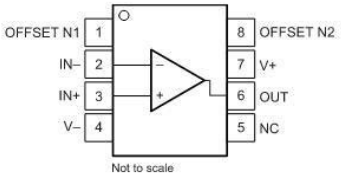

Figure 5-1. D Package, 8-Pin SOIC, P Package, 8-Pin PDIP, and PS Package, 8-Pin SO (Top View)

Table 5-1. Pin Functions

PIN		TYPE	DESCRIPTION
NAME	NO.		
IN+	3	Input	Noninverting input
IN–	2	Input	Inverting input
NC	5	—	Do not connect
OFFSET N1	1	Input	External input offset voltage adjustment
OFFSET N2	8	Input	External input offset voltage adjustment
OUT	6	Output	Output
V+	7	—	Positive supply
V–	4	—	Negative supply

6 Specifications

6.1 Absolute Maximum Ratings

over operating free-air temperature range (unless otherwise noted) (1)

			MIN	MAX	UNIT
V_S	Supply voltage(2)	Single supply		44	V
		Dual supply		±22	
	Input voltage	Differential(3)		±30	V
		Single-ended(4)		±22	
	Output short-circuit(5)		Continous		
T_J	Operating junction temperature		–55	150	°C
T_{stg}	Storage temperature		–65	150	°C

(1) Stresses beyond those listed under *Absolute Maximum Ratings* may cause permanent damage to the device. These are stress ratings only, which do not imply functional operation of the device at these or any other conditions beyond those indicated under *Recommended Operating Conditions*. Exposure to absolute-maximum-rated conditions for extended periods may affect device reliability.
(2) All voltage values, unless otherwise noted, are with respect to the midpoint between V+ and V−.
(3) Differential voltages are at IN+ with respect to IN−.
(4) The magnitude of the input voltage must never exceed the magnitude of the supply voltage or 15 V, whichever is less.
(5) The output can be shorted to ground or to the negative power supply. Fast ramping shorts to the positive supply can cause permanent damage and eventual destruction.

6.2 ESD Ratings

			VALUE	UNIT
$V_{(ESD)}$	Electrostatic discharge	Human-body model (HBM), per ANSI/ESDA/JEDEC JS-001(1)	±1000	V
		Charged-device model (CDM), per JEDEC specification JESD22-C101(2)	±1000	

(1) JEDEC document JEP155 states that 500-V HBM allows safe manufacturing with a standard ESD control process.
(2) JEDEC document JEP157 states that 250-V CDM allows safe manufacturing with a standard ESD control process.

6.3 Recommended Operating Conditions

over operating free-air temperature range (unless otherwise noted)

			MIN	NOM	MAX	UNIT
V_S	Supply voltage	Single supply	6		36	V
		Dual supply	±3		±18	
V_{CM}	Common-mode input voltage	V_S = ±15 V	–13		13	V
T_A	Operating ambient temperature		0		70	°C

6.4 Thermal Information

THERMAL METRIC(1)		OP07x		UNIT
		D (SOIC)	P (PDIP)	
		8 PINS	8 PINS	
$R_{\theta JA}$	Junction-to-ambient thermal resistance	127.6	85	°C/W
$R_{\theta JC(top)}$	Junction-to-case (top) thermal resistance	67.1	68.6	°C/W
$R_{\theta JB}$	Junction-to-board thermal resistance	71.4	55..6	°C/W
Ψ_{JT}	Junction-to-top characterization parameter	18.7	38.3	°C/W
Ψ_{JB}	Junction-to-board characterization parameter	70.6	55.2	°C/W
$R_{\theta JC(bot)}$	Junction-to-case (bottom) thermal resistance	—	—	°C/W

(1) For more information about traditional and new thermal metrics, see the Semiconductor and IC Package Thermal Metrics application report.

6.5 Electrical Characteristics

at T_A = 25°C, V_S = ±15 V, R_L = 2 kΩ connected to mid-supply, and V_{CM} = V_{OUT} = mid-supply (unless otherwise noted)(1).

PARAMETER		TEST CONDITIONS		MIN	TYP	MAX	UNIT
OFFSET VOLTAGE							
V_{OS}	Input offset voltage	OP07C			±60		µV
			T_A = 0°C to 70°C		±85		
		OP07D				±150	
			T_A = 0°C to 70°C			±250	
dV_{OS}/dT	Input offset voltage drift	T_A = 0°C to 70°C	OP07C		±0.5		µV/°C
			OP07D			±2.5	
	Long-term drift of input offset voltage(2)				±0.4		µV/mo
	Offset adjustment range	R_s = 20 kΩ, see Section 8.1			±4		mV
PSRR	Power supply rejection ratio	V_S = ±3 V to ±18 V			7	32	µV/V
			T_A = 0°C to 70°C		10	51	
INPUT BIAS CURRENT							
I_B	Input bias current	OP07C			±1.8		nA
			T_A = 0°C to 70°C		±2.2		
		OP07D				±12	
			T_A = 0°C to 70°C			±14	
	Input bias current drift	OP07C			±18		pA/°C
		OP07D				±50	
I_{OS}	Input offset current	OP07C			±0.8		nA
			T_A = 0°C to 70°C		±1.6		
		OP07D				±6	
			T_A = 0°C to 70°C			±8	
	Input offset current drift	OP07C			12		pA/°C
		OP07D				±50	
NOISE							
	Input voltage noise	f = 0.1 Hz to 10 Hz			0.38		$µV_{PP}$
e_N	Input voltage noise density	f = 10 Hz			10.5		$nV/\sqrt{Hz}$
		f = 100 Hz			10.2		
		f = 1 kHz			9.8		
	Input current noise	f = 0.1 Hz to 10 Hz			15		pA_{pp}
i_N	Input current noise density	f = 10 Hz			0.35		$pA/\sqrt{Hz}$
		f = 100 Hz			0.15		
		f = 1 kHz			0.13		
INPUT VOLTAGE RANGE							
V_{CM}	Common-mode voltage			±13	±14		V
		T_A = 0°C to 70°C		±13	±13.5		
CMRR	Common-mode rejection ratio	OP07C V_{CM} = ±13 V		100	120		dB
			T_A = 0°C to 70°C	97	120		
		OP07D V_{CM} = ±13 V		94	110		
			T_A = 0°C to 70°C	94	106		
INPUT CAPACITANCE							
r_i	Input resistance			7	33		MΩ
OPEN-LOOP GAIN							
A_{OL}	Open-loop voltage gain	1.4 V < V_O < 11.4 V, R_L = 500 kΩ	OP07C	100	400		V/mV
			OP07D		400		
		V_O = ±10 V		120	400		
			T_A = –40°C to +125°C	100	400		

6.5 Electrical Characteristics (continued)

at T_A = 25°C, V_S = ±15 V, R_L = 2 kΩ connected to mid-supply, and V_{CM} = V_{OUT} = mid-supply (unless otherwise noted)(1).

PARAMETER		TEST CONDITIONS	MIN	TYP	MAX	UNIT
FREQUENCY RESPONSE						
	Unity gain bandwidth		0.4	0.6		MHz
SR	Slew rate	V_S = 5 V, R_L = 2 kΩ		0.3		V/µs
OUTPUT						
	Voltage output swing		±11.5	±12.8		V
		T_A = 0°C to 70°C	±11	±12.6		
		R_L = 10 kΩ	±12	±13		
		R_L = 1 kΩ		±12		
POWER SUPPLY						
P_D	Power dissipation	No load		80	150	mW
		V_S = ±3 V, no load		4	8	

(1) The specifications listed in the *Electrical Characteristics* apply to OP07C and OP07D.
(2) Because long-term drift cannot be measured on the individual devices before shipment, this specification is not intended to be a warranty. This specification is an engineering estimate of the averaged trend line of drift versus time over extended periods after the first 30 days of operation.

6.6 Typical Characteristics

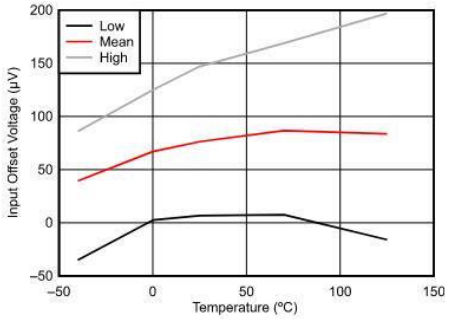

Figure 6-1. Input-Offset Voltage vs Temperature